

©Copyright 2004

Graeme Lufkin

Simulations of Giant Planet Migration in Gaseous
Circumstellar Disks

Graeme Lufkin

A dissertation submitted in partial fulfillment
of the requirements for the degree of

Doctor of Philosophy

University of Washington

2004

Program Authorized to Offer Degree: Department of Physics

UMI Number: 3139505

Copyright 2004 by
Lufkin, Graeme

All rights reserved.

INFORMATION TO USERS

The quality of this reproduction is dependent upon the quality of the copy submitted. Broken or indistinct print, colored or poor quality illustrations and photographs, print bleed-through, substandard margins, and improper alignment can adversely affect reproduction.

In the unlikely event that the author did not send a complete manuscript and there are missing pages, these will be noted. Also, if unauthorized copyright material had to be removed, a note will indicate the deletion.

UMI[®]

UMI Microform 3139505

Copyright 2004 by ProQuest Information and Learning Company.

All rights reserved. This microform edition is protected against
unauthorized copying under Title 17, United States Code.

ProQuest Information and Learning Company
300 North Zeeb Road
P.O. Box 1346
Ann Arbor, MI 48106-1346

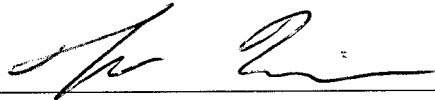
University of Washington
Graduate School

This is to certify that I have examined this copy of a doctoral dissertation by

Graeme Lufkin

and have found that it is complete and satisfactory in all respects,
and that any and all revisions required by the final
examining committee have been made.

Chair of Supervisory Committee:

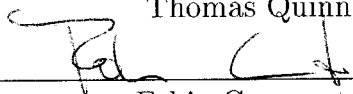


Thomas Quinn

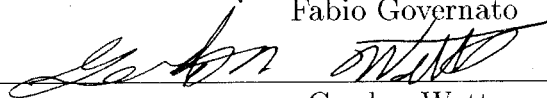
Reading Committee:



Thomas Quinn



Fabio Governato



Gordon Watts

Date:

8/5/2004

In presenting this dissertation in partial fulfillment of the requirements for the Doctoral degree at the University of Washington, I agree that the Library shall make its copies freely available for inspection. I further agree that extensive copying of this dissertation is allowable only for scholarly purposes, consistent with "fair use" as prescribed in the U.S. Copyright Law. Requests for copying or reproduction of this dissertation may be referred to Bell and Howell Information and Learning, 300 North Zeeb Road, Ann Arbor, MI 48106-1346, to whom the author has granted "the right to reproduce and sell (a) copies of the manuscript in microform and/or (b) printed copies of the manuscript made from microform."

Signature

A handwritten signature in black ink, appearing to be "A. H.", written over a horizontal line.

Date

9 August 2004

University of Washington

Abstract

Simulations of Giant Planet Migration in Gaseous Circumstellar Disks

by Graeme Lufkin

Chair of Supervisory Committee:

Professor Thomas Quinn
Department of Astronomy

This work describes the construction, performance, analysis and results of smoothed-particle hydrodynamics simulations of gas disks around Sun-like stars. We provide a history of the Solar System and present the known extrasolar planets data. We simulate planet formation and evolution in a gaseous circumstellar disk using the program *Gasoline*, and describe its implementation of gravity and hydrodynamics. The construction of near-equilibrium gas disks is discussed. We describe the performance and analysis of a large suite of simulations of these disks. These are the first fully three-dimensional, self-gravitating, boundary-free simulations of planet migration. After placing already-formed planets in gas disks, the migration and accretion rates of the planets are measured. We find that planet migration is rapid and scales linearly with the total disk mass. Contrary to the prediction of a linear theory, planet migration is independent of the planet mass. Planets will form gaps in their disks, halting one form of migration, with a timescale that depends most sensitively on the disk mass. In addition, the results of previous simulations of giant planet formation via gravitational instability are confirmed. Additional planet formation triggered by the perturbation of an already-formed planet is found and explored.

TABLE OF CONTENTS

List of Figures	iii
List of Tables	vi
Chapter 1: Introduction	1
1.1 A Brief History of the Solar System	2
1.2 Extrasolar Planets	4
1.3 Giant Planet Formation	6
1.4 Planet Migration	9
1.5 Goals	13
1.6 Organization	14
Chapter 2: Equations of Motion and their Implementation	15
2.1 Brief Discussion of SPH	15
2.2 The Continuity Equation	16
2.3 The Momentum Equation	18
2.4 The Energy Equation and Equations of State	19
Chapter 3: Equilibrium Disk Models: Generating Initial Conditions	22
3.1 Equilibrium Conditions	22
3.2 Manipulating Random Numbers	27
3.3 Distributing Particles Randomly	29
3.4 “SPH-ifying” a Grid Simulation	30

Chapter 4: Migration and Formation Paper	34
4.1 Paper Abstract	34
4.2 Introduction	35
4.3 Initial Conditions	38
4.4 Numerical Realization	41
4.5 Results	43
4.6 Discussion	57
4.7 Conclusion	59
Chapter 5: More Tests of Migration	62
5.1 Performing and Analyzing	62
5.2 Dependence on Planet and Disk Mass	64
5.3 Dependence on Other Parameters	72
5.4 Accretion Onto The Planet	86
5.5 Long Term Behavior	93
5.6 Conclusions	98
Chapter 6: Simulation Visualization Tools	102
6.1 The Need for Parallel Analysis Tools	102
6.2 SALSA's First Task: Simple Visualization	103
6.3 SPH Splatter Visuals	109
6.4 The Future of SALSA	114
Bibliography	124

LIST OF FIGURES

3.1	The density of a circumstellar disk, from a grid model	31
4.1	A parameter space map of disc-planet interactions	44
4.2	Planet mass as a function of time in a $0.1 M_{\odot}$ disc, for different starting masses.	49
4.3	Planet orbital radius as a function of time in a $0.1 M_{\odot}$ disc, for different starting masses	50
4.4	A sequence of snapshots showing the gas density in a protoplanetary disc. The presence of a planet triggers the formation of additional planets.	52
4.5	A sequence of snapshots showing the gas density in an unstable protoplanetary disc. Planets form via gravitational instability.	53
4.6	Formation in an unstable disc: The orbital radius of several clumps as a function of time	55
4.7	Formation in an unstable disc: The mass of several clumps as a function of time	56
4.8	Azimuthally and vertically averaged surface density of two discs with embedded Jupiter-mass planets	60
5.1	The migration rate as a function of the planet mass in a $0.01 M_{\odot}$ disk	66
5.2	The migration rate as a function of the planet mass in a $0.05 M_{\odot}$ disk	67
5.3	The accretion rate as a function of the planet mass in a $0.01 M_{\odot}$ disk	69
5.4	The accretion rate as a function of the planet mass in a $0.05 M_{\odot}$ disk	70

5.5	The migration rate of a $1 M_{\text{Jup}}$ planet as a function of the disk mass .	71
5.6	The migration rate of a $0.3 M_{\text{Jup}}$ planet as a function of the disk mass	72
5.7	Accretion shuts off when Hill radius shrinks	73
5.8	The accretion rate of a $1 M_{\text{Jup}}$ planet as a function of the disk mass .	74
5.9	The accretion rate of a $0.3 M_{\text{Jup}}$ planet as a function of the disk mass	74
5.10	Migration rate of a $1 M_{\text{Jup}}$ planet in a $0.01 M_{\odot}$ disk as a function of the simulation resolution	76
5.11	Accretion rate of a $1 M_{\text{Jup}}$ planet in a $0.01 M_{\odot}$ disk as a function of the simulation resolution	77
5.12	Accretion rate onto the planet as a function of the gravitational soft- ening length of the gas particles	81
5.13	Accretion rate onto the planet as a function of the gravitational soft- ening length of the planet	82
5.14	Semi-major axis of planets in disks with different equations of state .	85
5.15	Gas particles making up the envelope of a planet in a $0.01 M_{\odot}$ disk .	87
5.16	Zero-velocity curves in the restricted three-body problem with mass ratio appropriate for the Sun–Jupiter system	88
5.17	Gas particles that will soon be part of a planet in a $0.01 M_{\odot}$ disk . .	90
5.18	Projected density of particles making up a planet	92
5.19	Semi-major axis and mass of a planet forming a gap in a $0.05 M_{\odot}$ disk	95
5.20	Surface density profiles of a planet forming a gap in a $0.05 M_{\odot}$ disk .	96
5.21	A snapshot of a simulation where the planet has formed a gap in the disk	97
5.22	The semi-major axis of a $1 M_{\text{Jup}}$ planet in a $0.01 M_{\odot}$ disk, taking a long time to fully form a gap	98

6.1	A view of a three-dimensional simulation is defined by an infinite parallelepiped through the simulation volume	106
6.2	The axes of a view through a simulation	107
6.3	A planet formation simulation rendered pointlike by SALSA	108
6.4	In a splatter visual, a single SPH particle can contribute to several pixels	110
6.5	A planet formation simulation rendered splatter by SALSA	112

LIST OF TABLES

4.1	Migration time-scales and accretion rates for Type I systems	47
-----	--	----

ACKNOWLEDGMENTS

As the acknowledgments of this thesis, I'd like to thank you for reading me. In so doing, you have brought the words on this page to life, if only briefly. Although, since this text will be preserved for some time, perhaps it's not words on a page that you're reading. Maybe words on a computer display, a spoken version, or some means of display not yet conceived. If you'll tolerate a brief interruption, the body of the thesis has some thoughts to convey to you.

Hello, this is the thesis itself speaking. First of all, why are you reading me? Don't you know that nobody is supposed to read theses? Seriously, what reason could you possibly have to waste your time reading me? Really, if you've got this much free time, you should go outside and run around. Climb a mountain, go surfing, fly a kite, anything! Well, I suppose I can't stop you. After all, I'm nothing but words on a page.

That's why we don't let the thesis talk too often. To live up to my name, I suppose I'd better acknowledge someone. I'd like to thank Graeme himself for putting in the long hours and struggling through the tricky bits just so I could be here. Way to go, pal. Without you, I wouldn't exist.

Chapter 1

INTRODUCTION

The motion of the Sun, Moon, planets and stars across the sky invariably leads the curious observer to ask why, and where, they came from. Cosmogony, the study of the formation of the Solar System, is one of the oldest scientific endeavors. Ancient Greeks gave the name *planet* to the wandering stars, distinguishing them from the myriad other fixed stars, but it was not until the Copernican revolution that cosmogony and cosmology were revealed as separate fields of study. Observational cosmogony reigned as Galileo's pioneering use of the telescope revealed a system of moons orbiting Jupiter, exactly as the planets orbit the Sun. Newton's theory of universal gravitation established a set of rules and a rudimentary scale for the Solar System. Theoretical cosmogony was born when Kant and Laplace combined gravity and angular momentum to suggest the nebular theory of formation. The 20th century saw the onset of experimental cosmogony as meteorites revealed clues to the composition of the early Solar System and spacecraft visited the outer planets. Finally, in just the last few decades, observations of protoplanetary disks and Doppler-signatures of extrasolar planets have promoted cosmogony to the study of the formation of *all* planetary systems, not just our own.

In this introduction we discuss the scientific theory of planet formation and evolution to motivate the study of a particular aspect: the formation and orbital migration of giant planets in gaseous disks around Sun-like stars. The results presented in later chapters contribute to the large body of knowledge that forms the basis of modern

cosmogony.

1.1 A Brief History of the Solar System

The current scientific understanding of how the Solar System formed is best told as a short bedtime story.

More than four and a half billion years ago, a cloud of interstellar gas and dust collapsed to form what became our Sun. The cloud material that did not collapse onto the protosun was flattened into a protoplanetary disk through the conservation of angular momentum. Viscous forces in the disk lead to accretion onto the star until the present mass was reached. Some 1–10 million years after forming, the gas disk dispersed, perhaps due to strong stellar winds. In the disk, planets, moons, asteroids and comets formed and began to interact. Over the next few hundred-million years, collisions between large gravitating bodies became less frequent, as most of the mass became part of a small number of large bodies. For the next four billion years, the Sun made its way along the main sequence, its steady shine slowly increasing on its way to a red giant. The Earth, with its oceans of water, possibly delivered by comets, and its evolving atmosphere of light gases, followed its orbit around the Sun, along with eight other major planets, hundreds of moons, thousands of asteroids, and millions of comets. Then, just yesterday, astronomically and geologically speaking, we sprang up from bacteria in the primordial oceans and started asking how the Solar System formed.

The previous story has been worked out over the past 250 years by astronomers both theoretical and observational. Although a few details are known with great certainty, the next 250 years will see revisions, great and small, made to the explanation for almost all phases. Here we briefly describe how the above description came about.

The age of the Solar System is known by radioactive dating of meteorites and models of the evolution of the Sun. The nebular hypothesis, first presented by Kant and Laplace in the 18th century, states that the Solar System was formed by the collapse of a cloud of gas, a star forming at the center and the remains flattening into a circumstellar disk. Observations reveal that molecular clouds are ripe with star formation (Hester et al., 1996; Thompson et al., 2002; Muzerolle et al., 2004), and simulations confirm that clouds can collapse into stars with surrounding disks (Bate et al., 2003a). Circumstellar disks were first observed in the 1960s as an excess emission of infrared radiation from young stellar objects (Mendoza V., 1966, 1968). We now know the emission is due to dust mixed through the gas disk, making up just a small fraction of the total mass (Rucinski, 1985).

The total mass of the protoplanetary disk remains a subject of debate. A lower bound of $0.01 M_{\odot}$ can be derived by extrapolating the masses of the existing planets (Hayashi et al., 1985). This is called the *minimum mass solar nebula*. The mechanism for dispersing the gas is also unknown. Possible solutions include accretion onto the protosun, strong stellar winds and photo-evaporation by nearby sources of ultraviolet radiation (Hollenbach et al., 2000).

Both during and after the lifetime of the gas disk, solid bodies played an important role. Interstellar dust grains, condensates from the gas and, beyond the snow line, ices are a source of micron-size solid bodies. The growth from dust to meter and kilometer-size bodies, a range of nine orders of magnitude, is the least-well-understood phase of planet formation. Two possible mechanisms are gravitational instability of a thin disk of solid bodies and coagulation via an unknown sticking mechanism. Collisions between small solid bodies could be enhanced by turbulent viscosity in the disk. A review of this period of planet formation is Weidenschilling and Cuzzi (1993). Gas pressure forces cause the orbital velocity of the gas to be sub-Keplerian. Solid bodies larger than a kilometer will decouple from the gas and move on Keplerian orbits.

Once the gas disk dispersed, the evolution of the debris of the Solar System proceeded as the interaction of point masses (Duncan and Quinn, 1993; Richardson et al., 2000). A period of oligarchical growth led to a handful of bodies on roughly circular orbits. During this “clean up” phase of formation, impacts between large bodies were common, one forming the Earth’s Moon. The role of Jupiter and comets in forming the Earth’s environment is actively being pursued (Raymond et al., 2004).

Here on Earth, fossilized bacteria show that life arose as early as a billion years after formation. Whether life in the Solar System is unique to Earth is unknown, to be tested soon by probes to Mars, Saturn’s moon Titan and Jupiter’s moon Europa. The process of evolution presented by Darwin (1859) enabled us to understand how complex structures arise and replicate so profusely (Dawkins, 1989). We are finally able to ask meaningful questions about the origin of the Solar System and raise the possibility of planet formation elsewhere.

1.2 *Extrasolar Planets*

The Solar System is no longer the only known example of planets orbiting a star. Since 1995, Doppler-shift measurements of nearby Sun-like stars have revealed hundreds of new planets (Mayor and Queloz, 1995; Marcy and Butler, 2000), see exoplanets.org for a current list. To date, the newly discovered planetary systems are all starkly different from the Solar System. This is partially due to an observational bias, but nonetheless reveals a previously unpredicted class of planetary systems whose origins are not well understood.

The known extrasolar planets can be grouped into three rough categories: Hot Jupiters, eccentric giants and multiple-planet systems. Hot Jupiters are planets on almost perfectly circular orbits just a few tenths of an AU from their parent star, ranging from one quarter to a few Jupiter masses. These planets are the most easily detected, as they produce large oscillations in the Doppler shift of a star and require

only a few days to observe an entire period of the orbit of the planet. Their near-circular orbits are understood to be due to eccentricity damping via tidal interaction with the nearby star. Eccentric giants are on orbits larger than 0.15 AU and have eccentricities more than six times larger than the planets in our Solar System, on average. The maximum observable orbital period is limited by the length of time data has been collected. Finally, about ten percent of the stars with planets possess more than one observed planet. Recent simulations reveal regions of orbital stability in these systems where additional, lower mass planets could reside (Barnes and Raymond, 2004).

The Hot Jupiters were a source of much debate in the years following their discovery. Their existence contradicted the conventional wisdom about planetary systems gained from exploring our own Solar System. It was believed that giant planets formed with little eccentricity in the cool outer reaches of the disk, and remained on those orbits for their entire lifetime. When there were only a few known extrasolar planets, all Hot Jupiters, it was suggested that perhaps they were merely planetary outliers, brought to misleading prominence by the selection bias inherent in the Doppler shift technique. As more planets on larger orbits were detected, it became clear that this was not the case. While eccentric giants now outnumber them, Hot Jupiters remain a sizable percentage of the extrasolar planet population. A theory of giant planet formation will be incomplete if it cannot explain how these planets formed and evolved.

The eccentric giants surprised astronomers in a different direction. Excepting Mercury, all the major planets in our Solar System have eccentricities below 0.1. It was widely believed that large eccentricity in forming planets would be damped via interaction with the protoplanetary disks.

In the mid-20th century, the discovery of the muon prompted physicist I.I. Rabi to ask “Who ordered this?” Similarly, planetary astronomers never believed Jupiter-mass planets with several-day orbits could exist, until they were detected. Nature has once again revealed the limitations of our imagination, providing us with a host

of planetary systems strikingly different from our own. We are now faced with the challenge of explaining these unmasked-for planets. Two possibilities arise: the planets formed at their present location or formed elsewhere and underwent some form of orbital evolution. By examining our current understanding of giant planet formation, we conclude that the second possibility is more likely. This is the motivation for the work described in this thesis.

1.3 Giant Planet Formation

There are currently two popular theories of giant planet formation. Most likely, future work will reveal that each possibility plays a role, depending on the initial conditions. For a more detailed discussion of giant planet formation, see Wuchterl et al. (2000).

The first theory, the *core accretion* model, suggests that giant planets form by growing a rocky core, then accreting a large gas envelope (Hayashi et al., 1985; Lissauer and Stewart, 1993; Pollack et al., 1996). This scenario is also known as the core instability, or nucleated instability model. A rocky core is built from the agglomeration of small solid bodies in the protoplanetary nebula. Above a critical mass, determined by the density of planetesimals in the disk, gravitational focusing allows a core to undergo runaway accretion until it depletes its feeding zone (Podolak et al., 1993). Up to this point, this scenario is identical to the accepted theory of terrestrial planet formation. If the core grows in the outer, cooler part of the disk, gas accretion can occur, building a gas giant. To form a Jupiter-mass planet, it is believed that a core of roughly ten Earth-masses is necessary. Gas accretion is also a runaway process, and is limited by the opacity of the gas, as the envelope must radiate its thermal energy to contract. The gas envelope becomes the great majority of the mass of the planet. The timescale for core growth is determined by the density of rocky material. The timescale for gas envelope growth is determined by the temperature and density of the gas. Using this scenario, Pollack et al. (1996) estimated a formation time of

1–10 million years for Jupiter, assuming a disk density three times greater than the minimum mass solar nebula model. This is currently the accepted formation scenario for the giant planets in our Solar System.

The core accretion model of giant planet formation has several advantages. It builds upon an already-accepted framework, terrestrial planet formation. It allows the formation of multiple planets. It explains the observed non-Solar abundances of heavy elements in the atmosphere and the solid cores of the giant planets in our Solar System. Finally, it also incorporates the formation of smaller Solar System denizens, the asteroids and comets. The most significant difficulty of the core accretion model is the timescale it requires. Although a large percentage of young stars have detectable circumstellar disks (Beckwith and Sargent, 1993), the disks vanish by the time the star is about ten million years old (Strom et al., 1993). To form giant planets via the core accretion mechanism, the planet must form its gas envelope during the lifetime of the gas disk. In the race to form gas giant planets before the disk dissipates, core accretion is the tortoise, taking of order a million years to form Jupiter-mass planets. In addition, the core accretion model cannot currently be directly simulated from the beginning. The number of kilometer-sized planetesimals in a protoplanetary disk is on the order of 10^{12} , well beyond today’s computational reach. All simulations thus rely on the “particle-in-a-box” approximation or start with planetary embryos already as large as an Earth-mass.

The second theory, the *disk instability* model, suggests that giant planets form directly out of the gas disk, via gravitational collapse. The physical process is identical to the theory of spiral structure in galaxies, scaled down to solar system size. In a circumstellar gas disk, a density perturbation will be sheared by the differential rotation, forming a spiral pattern. The normal modes of oscillation are thus spiral density waves. If the density in one of these waves becomes high enough, the enhanced local self-gravity will overcome the repulsive gas pressure, and the region will collapse. This process is known as the Toomre disk instability, and is quantified by

the dimensionless Toomre Q criterion (Binney and Tremaine, 1987).

$$Q = \frac{c_s \kappa}{\pi G \Sigma} \quad (1.1)$$

where c_s is the sound speed, κ is the epicyclic frequency, G is the gravitational constant and Σ is the surface density of the gas. For a two-dimensional disk, linear analysis reveals that, for $Q < 1$, the disk is unstable to an axisymmetric perturbation. This is a global instability. Nonetheless, simulations indicate that Q is a good indicator of a local instability, where the disk fragments into bound objects. In a circumstellar disk, these clumps of collapsed gas are identified as gas giant planets. Simulations suggest that three-dimensional, isothermal gas disks with Q as high as 1.4 may be susceptible to fragmentation (Mayer et al., 2002; Lufkin et al., 2004).

The disk instability model of giant planet formation also has several advantages. The formation timescale is very short, only several hundred years (making disk instability the hare). It naturally, possibly even preferentially, allows the formation of multiple planets. The most persistent criticism of the disk instability model has been that it requires a disk that is inordinately cooler and more massive than the minimum mass solar nebula model. Repeatedly, simulations have pushed down the disk mass required for instability (Boss, 2000, 2002; Mayer et al., 2002, 2003). We now have unstable disk models with disk masses only a few times greater than the minimum mass solar nebula. The disk instability model also does not naturally explain the presence of solid cores in giant planets, as are observed in our Solar System.

One element that both theories have in common is the location of the giant planets they form: far out (several AU) in the disk. Both theories prohibit the formation of giant planets at less than an AU from the central star, due to the larger Keplerian shear and high temperature of the disk gas. How do we reconcile this with the observed distribution of planets? Of the known extrasolar planets, fully 16% orbit less than a tenth of an AU from their parent stars. As more planets are detected, it becomes clear that close-in planets are not a statistical anomaly. We must therefore

explain how a giant planet moves from the cool outer regions to the hot inner core of a circumstellar disk.

1.4 Planet Migration

Planet migration is the secular change of the semi-major axis of the orbit of a planet. The most extensively studied theory of planet formation involves interaction between a planet and the gas disk it is embedded in. Depending on the particular interaction, this is known as Type I or Type II migration.

First, we briefly discuss some alternate scenarios for planet migration, ultimately dismissing them. Planet migration via repeated scattering of small planetesimals has been suggested (Murray et al., 1998; Hahn and Malhotra, 1999; Del Popolo et al., 2001; Cionco and Brunini, 2002). There is evidence that, in our own Solar System, Jupiter has migrated inward by repeatedly scattering comets. By looking at the orbits of Kuiper Belt objects, however, we see that Uranus and Neptune have migrated outward (Malhotra, 1999). In addition, to move a giant planet in to a few-day orbit would require an inordinate amount of planetesimals. Dynamical interaction between multiple giant planets can induce large changes in semi-major axis and eccentricity. The gravitational instability mode of planet formation is capable of producing several planets with non-negligible eccentricity, which would definitely experience significant orbital changes due to dynamical interaction. While this method of migration could place giant planets on very small orbits, it would not do this preferentially. Also, only about ten percent of the known extrasolar planets are in multiple-planet systems. While these mechanisms for planet migration are physically realistic and likely do occur, in their current form they are not by themselves sufficient to explain the observed distribution of extrasolar planets. See Lin et al. (2000) for a discussion of other migration scenarios. We now turn to the theory of migration via interaction with a gas disk.

The mathematics of gravitational interaction between a disk and embedded object was first developed by Goldreich and Tremaine (1978b) to explain features in the rings of Saturn. It was immediately extended to the orbital migration of a planet in a circumstellar disk (Goldreich and Tremaine, 1980). It is based on two principles. First, that density fluctuations in a differentially rotating disk are wound into a spiral shape. Second, that a tightly wound spiral pattern can be treated via a Fourier decomposition. Here we briefly explain the physical processes behind Types I and II migration, then discuss previous theoretical and simulation-based results. Note that although the application of spiral density waves to planet migration shares some terminology and mathematical structure with the Lin–Shu spiral density wave theory of galactic structure, it is not exactly the same theory.

A planet gravitationally affects the gas disk it is embedded in. These perturbations take the form of *spiral density waves* excited at Lindblad resonances of the planet (Goldreich and Tremaine, 1979; Ward, 1986). Because a spiral is non-axisymmetric, the perturbed disk acts back on the planet, exerting a net torque. The inner waves carry negative angular momentum, moving the planet outward and disk material in. Similarly, the outer waves carry positive angular momentum, sending disk material outward and the planet in. In a wide range of models for the radial density distribution of the disk, the outer torque is larger than the inner, leading to an overall change in the orbit of the planet (Ward, 1986).

1.4.1 Theory

By making several approximations, the torque due to spiral density waves can be calculated, yielding a migration timescale as a function of the parameters of the disk and planet. Here we discuss the steps, without presenting the mathematics, and quote a final result. For a detailed presentation of the mathematics, see Goldreich and Tremaine (1978a, 1979, 1980); Artymowicz (1993); Ward (1986, 1997); Tanaka et al. (2002).

First, the potential of the planet is expanded in a Fourier series. This expansion identifies the Lindblad resonances of the planet: locations in the disk that feel the periodic forcing of the potential of the planet. By linearizing the equations of motion, it can be shown that density builds in these regions and is propagated away from the planet as a wave due to the differential rotation. The waves dissipate in the disk via turbulent viscosity and nonlinear shocking. This process serves to move energy and angular momentum from the excitation site, the Lindblad resonances, to the dissipation site, farther in or out in the disk. The exchange of angular momentum is a torque on the planet and disk material, causing a change in their orbits. To first order, this change affects only the semi-major axis, not the eccentricity. By assuming a form and location for the dissipation, the total amount of torque can be calculated.

Historically, the above process was carried out and the migration timescale for proto-Jupiter in a minimum mass solar nebula was estimated at a few times 10^4 years. Refinements were made, including recognizing the effects of gap formation, corotation resonances and a three dimensional disk. A recent estimate by Tanaka et al. (2002) gives a migration timescale of 8×10^5 years for an Earth-mass planet at 5.2 AU. They also provide an expression for the inward migration rate, in which we have substituted the parameters for our simulations to obtain

$$\dot{a}_p = -217.5 \left(\frac{M_D}{M_\odot} \right) \left(\frac{M_p}{M_\odot} \right) \text{ AU/yr} \quad (1.2)$$

where M_D is the total mass of the disk and M_p is the mass of the planet.

The mathematical treatment of the physical process described in the preceding paragraphs is known as Type I migration. If a planet opens a gap in the disk, there will be no disk material at the Lindblad resonances to excite, and therefore no Type I migration. A planet forms a gap if its tidal torque exceeds the viscous force for material on nearby orbits (Lin and Papaloizou, 1993; Takeuchi et al., 1996; Rafikov, 2002). There are several criteria for gap formation, boiling down to a critical planet mass. Even after forming a gap, the planet can still migrate if there is an overall

source of viscosity in the disk. This is known as Type II migration. In this case, the planet and the inner and outer portions of the disk will move inward together with the viscous timescale. In general, this is much longer than the Type I migration timescale. To quantify the viscous timescale, most researchers assume a parametrized form for the effect of viscosity in the disk, known as an α prescription (Shakura and Sunyaev, 1973).

The discussion above has not considered changes in the eccentricity of planets in gas disks. Although there is a body of work addressing this, we have omitted its discussion based on its added difficulty and because we did not observe large changes in eccentricity in our simulations of this phenomena. See Lin et al. (2000) for a discussion of eccentricity evolution.

1.4.2 Simulation

Many simulations have been performed to test the assumptions and predictions of the theory of Type I and II migration. The most important approximations made in the theory of Type I migration are the linear response of the disk to the planet, ignoring the self-gravity of the disk, and approximating the disk as two-dimensional. All simulations capture the possibly non-linear response of the disk to the planet, but only recently have simulations been performed where the self-gravity and three-dimensional nature of the disk are embraced.

The majority of simulations of disk-planet interaction have been performed with two-dimensional Eulerian grid codes. This technique limits the spatial resolution to the grid size and requires a prescription for boundary conditions. Using such grids, gap formation has been investigated by Kley (1999); Bryden et al. (1999); Lubow et al. (1999). Nelson et al. (2000b) compared three different grid codes, finding rapid Type II migration.

Recently, D'Angelo et al. (2002, 2003) have used a system of nested grids to achieve excellent spatial resolution close to the planet. Their findings indicate that

the circumplanetary material can have an important effect on the orbit of the planet. Their gap formation simulations confirm that accretion slows but does not stop after a planet has formed a gap.

Three-dimensional grids have been used by Bate et al. (2003b), ignoring the self-gravity of the disk. They found the migration rate to vary with the planet mass as predicted by Tanaka et al. (2002).

Smoothed particle hydrodynamics (SPH) is a Lagrangian simulation technique that has seen great success in other areas of computational astrophysics. Only recently has it been applied to solar-system scale problems. Nelson et al. (1998, 2000a) compared a grid code with SPH while studying the formation of spiral waves in unstable gas disks. Also, Schäfer et al. (2004) has used SPH to simulate the migration of one and two planets in a gas disk, in the two-dimensional approximation and ignoring the self-gravity of the disk.

The effect of magnetic fields in the disk has been studied by Papaloizou and Nelson (2003); Papaloizou et al. (2004); Nelson and Papaloizou (2003, 2004) using a two-dimensional grid. Contrary to many other simulations, they found migration of several-Earth-mass planets to be non-secular, with disk torques fluctuating rapidly over the orbital period of the planet.

Self-gravity of the disk has finally been included by Nelson and Benz (2003a,b). Their results are similar to ours, and are specifically discussed in Chapter 5.

1.5 Goals

The challenge is to understand the nature of disk–planet interaction, specifically to explain the presence of giant planets on small orbits about their parent stars. To meet this goal, we performed simulations of disk–planet systems using the smoothed particle hydrodynamics technique. In massive disks, we looked for planet formation via the disk instability alone and with the trigger of an already–formed planet. In

lighter disks, we examined migration of the planet through the disk. In this thesis, we assume that planets form farther out in the disk, around the present orbit of Jupiter in our Solar System. We also limit ourselves to Sun-like parent stars. By measuring the migration rate of a planet, we tested the predictions of migration theory. By using a new computational technique, we increase the robustness of the pool of simulation results. This tool incorporates many physical aspects that have hitherto been ignored in simulations. Namely, we include the self-gravity of the disk, are fully three-dimensional and have free boundary conditions.

1.6 Organization

The rest of the text is organized as follows. In Chapter 2 we discuss the equations of motion for the disk–planet system and their computational implementation. The subject of Chapter 3 is the process of constructing the initial conditions to use in the simulations. Chapter 4 contains the body of a paper published as Lufkin et al. (2004), giving an overview of the relationship between Types I and II migration, and results regarding planet formation due to gravitational collapse. More migration simulations and results are presented in detail in Chapter 5. Finally, Chapter 6 discusses tools used to visualize and analyze these and other simulations.

Chapter 2

EQUATIONS OF MOTION AND THEIR IMPLEMENTATION

In the most fundamental sense, a gas dynamical simulation is a way of solving the Boltzmann equation for some fluid. Of course we don't solve the complete six-dimensional Boltzmann equation, but rather integrate the Boltzmann equation over velocity using the applicable collisional invariants. We then solve discrete versions of those integrals, known as the equations of motion, given some initial conditions. Details of performing the integrations to obtain the equations discussed below can be found in, e.g., Battaner (1996); Shu (1991); Binney and Tremaine (1987).

The equations of motion relevant to a gaseous disk are the continuity equation, the momentum equation, and the energy equation. Here we discuss each equation in turn, detailing how the equation is used in the SPH simulations.

2.1 *Brief Discussion of SPH*

Smoothed Particle Hydrodynamics (SPH) is a way to model the physics of a continuous fluid via a collection of particles. Each particle has an extended size and mass distribution. This technique can be thought of as Monte Carlo sampling the fluid. Each particle has various fundamental and composite attributes. The fundamental attributes are usually mass, position, velocity and gravitational softening length. Composite attributes are determined by the state and configuration of other particles or external factors, and may include smoothing length, density and diffusive energy flux. Depending on the equation of state used, energy can be either a fundamental

or composite attribute.

SPH is a Lagrangian method, preserving a fixed mass resolution. By using a spatially varying smoothing length, it becomes spatially adaptive. By using a hierarchical multi-stepping scheme for integrating the motion of the particles, it becomes temporally adaptive. It is particularly well-suited for problems with free boundary conditions and large density contrasts. See Monaghan (1992) for a detailed review of SPH.

The work described in this thesis uses *Gasoline*, a portable, parallel tree-based gravity solver that includes an implementation of SPH (Wadsley et al., 2004). In *Gasoline*, the integration of the momentum equation is second-order accurate, while the energy equation is first-order accurate.

2.2 The Continuity Equation

Using the principle of conservation of mass leads to the first equation of motion, the continuity equation. It is expressed by the equation:

$$\frac{\partial \rho}{\partial t} + \nabla \cdot (\rho \mathbf{v}) = 0 \quad (2.1)$$

where ρ is the mass density and \mathbf{v} the velocity. In the SPH formalism, mass is carried by the particles and does not change as a function of time. Therefore, if no particles exit or enter the system, mass is exactly conserved. This equation does not actually appear in our implementation of SPH. Instead, the density at any point in space is defined by the masses of nearby particles, weighted by the smoothing kernel:

$$\rho(\mathbf{r}) = \sum_b m_b W(\mathbf{r} - \mathbf{r}_b, h) \quad (2.2)$$

where the sum is over all the particles in the simulation, m_b is the mass of the b th particle, \mathbf{r} is the position, W is known as the smoothing function or kernel and h as the smoothing length. The smoothing function represents the extended distribution of mass given to each particle.

2.2.1 The Cubic-Spline Smoothing Kernel

The smoothing kernel determines how nearby particles contribute to composite quantities. The most commonly used smoothing kernel is the cubic-spline kernel. It is spherically symmetric and has compact support. In three dimensions it has the form:

$$W(r, h) = \begin{cases} \frac{1}{\pi h^3} \left(1 - \frac{3}{2} \left(\frac{r}{h} \right)^2 + \frac{3}{4} \left(\frac{r}{h} \right)^3 \right) & \text{for } r < h \\ \frac{1}{\pi h^3} \frac{1}{4} \left(2 - \frac{r}{h} \right)^3 & \text{for } h \leq r < 2h \\ 0 & \text{for } r \geq 2h \end{cases} \quad (2.3)$$

This is the kernel used in all the simulations described in this thesis.

If the smoothing length is not the same for each particle, there are multiple ways to interpret SPH equations. For each occurrence of the smoothing kernel, which smoothing length h do we supply? To calculate a smoothed quantity of particle a , the *gather* interpretation uses h_a , the smoothing length of the target particle. Alternatively, the *scatter* interpretation uses h_b , the smoothing length of the contributing particle. We use a symmetric combination, known as *gather/scatter*, where each occurrence of the smoothing kernel is replaced by its average:

$$W(r, h) \Rightarrow \frac{1}{2} (W(r, h_a) + W(r, h_b)) \quad (2.4)$$

The gradient of the kernel is also replaced by its average.

In our simulations, each particle has its own smoothing length. This distance is calculated dynamically as half the distance to the n th-nearest neighbor of the particle. This prescription ensures that smoothing lengths will be small in regions of high particle density. Choosing the particular number of nearest neighbors is a trade-off between noisy estimates (small n) and smoothing out real small-scale features (large n). The combined experience of the SPH community suggests that $24 < n < 50$ yields an effective trade-off for a wide variety of simulations. We use $n = 32$ for all the simulations discussed here. Note that, using the *gather/scatter* interpretation,

exactly n particles will contribute to the gather part of the sum. The number of scatter contributors will depend on the spatial configuration of the neighboring particles.

2.3 The Momentum Equation

The zeroth-order solution to the momentum integral of the Boltzmann equation is known as Euler's equation:

$$\frac{D\mathbf{v}}{Dt} = -\frac{\nabla P}{\rho} - \nabla\Phi \quad (2.5)$$

where $\frac{D}{Dt} = \left(\frac{\partial}{\partial t} + \mathbf{v} \cdot \nabla\right)$ is the convective derivative operator, P is the pressure and Φ is the gravitational potential. The acceleration due to gravity ($-\nabla\Phi$) is calculated using a tree (Stadel, 2001). The pressure gradient is calculated with SPH, using the tree to find nearest-neighbors, yielding the acceleration on particle a due to pressure gradients:

$$\frac{D\mathbf{v}_a}{Dt} = -\sum_b m_b \left(\frac{P_b}{\rho_b^2} + \frac{P_a}{\rho_a^2} + \Pi_{ab} \right) \nabla_a W(\mathbf{r}_a - \mathbf{r}_b, h) \quad (2.6)$$

where Π_{ab} is the artificial viscosity term discussed below. See Hernquist and Katz (1989) and Monaghan (1992) for a discussion of the choice of the form of the momentum equation.

2.3.1 Artificial Viscosity

Euler's equation is exact for a dissipationless fluid. The next-higher order approximation, the Navier–Stokes equations, include terms that account for dissipation due to viscosity in the fluid. In the astrophysical systems we are interested in, we cannot resolve the molecular-level forces that give rise to viscosity. However, we can parametrize certain known effects that take the same form as true molecular viscosity. We then add this artificial viscosity to the momentum and energy equations (equations 2.6 and 2.9). The artificial viscosity is designed to handle shocking in the gas. In addition, it serves to stabilize the numerical integration of the momentum

and energy equations. The most commonly used form for artificial viscosity in SPH is:

$$\Pi_{ab} = \begin{cases} \frac{1}{\bar{\rho}_{ab}} (-\alpha \bar{c}_{ab} \mu_{ab} + \beta \mu_{ab}^2) & \text{for } (\mathbf{v}_a - \mathbf{v}_b) \cdot (\mathbf{r}_a - \mathbf{r}_b) < 0 \\ 0 & \text{for } (\mathbf{v}_a - \mathbf{v}_b) \cdot (\mathbf{r}_a - \mathbf{r}_b) \geq 0 \end{cases} \quad (2.7)$$

$$\mu_{ab} = \frac{\bar{h}_{ab} (\mathbf{v}_a - \mathbf{v}_b) \cdot (\mathbf{r}_a - \mathbf{r}_b)}{|\mathbf{r}_a - \mathbf{r}_b|^2 + \eta^2 \bar{h}_{ab}^2} \quad (2.7a)$$

where barred values indicate averages over the two interacting particles, $c = \sqrt{\gamma P / \rho}$ is the sound speed, $\eta = 0.1$ prevents singularities, and α and β parametrize the linear and quadratic terms. See Monaghan (1992) and Nelson et al. (2000a) for discussions of this form of artificial viscosity. In addition, we use a Balsara switch to reduce spurious viscosity in regions of strong shear (Balsara, 1995). In Section 5.3.3 we examine the effects of varying the parameters α and β .

2.4 The Energy Equation and Equations of State

The third collisional invariant is the energy, yielding the energy equation:

$$\frac{Du}{Dt} = -\frac{P}{\rho} \nabla \cdot \mathbf{v} + \frac{1}{\rho} (\Gamma - \Lambda) \quad (2.8)$$

where u is the internal energy per unit mass, and Γ and Λ are external heating and cooling sources, respectively.

Without the heating and cooling terms and including the effect of artificial viscosity, the SPH form of the energy equation we use is:

$$\frac{Du_a}{Dt} = \sum_b m_b \left(\frac{P_a}{\rho_a^2} + \frac{1}{2} \Pi_{ab} \right) (\mathbf{v}_a - \mathbf{v}_b) \cdot \nabla_a W(\mathbf{r}_a - \mathbf{r}_b, h) \quad (2.9)$$

The continuity, momentum and energy equations provide five equations for the six quantities ρ , \mathbf{v} , u and P . To solve the system we use a closure relation, known as the equation of state, which expresses the pressure as a function of the density and energy: $P = P(\rho, u)$. The choice for the equation of state determines what kind of

a gaseous system we are modeling. Here we describe three common choices for the equation of state.

2.4.1 *Isothermal*

In an isothermal gas, the temperature remains constant through changes in density. Such a process does not conserve energy, so we cannot use the energy equation. The physical picture for such a process is of non-equilibrium energy due to expansion, contraction and shock heating being immediately radiated away to infinity. For many astrophysical simulations, the radiative cooling time is sufficiently smaller than the dynamical time to justify this approach.

To simulate an isothermal system, we need the pressure of each particle to integrate the momentum equation. Via the ideal gas law, the pressure of a particle is a product of the local density and the local temperature.

For a circumstellar disk, the dominant source of energy will be the radiation from the central star. As such, the equilibrium temperature should be dependent solely on the distance to the star. Because we are interested in a thin disk, we ignore vertical variations in the temperature.

To simulate this situation, the temperature of each particle is determined by the cylindrical radial distance to the star. This temperature and the calculated density (Equation 2.2) yield the pressure for each particle. This treatment is different from *Gasoline*'s standard isothermal equation of state, where the temperature of each particle is fixed for the duration of the simulation by the initial conditions. The alternate implementation was added to the code by the author. The code reads a set of pairs of radial distance and temperature, composing the temperature profile table. Individual temperatures are interpolated from this table using the radial position of each particle.

Except where otherwise noted (see Section 5.3.4) we use an isothermal equation of state where the temperature is a function solely of the radial distance in a cylindrical

coordinate system.

2.4.2 Adiabatic

In an adiabatic gas, no heat is lost during changes in density. Following the First Law of Thermodynamics, contraction and expansion of the gas can change the energy. To simulate an adiabatic gas, we keep track of the PdV work done by each particle during a timestep by using Equation 2.9. Note that work is also done by shock heating, accounted for by the artificial viscosity term. The pressure of each particle depends on the adiabatic index, density and internal energy: $P = (\gamma - 1)\rho u$.

2.4.3 Cooling Time

In addition to the work done by adiabatic expansion and contraction and shock heating, external sources of heating and cooling can be included. Such terms can handle physics that is not explicitly handled elsewhere in the simulation, for example radiative cooling via two-body processes or heating from a constant ultraviolet background source (Katz et al., 1996). Radiative transfer is believed to be important in a circumstellar disk, but is difficult to simulate realistically. Heat should propagate from the central star onto the outer layers of the disk, be transferred through the disk, and be re-radiated in the optically thin layers. Here we describe a parametrized form of cooling that attempts to capture some qualitative features of this process.

One form for the cooling term Λ is linear cooling with a constant cooling time: $\Lambda_a = u_a/\tau_{\text{cool}}$. This form of cooling has been implemented in *Gasoline* by the author. An alternative is a cooling time inversely proportional to the local angular velocity, which has been shown to dramatically decrease the stability of circumstellar disks, resulting in enhanced formation of giant planets via gravitational collapse (Gammie, 2001; Rice et al., 2003).

Chapter 3

EQUILIBRIUM DISK MODELS: GENERATING INITIAL CONDITIONS

To simulate the evolution of a circumstellar disk, we first need a starting condition. We do not simulate the formation of the central star and surrounding disk, rather we want a well-formed disk in equilibrium. We will then insert a planet into the disk and simulate the evolution away from the equilibrium state (see Chapters 4 and 5).

Expressions for the density, temperature and velocity in the disk completely specify the system. We will choose a functional form for parts of these distributions and derive the equilibrium values for the remaining variables. We then discretize the equilibrium state using a source of random numbers. The discretized system is then suitable for numerical simulation.

3.1 Equilibrium Conditions

The equilibrium state we seek is an azimuthally symmetric, differentially rotating disk; Equilibrium pressure forces keep individual parcels of gas on vertically supported circular orbits. Working in heliocentric cylindrical coordinates (r, θ, z) , the disk extends from $r = R_{\text{in}}$ to R_{out} . For a circumstellar gaseous disk, the important physical forces are the gravity of the central star, the self-gravity of the disk and gas pressure forces. We specify the complete temperature profile and radial component of the density profile. We then solve for the vertical component of the density distribution. The equilibrium circular velocity then exactly balances the physical forces arising from the distribution of mass in the disk.

Forces due to disk self-gravity and pressure support will be small relative to the gravity of the central star because we are using a disk mass small (at most one-fifth) in comparison to the mass of the central star. Thus we will make approximations to find analytic expressions for the equilibrium state.

3.1.1 Temperature Profile

Although our simulations are three-dimensional, we pick a simple temperature profile with no vertical dependence. This choice is motivated by our belief that, in the thin disks we are interested in, the distance from the central star is the most important factor determining the temperature in the disk.

The temperature profiles of circumstellar disks around Sun-like stars are not well known. Most investigations choose a power-law model for the temperature profile, $T(r) \propto r^{-q}$, and attempt to find the appropriate index q . For example, by fitting infrared spectra, Beckwith et al. (1990) found that many young circumstellar disks had profiles with $q = 1/2$. Theoretical models of a thin disk heated only by stellar irradiation give $q = 3/4$ (Beckwith and Sargent, 1993). In our own Solar System, cosmochemical evidence from meteorites suggest much hotter temperatures than the scale set by either of these power laws (Boynton, 1985; Boss, 1998). We assume that either such high temperatures occurred only briefly, or that the midplane temperature can be much greater than the surface temperature. Boss (2002) used a profile derived from calculations of radiative transfer, finding a very steep $q = 3$ profile within 4–9 AU. See Boss (1998) for a review of temperature profiles in circumstellar disks.

We choose the power-law profile

$$T(r, z) = T(r) = T_0 \left(\frac{r}{r_0} \right)^{-1} \quad (3.1)$$

where r_0 sets the length scale of the system, where the temperature is T_0 . This choice yields a disk with constant aspect ratio (i.e. the disk is not flared). This is largely a choice of convenience, and has been used in several previous simulations of

similar disk–planet systems (Lubow et al., 1999; Kley et al., 2001; Bate et al., 2003b; Papaloizou and Nelson, 2003; Nelson and Papaloizou, 2003; Papaloizou et al., 2004; Nelson and Papaloizou, 2004). Using $q = 1/2$ is also common (Nelson et al., 1998; Nelson and Benz, 2003a,b).

3.1.2 Density Distribution

To find the vertical density distribution in the disk, consider the forces acting in the vertical direction on a parcel of gas at radius r and height z . Imagine the parcel to be a cylinder with cross-sectional area $dA = r dr d\theta$ and height dz , and therefore a mass of $dm = \rho(r, z) r dr d\theta dz$. The vertical component of the disk self-gravity is negligible compared to the gravity of the central star, so in equilibrium

$$0 = F_{\text{star's gravity}} + F_{\text{gas pressure}} = -GM_{\star}dm \frac{z}{(r^2 + z^2)^{3/2}} + \frac{dP}{dz} dz dA \quad (3.2)$$

Expressing this as a function of the density, using the ideal gas law ($P = \rho k_B T / \mu$, where μ is the mean molecular weight of the gas) and that the imposed temperature profile has no vertical dependence, we obtain the differential equation

$$\frac{d\rho}{dz} = -\frac{GM_{\star}\mu}{k_B T(r)} \frac{z}{(r^2 + z^2)^{3/2}} \rho \quad (3.3)$$

As written, the solution leads to a density distribution whose integral does not converge, i.e. gives a disk of infinite mass. Because a temperature profile that depends only on the radial distance is applicable only to a thin disk, we expand to first order in z/r and solve to find a Gaussian functional form

$$\rho(r, z) = \rho_0 f(r) e^{-\frac{z^2}{2H(r)^2}} \quad (3.4)$$

where f is an arbitrary dimensionless function of r , ρ_0 sets the density scale and $H(r) = \left(\frac{k_B T(r)}{\mu GM_{\star}} r^3 \right)^{1/2}$ is the scale-height of the disk. With an appropriate choice for $f(r)$ this yields a disk of finite mass.

Using Equation 3.1, the chosen temperature profile gives a constant $\eta \equiv H(r)/r$, the aspect ratio of the disk. Using small η guarantees that the expansion of Equation 3.3 in z/r is a good approximation. Integrating Equation 3.4 over z we obtain

$$\Sigma(r) = \int_{-\infty}^{\infty} \rho(r, z) dz = \sqrt{2\pi} \rho_0 \eta r f(r) \quad (3.5)$$

Theoretical and observational arguments suggest a surface density profile $\Sigma \propto r^{-3/2}$ (Hayashi et al., 1985; Beckwith et al., 1990), so we take $f(r) = (r/r_0)^{-5/2}$. A power law with this index for the surface density is common in simulations of protoplanetary disks (Nelson and Benz, 2003a; Rafikov, 2002). The final expression for the density is

$$\rho(r, z) = \rho_0 \left(\frac{r}{r_0} \right)^{-5/2} e^{-\frac{z^2}{2\eta^2 r^2}} \quad (3.6)$$

for $R_{\text{in}} < r < R_{\text{out}}$ and $\rho = 0$ elsewhere, yielding a total disk mass of

$$M_D = \int_0^{2\pi} d\theta \int_{-\infty}^{\infty} dz \int_{R_{\text{in}}}^{R_{\text{out}}} r dr \rho(r, z) = 2 (2\pi)^{3/2} \rho_0 \eta r_0^{5/2} \left(\sqrt{R_{\text{out}}} - \sqrt{R_{\text{in}}} \right) \quad (3.7)$$

Now pick the disk mass M_D , extent R_{in} to R_{out} , aspect ratio η (equivalently, T_0) and distance scale r_0 to determine ρ_0 and the scale of the system units. Given Equation 3.6 and the defining constants mentioned above, we can evaluate the density everywhere in the disk. Using the density, we now calculate forces.

3.1.3 Gravitational Potential of a Disk

Gravitational forces from the central star and the disk itself are included. The vertical component of the star's gravity was explicitly countered by the vertical pressure gradient in Equation 3.2, so we need only consider the radial component due to a point mass at the origin,

$$a_{\text{star}}(r, z) = -GM_{\star} \frac{r}{(r^2 + z^2)^{3/2}} \quad (3.8)$$

The potential due to the disk is more complicated. We are interested in thin disks, so approximate the disk as two dimensional for this calculation and only consider

acceleration in the radial direction. Consider a ring of mass M and radius R centered on the origin. In the plane of the ring, the potential is (from Jackson (1999), making the substitutions $1/4\pi\epsilon_0 \rightarrow G$ and $q \rightarrow -M$)

$$\Phi(r) = -GM \sum_{l=0}^{\infty} \frac{r_{<}^l}{r_{>}^{l+1}} P_l(0)^2 \quad (3.9)$$

where $r_{<}$ ($r_{>}$) is the smaller (greater) of r, R and P_l is the Legendre polynomial of order l . A disk from R_{in} to R_{out} is a series of rings, each with mass $2\pi r dr \Sigma(r)$. The potential of the entire disk is thus the integral

$$\Phi(r) = -G \int_{R_{\text{in}}}^{R_{\text{out}}} 2\pi r' dr' \Sigma(r') \sum_{l=0}^{\infty} \frac{r_{<}^l}{r_{>}^{l+1}} P_l(0)^2 \quad (3.10)$$

We are only interested in the potential inside the disk:

$$\Phi(R_{\text{in}} < r < R_{\text{out}}) = -2\pi G \sum_{l=0}^{\infty} P_l(0)^2 \left[\int_{R_{\text{in}}}^r r' dr' \Sigma(r') \frac{r'^l}{r^{l+1}} + \int_r^{R_{\text{out}}} r' dr' \Sigma(r') \frac{r'^l}{r^{l+1}} \right] \quad (3.11)$$

Using the surface density of interest (Equation 3.5) we obtain

$$\begin{aligned} \Phi(R_{\text{in}} < r < R_{\text{out}}) &= -(2\pi)^{3/2} G \rho_0 \eta r_0^{5/2} \sum_{l=0}^{\infty} P_l(0)^2 \frac{2}{2l+1} \\ &\quad \times \left[2r^{-1/2} - \left(\frac{R_{\text{in}}}{r}\right)^{l+1} R_{\text{in}}^{-1/2} - \left(\frac{r}{R_{\text{out}}}\right)^l R_{\text{out}}^{-1/2} \right] \end{aligned} \quad (3.12)$$

Finally, to obtain the acceleration due to the disk we take the gradient of the potential:

$$\begin{aligned} a_{\text{disk}}(R_{\text{in}} < r < R_{\text{out}}) &= -\frac{\partial \Phi}{\partial r} = -(2\pi)^{3/2} G \rho_0 \eta r_0^{5/2} \sum_{l=0}^{\infty} P_l(0)^2 \frac{2}{2l+1} \\ &\quad \times \left[r^{-3/2} - (l+1) \left(\frac{R_{\text{in}}}{r}\right)^{l+2} R_{\text{in}}^{-3/2} + l \left(\frac{r}{R_{\text{out}}}\right)^{l-1} R_{\text{out}}^{-3/2} \right] \end{aligned} \quad (3.13)$$

3.1.4 Pressure Gradients

Again making the two-dimensional approximation, we use the surface density and the ideal gas law to calculate the acceleration due to the radial pressure gradient:

$$a_{\text{pressure}}(r) = -\frac{1}{\Sigma(r)} \frac{dP}{dr} = -\frac{1}{\Sigma(r)} \frac{k_B}{\mu} \left(T(r) \frac{d\Sigma}{dr} + \Sigma(r) \frac{dT}{dr} \right) = \frac{5}{2} \frac{k_B T(r)}{\mu} \frac{1}{r} \quad (3.14)$$

where the coefficient of the last expression is determined by the power law indices we have chosen.

3.1.5 Equilibrium Velocity

To find the velocity of a circular orbit in this disk, we balance the acceleration due to the forces detailed above by the centripetal acceleration of circular motion:

$$\mathbf{v}(r, z) = (-r [a_{\text{star}}(r, z) + a_{\text{disk}}(r) + a_{\text{pressure}}(r)])^{1/2} \hat{\theta} \quad (3.15)$$

We now know the density, temperature and circular velocity everywhere in the disk. We discretize the analytic expressions by placing equal-mass particles according to the density distribution, assigning them velocities and temperatures appropriate to their position. This is done by assigning particle positions using a random number generator with the appropriate distribution.

3.2 Manipulating Random Numbers

Random numbers are used in all areas of computational science. For example, when constructing initial conditions for astrophysics simulations, particle properties are often determined by drawing them from a random number distribution. The desired layout of the particles determines the particular distribution to use. Here we describe how to manipulate random number distributions, with an eye to changing a uniformly distributed source of random numbers to an arbitrary distribution. This section builds on the discussion of random number distributions in Zwilliger (1996) and Knuth (1981). The following applies to continuous, as opposed to discrete, distributions of random numbers.

3.2.1 The Probability Density Function

Let X be a random number. Then the probability density function (PDF) $f(x)$ of the distribution is defined by $f(x) dx$ being the probability that $X \in [x, x + dx]$.

By definition we have $\int_{-\infty}^{\infty} f(x) dx = 1$. An expression for f completely describes the distribution of the random number source. The cumulative distribution function (CDF) $F(x)$ is the probability that $X < x$, and can be expressed as a function of the PDF:

$$F(x) = \int_{-\infty}^x f(x') dx' \quad (3.16)$$

Note that we can immediately say that $0 \leq F(x) \leq 1$, $F(-\infty) = 0$, and $F(\infty) = 1$.

3.2.2 Pseudorandom Number Generators

There are many software routines for generating pseudorandom numbers. While some libraries provide several specialized distributions, they all provide a source of random floating-point numbers uniformly distributed between 0 and 1. One popular, efficient, and well-tested library of random number generators is available as one of the Boost C++ libraries (Boost Developers, 2004). The Mersenne twister generator of this library is used in this work (Matsumoto and Nishimura, 1998).

3.2.3 Manipulating a Distribution

Given an arbitrary desired non-uniform distribution function, can we manipulate uniformly distributed random deviates to follow the desired distribution? If the desired distribution is invertible, this can be done quite simply.

Given a uniformly distributed random deviate U and a desired CDF $F(x)$, let $X = F^{-1}(U)$ where we have the inverse $F^{-1}(F(x)) = x$ for all x in the domain of F . If we can show that $F(x)$ is the probability that $X \leq x$, then we can use the manipulated X as the desired random deviate. Consider the probability that $X \leq x$. Given the definition of X , this is equal to the probability that $F^{-1}(U) \leq x$. Apply F to both sides, and we get the probability that $U \leq F(x)$. Now because U is uniformly distributed and F is continuous and strictly increasing (requirements for invertibility) from 0 to 1, this probability is equal to $F(x)$. Therefore we have shown that X is

distributed according to $F(x)$.

3.3 Distributing Particles Randomly

In an SPH scheme, you often want to create initial conditions by placing particles randomly according to a distribution. Because SPH approximates a continuous fluid, you usually have an expression for the density everywhere in the simulation. Given a density, how do you place equal-mass particles to simulate that distribution of mass? This can be done by relating a mass density to a probability density, defining a distribution. You then use this distribution to randomly pick the particle positions.

For example, given a separable density field $\rho(x, y, z) = \frac{M}{r_0^3} f(x)g(y)h(z)$ where M is the total mass of the system, we identify three probability densities f , g , and h . These can then be used to pick the components of the position. If each of N particles is assigned a mass of M/N , the ensemble will approximate the continuous density field $\rho(x, y, z)$.

3.3.1 The Disk Model

The disk geometry described by Equation 3.6 is not immediately separable and requires a slightly more complicated treatment. Since the disk is azimuthally symmetric, the azimuthal angle is clearly separable and chosen uniformly distributed between 0 and 2π . The radial component can be chosen by relating the vertically averaged surface density $\Sigma(r)$ to a probability distribution $f(r)$.

$$1 = \frac{1}{M_D} 2\pi \int_{R_{\text{in}}}^{R_{\text{out}}} \Sigma(r) r dr = \int_{R_{\text{in}}}^{R_{\text{out}}} f(r) dr \quad (3.17)$$

$$f(r) = \frac{1}{2(\sqrt{R_{\text{out}}} - \sqrt{R_{\text{in}}})} r^{-1/2} \quad (3.18)$$

The CDF for this distribution is

$$F(r) = \int_{R_{\text{in}}}^r f(r') dr' = \frac{\sqrt{r} - \sqrt{R_{\text{in}}}}{\sqrt{R_{\text{out}}} - \sqrt{R_{\text{in}}}} \quad (3.19)$$

the inverse of which is

$$F^{-1}(r) = \left(r \left(\sqrt{R_{\text{out}}} - \sqrt{R_{\text{in}}} \right) + \sqrt{R_{\text{in}}} \right)^2 \quad (3.20)$$

The radial component of a particle’s position is thus taken as $F^{-1}(U)$ where U is a uniformly distributed random deviate.

To choose the vertical component, note that for a given radius r , the vertical distribution is proportional to a Gaussian with mean $\mu = 0$ and variance $\sigma^2 = \eta^2 r^2$. Thus we choose the z component of a particle’s position from a normal distribution, after choosing r .

We are now prepared to write down the complete algorithm for constructing the initial disk model. First, the scale of the problem is set by specifying the constants r_0 , R_{in} , R_{out} , M_D and η . The total number of gas particles determines the mass of each individual particle. For each particle, the position is chosen randomly as described above. The temperature of each particle is set by its position in the disk. The velocity is set in the azimuthal direction to balance the physical forces (Equation 3.15). In addition, a softening length for the gravitational force is set, as described in Section 5.3.2. Finally, for migration simulations, a planet is inserted into the disk with a specified mass, semi-major axis, softening and circular velocity.

3.4 “SPH-ifying” a Grid Simulation

There are two major techniques for numerical hydrodynamics: finite difference methods on a spatial grid, and smoothed particle hydrodynamics. To accommodate the different strengths and weaknesses of the two techniques, it is useful to compare the solutions to a single problem obtained using both methods. An important first step is using similar initial conditions. Here we describe a method for converting a grid simulation output into a format suitable for SPH. This method is then applied to the initial conditions of a grid simulation.

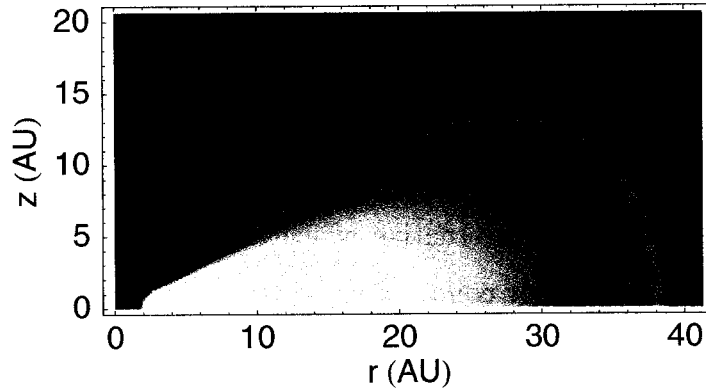


Figure 3.1: The density in a circumstellar disk around a $0.5 M_{\odot}$ star, taken from a grid model. The grid is two-dimensional, representing a slice through an azimuthally and vertically symmetric disk. The color scale represents the logarithm of the density.

3.4.1 Grid Quantities

An SPH simulation provides a fixed mass resolution, as it follows constant mass particles through space. In contrast, a grid simulation provides fixed spatial resolution, monitoring the mass flowing through a point in space. As an SPH particle contains several quantities that are affected by physical forces, so does a grid point. For a snapshot of a azimuthally symmetric two-dimensional grid model of a disk, the quantities at each grid point are the density, temperature and angular velocity. Figure 3.1 shows the gas density in the disk taken from a grid model.

In Section 3.3 we used an analytic expression for the density to guide the placement of particles. The grid model gives the density at regularly spaced points in space, which cannot be easily mapped to a closed-form expression. We must use a different technique to place particles according to the new density distribution. Then for each particle we assign a temperature and circular velocity, interpolated from the grid.

3.4.2 The Acceptance/Rejection Method

Section 3.2.3 describes how to construct non-uniform random deviates, given a uniform source of random deviates and an invertible distribution function. The acceptance/rejection method is an alternative which can be used when the CDF of the desired distribution is not easily computable. Consider a two-dimensional probability distribution $p(x, y)$ over the domain $x \in [x_1, x_2]$, $y \in [y_1, y_2]$. If we have a source of random deviates following distribution $f(x, y)$ such that $f(x, y) \geq p(x, y)$ for all x, y in the domain, then we can use $p(x, y)$ as an acceptance criterion to choose random numbers X, Y such that they are distributed with $p(x, y)$. Let X be a random deviate uniformly distributed on $[x_1, x_2]$ and Y be uniformly distributed on $[y_1, y_2]$. Now take Z to be uniformly distributed on $[0, f(X, Y)]$. If $Z < p(X, Y)$ then we accept the pair (X, Y) , else we reject the pair and start over. Because we have used the desired distribution p as the acceptance criterion, the pair of random deviates (X, Y) will be distributed according to $p(x, y)$.

In certain cases we may be able to find an f that is “close” to p , thus reducing the average number of rejections encountered while choosing a deviate using this method. If p is not pathological, it is often easier and not prohibitively expensive to choose f to be a constant, the natural choice being $f(x, y) = \max_{x' \in [x_1, x_2], y' \in [y_1, y_2]} p(x', y')$. For a more detailed explanation of the acceptance/rejection method in one dimension, see Press et al. (1992); Zwilliger (1996).

3.4.3 Interpolating Quantities

To assign positions to SPH particles using the density from a grid model, we use the acceptance/rejection method, identifying the mass density $\rho(r, z)$ with a probability density

$$p(r, z) = \frac{4\pi}{M_D} r \rho(r, z) \quad (3.21)$$

and choosing $f(r, z) = \max p(r, z)$. This method determines the r and z for each particle. The grid model assumes symmetry about the $z = 0$ plane, so we alternate the sign of z when constructing the fully three-dimensional particle model. The azimuthal angle is distributed uniformly between 0 and 2π .

To use the acceptance/rejection method, we need to evaluate $p(r, z)$ for any r, z within the grid limits. Once the position has been assigned, we need to determine the temperature and angular velocity at that arbitrary point. To handle this, we interpolate values over the density, temperature and angular velocity grids. The grid is two-dimensional, so we use bilinear interpolation (Press et al., 1992).

Following this technique, we can construct a disk model composed of SPH particles, which we can evolve with our standard simulation tool. Given the results of the accompanying grid simulation, we can examine the differences and similarities between the two techniques. Such a test is left for a later work.

Chapter 4

MIGRATION AND FORMATION PAPER

The remainder of this chapter is the body of the paper originally published as Lufkin, Quinn, Wadsley, Stadel, and Governato (2004). The only difference is a correction to Equation 4.1 and the use of color figures. The paper is © 2004 The Royal Astronomical Society. Note that British spellings are used in this chapter. The simulation initial conditions it describes were constructed as detailed in Chapter 3.

4.1 Paper Abstract

We present global three-dimensional self-gravitating smoothed particle hydrodynamics (SPH) simulations of an isothermal gaseous disc interacting with an embedded planet. Discs of varying stability are simulated with planets ranging from 10 Earth masses to 2 Jupiter masses. The SPH technique provides the large dynamic range needed to accurately capture the large-scale behaviour of the disc and the small-scale interaction of the planet with surrounding material. Most runs used 10^5 gas particles, giving us the spatial resolution required to observe the formation of planets. We find four regions in parameter space: low-mass planets undergo Type I migration; higher-mass planets can form a gap; the gravitational instability mode of planet formation in marginally stable discs can be triggered by embedded planets; discs that are completely unstable can fragment to form many planets. The disc stability is the most important factor in determining which interaction a system will exhibit. For the stable disc cases, our migration and accretion time-scales are shorter and scale differently from previously suggested.

4.2 Introduction

Planet formation is believed to occur in discs of gas and dust around young stars. Observations of circumstellar discs in multiple wavelengths reveal the initial conditions for planet formation (McCaughrean, Stapelfeldt, and Close, 2000; Wilner and Lay, 2000). Detection of extrasolar planets has provided a diverse set of final states, including a statistically significant number of planets with masses comparable to that of Jupiter on orbits very close to their parent star, so-called ‘Hot Jupiters’ (for a review see Marcy and Butler, 2000, and exoplanets.org for an up-to-date catalogue). Formulating an acceptable theory of giant planet formation in such an environment has proved difficult (Wuchterl, Guillot, and Lissauer, 2000, and references therein). Instead planet migration has become the standard theory to explain these interesting companions.

The interaction between a gaseous disc and an embedded protoplanet is a complex, highly non-linear process. Several phenomena have been classified, including the accretion of planetesimals, the accretion of gas, the exchange of angular momentum via tidal forces and planet formation via gravitational instability. How these behaviours combine is determined by the initial conditions, for example the mass and temperature of the disc and the location of an embedded planet. We can sort all possible interactions into a few categories: linear migration via tidal interaction, gap formation and viscous migration, and planet formation via gravitational instability. All these interactions have previously been investigated separately. Here we examine how the interactions are related and how the initial conditions determine which behaviour will be exhibited.

The dynamics of low-mass planets in gaseous discs have been explored both theoretically and numerically. The exchange of orbital angular momentum between disc and embedded satellite via spiral density waves excited at Lindblad resonances was discussed in Goldreich and Tremaine (1980). Ward (1997) gave arguments suggesting

that this will almost always lead to inward migration of the embedded planet, and derived an expression for the rate of this migration in the case where a planet does not open a gap in the disc (Type I migration). More recently, Tanaka, Takeuchi, and Ward (2002) gave an updated formula for the total torque on a planet, taking into account corotation resonances and mentioning three-dimensional (3D) effects. Previous numerical simulations have tested some of the theoretical assumptions, usually finding general agreement (e.g. Nelson et al., 2000b; D'Angelo et al., 2002).

In Type II migration the planet exerts a tidal torque greater than the disc viscous force, opening a gap. The migration time-scale is slowed, and accretion on to the planet is expected to slow or stop. Criteria for gap opening have been derived (Takeuchi, Miyama, and Lin, 1996; Rafikov, 2002) and examined numerically using two-dimensional (2D) grids (Bryden et al., 1999; D'Angelo et al., 2002). The accretion process has been simulated (Kley, 1999; Lubow, Seibert, and Artymowicz, 1999) finding mass-doubling times for Jupiter-mass planets in light discs to be of the order of 10^5 yr. For a review of Type I and II migration, see Thommes and Lissauer (2002).

The standard picture of migration is situated in a calm, stable disc. What if a single planet forms in a marginally stable disc? First hinted at by Armitage and Hansen (1999), the spiral density waves excited by a compact object (e.g. a rocky core formed via accretion of planetesimals) can lead to clump formation that would not otherwise occur. The fact that an embedded planet affects the disc density and flow locally has been known for some time; here we find that it can also have far-reaching (spatially and temporally) global effects.

Regardless of the embedded planets, some discs are themselves gravitationally unstable. This scenario of planet formation has been explored by Boss (1997, 2001) and recently by Mayer et al. (2002). In unstable discs many planets of Jupiter-mass or greater can be formed very quickly (hundreds of years). The newly formed proto-giant planets will violently tear through the disc, and their interaction as point masses will dominate the subsequent evolution of the system. This scenario is attractive because

it easily produces planets with properties similar to observed extrasolar planets. Furthermore, because the time-scale of formation is so small, any system even marginally unstable is likely to form planets during the much longer disc lifetime.

Much previous numerical work in this area has been limited to two-dimensional approximations, using grids with a relatively small spatial range, and ignoring the self-gravity of the disc. Some three-dimensional simulations have been performed recently (Bate et al., 2003b; D’Angelo et al., 2003), although these have still ignored self-gravity. The smoothed particle hydrodynamics (SPH) formalism was designed to be spatially adaptive. Our implementation uses variable time-steps, giving us temporal adaptivity. This allows us to explore the interaction with a much greater dynamic range. Our simulations are fully three-dimensional, have free boundary conditions, include the self-gravity of the disc and allow the planet to migrate and accrete freely.

Armed with these useful tools, we have simulated planets embedded in gaseous discs, for initial planet masses ranging from 10 Earth-masses to 2 Jupiter-masses, and disc masses ranging from 0.01 to 0.25 M_{\odot} . Previous investigations have focused on just one of the interactions described above, usually looking at lower-mass discs. Here we attempt to relate the interactions, and see how the choice of initial conditions determines the classification of the outcome. We draw an outline of interesting regions of parameter space, and present a few early results from each distinguishable region. We also discuss where our simulations differ from previous efforts and suggest that this is due to the more realistic system we are able to model. In future papers we will quantitatively address the specific phenomena we can simulate, such as gap opening criteria, gas accretion through the gap, Type I and II migration time-scales and the likelihood of triggered planet formation.

The plan of the paper is as follows. In Section 4.3 we describe the initial conditions of our models. The numerical technique is briefly discussed in Section 4.4 and our main findings are detailed in Section 4.5. Details of the results are discussed in

Section 4.6 and we conclude with Section 4.7.

4.3 Initial Conditions

We use power-law distributions for density and temperature profiles in our simulations, and the disc stability criterion and mass ratio are dimensionless, so our results should scale well. None the less, it is convenient to use conventional units when discussing our results. The central star was of $1 M_{\odot}$, and its potential was softened with a cubic spline on a length-scale of 0.4 AU. All simulations were performed in heliocentric coordinates, taking into account the back-reaction of the disc and planet on the star. Initially, the disc extends from 1 to 25 AU and is free to expand.

Temperature profile

Observations of protoplanetary discs do not put tight constraints on the temperature profile. Therefore, we adopt a power law for the radial temperature profile and choose an index which is equivalent to a constant aspect ratio H/r (where H is the scaleheight of the disc at a particular radius). Most of our simulations used $H/r = 0.05$ (which gives $T(5.2 \text{ AU}) = 102 \text{ K}$). This profile is similar to that suggested by the solar nebula model of Hayashi, Nakazawa, and Nakagawa (1985) and is common in other simulations of these phenomena. The temperature is capped at 5000 K within 0.1 AU of the star and limited below by 17 K outside of 30 AU.

Density profile

The minimum-mass solar nebula model suggests a power law for the vertically averaged surface density of $\Sigma(r) \propto r^{-3/2}$. The vertical structure of the disc is determined by the balance between the vertical component of the gravity of the central star and the vertical pressure support of the disc. If we assume no vertical variation in the temperature, the vertical density structure can be solved, yielding a scaleheight ex-

pressed as a function of the radius and the temperature at that radius. An expression for the density distribution is then

$$\rho(r, \theta, z) = \rho_0 r^{-5/2} e^{-z^2/2H(r)^2} \quad (4.1)$$

In a gravitationally stable disc we found this profile to be stable over many dynamical times, so we chose this initial distribution for all of our simulations. Our standard disc, $0.1 M_\odot$ extending from 1 to 25 AU, thus has $\Sigma(5.2 \text{ AU}) = 150 \text{ g cm}^{-2}$. For the gas particles of the disc, the initial positions are randomly drawn from the desired distribution. Initial velocities are chosen so that particles are on circular Keplerian orbits, modified slightly to account for the self-gravity of the disc and gas forces. In stable discs without embedded planets, the surface density does not change markedly with time except at the inner and outer edges. The outer edge expands slightly, due to the initial sharp drop in density. At the inner edge, particles migrate inward due to viscous forces, participating in a complex balance between the softened potential of the star, the smoothed gas pressure forces and Keplerian shear. These particles are much closer to the central star than the inner Lindblad resonance of the planet, so we do not believe they play a large role in determining the evolution of the planet. We have not investigated schemes for halting planet migration, which might involve removing the inner reaches of the disc.

The embedded planet

The initial mass of the planet particle was a parameter. We used planet masses ranging from $10 M_\oplus$ to $2 M_J$. The planet particle interacts via gravity only, and no gas drag is applied. Planets significantly more massive than a gas particle can capture gas particles, adding to the effective mass of the planet. These captured gas particles are not removed or treated specially; they remain as part of the envelope of the developing planet. The potential of the planet was spline-softened on a length-scale of one-fifth the initial Roche radius.

4.3.1 *An initial gap*

Sufficiently large planets can open a gap in the disc by exerting a tidal torque stronger than the local viscous angular momentum transfer. The balance between these forces determines the shape and width of the gap formed around such a planet, which can be calculated analytically by averaging over many orbits and assuming how and where the density waves are dampened. The formation of these gaps has been studied numerically before, primarily in light discs with heavy planets without allowing migration (Bryden et al., 1999), finding reasonable agreement with analytic models. For low-mass discs, the Type I migration time-scale may be sufficiently long for the standard explanation of gap formation to work. We found that planet migration and gap formation could not be decoupled. Therefore, we chose not to impose any initial gap, instead the formation of the gap is simulated in systems that produce one.

A Jupiter-mass planet embedded in an unperturbed disc without a gap is somewhat unphysical: how did the planet become so massive without affecting the disc? As seen in Fig. 4.3 below, the transition from Type I to Type II migration is very sudden, taking only a few orbital times. Therefore, the sudden appearance of a large planet in a calm disc is not entirely unreasonable, and we can imagine the following scenario: the planet forms, at a lower mass, further out in the disc, and undergoes Type I migration and accretion to obtain the location and mass we start with. To accurately model the capture of gas, the planet particle must be several times more massive than the gas particles. Therefore, future investigations using higher resolution should be able to push the initial planet mass lower.

4.3.2 *Equation of state*

We use an isothermal equation of state with a spatially fixed temperature profile. In doing so we are assuming that the disc temperature is controlled solely by the distance from the parent star, and that the energy of viscous heating is radiated away much

faster than the dynamical time-scale of the gas. We do not account for shielding, so we miss the detailed thermal structure of the clumps that form. Furthermore, clumps on elliptical orbits will heat up and cool down along their orbits. Boss (2002) has found that using a more realistic equation of state suppresses clump formation in marginally stable discs.

4.3.3 *Disc stability*

The stability of the disc is characterized by the Toomre Q criterion, defined as

$$Q = \frac{c_s \kappa}{\pi G \Sigma} \quad (4.2)$$

where c_s is the sound speed, κ is the epicyclic frequency, and Σ is the surface density of the disc. This criterion measures the susceptibility to a local instability. Global spiral waves can cause the local density to increase, leading to a local collapse. The power laws we have chosen for the temperature and density make $Q \propto r^{-1/2}$. Hence we expect instabilities, if produced, to occur in the outer regions of the disc.

4.4 *Numerical Realization*

To model the disc–planet system we used *Gasoline*, a tree-based particle code originally developed for cosmological simulations (Stadel, 2001; Wadsley et al., 2004). It implements smoothed particle hydrodynamics, a Lagrangian treatment of hydrodynamics for gas. It has been used previously on solar system-scale problems by Richardson et al. (2000) and Mayer et al. (2002). The code was modified to apply a fixed temperature profile to the particles. The equations of motion include the gravity and hydrodynamics of the gas disc. We do not include effects due to magnetic fields.

4.4.1 *Boundary conditions*

SPH is a Lagrangian technique, so we do not need to impose any boundaries. All the particles are allowed to move where the forces dictate. Particles are not deleted or

merged when they approach the central star or the embedded planet.

4.4.2 *Simulation parameters*

The tree-cell interaction opening angle we used was $\theta = 0.7$. Using a multi-stepping technique, the particle timesteps are picked according to the local density (with $\eta = 0.1$), and to satisfy the Courant condition (with $\eta_c = 0.4$). The largest possible timestep was set to be 2.5 yr, which is 1/50 the orbital time at the outer edge of the disc. The mean molecular weight of the gas is 2 AMU, corresponding to molecular hydrogen.

4.4.3 *Viscosity*

The SPH formalism treats viscosity differently from the Shakura & Sunyaev α prescription popular in finite difference schemes. No ‘real’ viscosity is added to the equations of motion. Because so little is known concerning the sources of real viscosity, we choose to err on the side of caution by introducing as little viscosity as possible into the system, in an attempt to model the fluid with as high a Reynolds number as possible. However, some artificial viscosity is necessary to stabilize the integration of the equations of motion. *Gasoline* includes the standard Monaghan treatment of artificial viscosity (Monaghan, 1992), including a Balsara switch that reduces viscosity in regions of strong shear (Balsara, 1995). Using the SPH formulation of the equations of motion, we can estimate the kinematic viscosity $\nu = \bar{\alpha} c_s h / 8$ (Nelson et al., 1998) associated with the artificial viscosity. This estimate is reasonable when there is little or no shocking (the presence of shocking adds artificial viscosity locally). There is strong shear in the disc, so the Balsara switch reduces this by a factor of approximately 5, yielding a viscous time-scale $\tau = r^2 / \nu \gtrsim 10^4$ yr everywhere for a run with 10^5 particles in a stable disc. Since this is at least 5–10 times longer than our simulations, we believe that artificial viscosity will not seriously affect the dynamics of the disc. To confirm this, we performed two additional simulations where

we halved and doubled the standard value of $\bar{\alpha} = 1$. The change in migration and accretion rates was approximately 5 per cent, which is less than the difference due to the random seed used to determine the initial particle locations. This indicates that artificial viscosity only affects the simulation as a numerical stabilizer, and does not introduce spurious physical effects.

4.5 Results

Looking first for planet migration, we start with planets embedded in light, stable discs. Increasing the disc and planet masses increases the rate of Type I migration, and brings us to gap formation and Type II migration. Continuing to marginally stable discs, we find that the density waves excited by an already formed planet can trigger gravitational instability in discs that would otherwise remain stable. Finally, we push the disc mass high enough so that no external trigger is needed to drive the gravitational collapse mode of planet formation.

Some of the factors that determine which category a system will end up in include the disc density profile and total mass, disc temperature, initial planet mass and orbital radius. We made choices for the density and temperature profiles, and varied the total disc mass, the initial planet mass and the orbital radius. We ran a simulation for each variation of the parameters for a given amount of time (326 yr), and classified the final result. We found the disc stability to be the most influential factor in determining the behaviour of a disc–planet system. The qualitative results of our suite of simulations can be seen in Fig. 4.1. We have arranged our results in a map of parameter space, illustrating the relative positions of the four interactions.

In stable discs (the upper region), planets of all masses exhibit Type I migration. In more massive discs, planets can open a gap, with a bias toward more massive planets. A precise measurement of the interface between these two regions can show us the criteria for gap opening. To differentiate between the regions labelled ‘Type

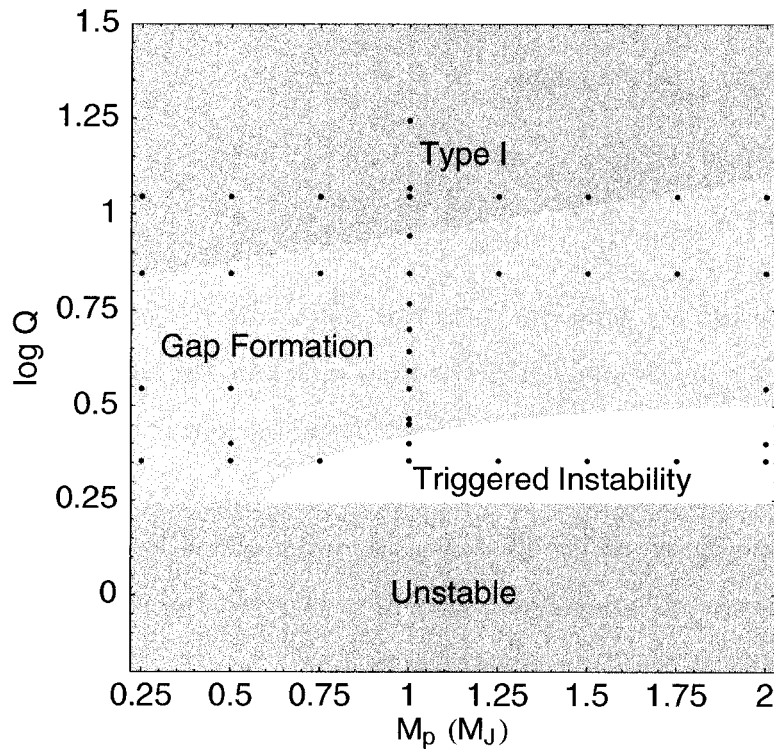


Figure 4.1: A parameter space map of disc–planet interactions. Q is the initial value of the Toomre criterion at the initial location of the planet. M_p is the mass of the planet, measured in Jupiter-masses. The points show the parameter values for the simulations we ran. See the discussion in the text. Since the totally unstable discs do not require planets, we cannot technically place them on this plot. However, if the disc is unstable, an additional planet will certainly not prevent instabilities from growing, so it is reasonable to label a region of this plot as unstable.

I' and 'Gap Formation' we look for the halting of the migration of the embedded planet within the time we simulated. See Sec. 4.6.4 for our definition of a gap and the reasoning behind it.

Some planets can trigger the formation of more planets via gravitational instability. This requires a marginally stable disc and a massive planet. The precise shape we have given this region is a guess based on our experience. In the bottom region, the disc is gravitationally unstable, even in the absence of embedded planets.

Note that the location of the boundaries between regions in this map are dependent on the time period of interest. We are deliberately simulating for only a few hundred years, to match the time-scale of triggered and wholly unstable planet formation. As such, many of the systems we classify as Type I do satisfy the standard thermal and viscous criteria for gap formation, and would form deeper depressions in the density profile and eventually shift from Type I to Type II migration if we evolved them several times longer. In addition, classification over such a short period of time is important, as we measure very high migration and accretion rates.

We have shown a two-dimensional slice through the three-dimensional parameter space we explored. While convenient and, we believe, largely accurate, this does hide some of the complexity we found. For example, we looked for triggered instability by placing planets at different orbital radii in different mass discs such that the value of Q was the same at the location of each planet. Since Q is dimensionless and we used power laws for the density and temperature, we might expect the same result in each system. However, the system with closer planet and more massive disc did not fragment, while the further planet and less massive disc system did. This may be due to edge effects or a non-linear dependence on the effectiveness of Q as a predictor of collapse.

4.5.1 *Type I migration*

Linear theory suggests that a seed planet in a light gas disc will undergo Type I migration with a rate that scales linearly with the planet mass and disc surface density. The planet excites density waves in the disc which torque back on the planet, leading to a change in the orbital angular momentum of the planet. As a result of the power-law index we chose for the density profile, we always see inward migration. During Type I migration the planet accretes gas from the disc with the help of the spiral density waves it excites. The internal waves take angular momentum from the disc, and the external waves give angular momentum back to the disc. On both sides, mass on nearby orbits is shepherded on to the planet.

Table 4.1 lists migration and accretion rates for the systems we classified as Type I migration. For the lighter discs, the migration rate is a constant function of time, whereas a more massive disc causes the migration rate to decrease as the simulation progresses and a gap is formed. We find that the accretion rate scales linearly with the planet mass and disc surface density. Further, the migration rate scales linearly with the disc surface density. However, changing the planet mass has almost no effect on the migration rate, confirming the findings of Nelson and Benz (2003a). If we compare our results with the analytic expression (eq. 70 from Tanaka et al. (2002)), we find our migration time-scales ($\tau_M = a/|\dot{a}|$) to be approximately 6 times shorter. Most previous simulations of Type I migration have kept the planet on a fixed circular orbit, and estimated migration time-scales by measuring the torque on the planet from the gaseous disc. Our migration timescales are actual measurements of the rate of change of the orbit of the planet.

4.5.2 *Gap formation*

More massive seed planets exert strong enough tidal torques to open a gap in the disc. By clearing the gas from the location of the Lindblad resonances, the torque

Table 4.1: Migration time-scales and accretion rates for Type I systems

M_p	M_d (M_\odot)	$-\dot{a}$ (AU/yr)	\dot{M} (M_\odot /yr)
2 M_J	0.01	1.2×10^{-3}	5.3×10^{-6}
1.75 M_J	0.01	1.2×10^{-3}	4.7×10^{-6}
1.5 M_J	0.01	1.4×10^{-3}	4.1×10^{-6}
1.25 M_J	0.01	1.1×10^{-3}	3.2×10^{-6}
1 M_J	0.01	1.0×10^{-3}	2.6×10^{-6}
0.75 M_J	0.01	1.4×10^{-3}	1.8×10^{-6}
0.5 M_J	0.01	1.1×10^{-3}	1.2×10^{-6}
0.25 M_J	0.01	8×10^{-4}	2.7×10^{-7}
1 M_J	0.0035	2.7×10^{-4}	6.4×10^{-7}
1 M_J	0.02	2.9×10^{-3}	5.7×10^{-6}
1 M_J	0.03	3.7×10^{-3}	8.5×10^{-6}
1 M_J	0.04	6.0×10^{-3}	1.3×10^{-5}
1 M_J	0.05	7.2×10^{-3}	1.9×10^{-5}
1 M_J	0.06	1.0×10^{-2}	2.3×10^{-5}

M_p is the planet's initial mass, M_d is the total disc mass, \dot{a} is the inward migration rate, \dot{M} is the accretion rate on to the planet. All these planets started out on circular orbits at 5.2 AU. The rates given are equilibrium values over at least the last 200 years of the simulation (which typically lasted 326 years). For the lighter discs the long-term values were reached immediately. We give values for particular simulations, so can give no meaningful error estimate. However, we completed several runs at different resolution, and usually found agreement within 10 per cent.

exerted on the planet by the disc vanishes. Previous theoretical work and simulations have suggested that formation of a gap drastically reduces the accretion rate on to the planet. We have not found this to be true. Even when the gap has cleared, the planet still perturbs the disc. These perturbations act to pull mass off the edges of the gap and on to the planet.

We found that gap formation was dependent more on the disc mass than the planet mass. This agrees with our claim that the self-gravity of the disc is important. At the start of the simulation the planet rapidly collects all the gas particles nearby, forming a gap within approximately 100 years. This accretion of gas at corotation is much faster than the accretion from close spiral arms or from gap edges, as described above. Since the migration time-scale is so short in the massive discs, there is significant migration during the gap formation. After the gap has formed, the migration stops or slows considerably. In $0.1 M_{\odot}$ discs, the accretion rate slows to a steady value of approximately $10^{-5} M_{\odot}/\text{yr}$, independent of the mass of the planet. Fig. 4.2 shows the mass of a planet and its accreted envelope as a function of time, for 0.5, 1, and 2 Jupiter-mass seed planets. By comparing with Fig. 4.3, the semi-major axis of the planet as a function of time, we see the accretion slow as the planet clears its gap (changes from Type I to Type II migration). The planet peels gas off the edges of the gap, as it catches up with particles on the outer edge and is caught by particles on the inner edge. Our results confirm that the formation of ‘Super-Jupiters’ is possible in massive discs. As Type I migration ceases, the planet is left in the gap with a non-zero eccentricity. We saw eccentricities of 0.01 to 0.04, comparable to the current eccentricity of Jupiter.

The time-scale for Type II migration is the viscous time-scale of the disc. Since we are actively trying to reduce the viscosity of the disc in our simulation, we do not see significant migration after the gap has formed.

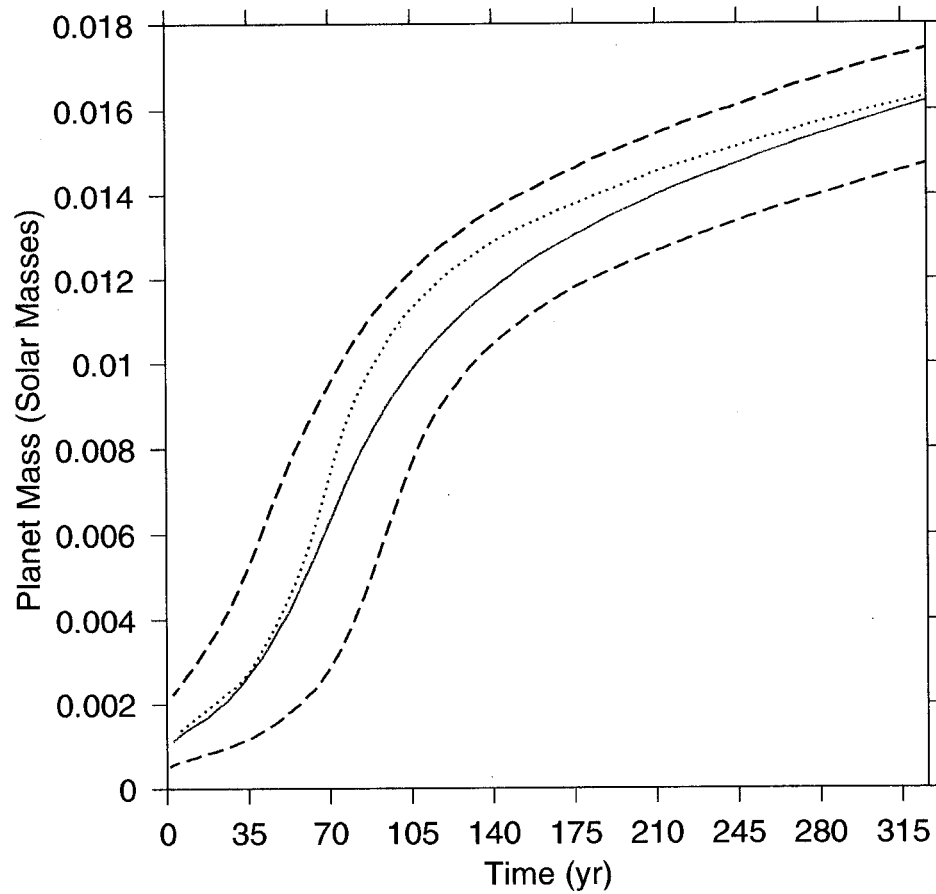


Figure 4.2: Gap formation scenario: The planet mass as a function of time in a $0.1 M_{\odot}$ disc, for different starting masses. The solid line is for an initial planet mass of $1 M_J$. The top dashed line is $2 M_J$ and the bottom dashed line is $0.5 M_J$. The dotted line is for a $1 M_J$ planet in the 2D approximation.

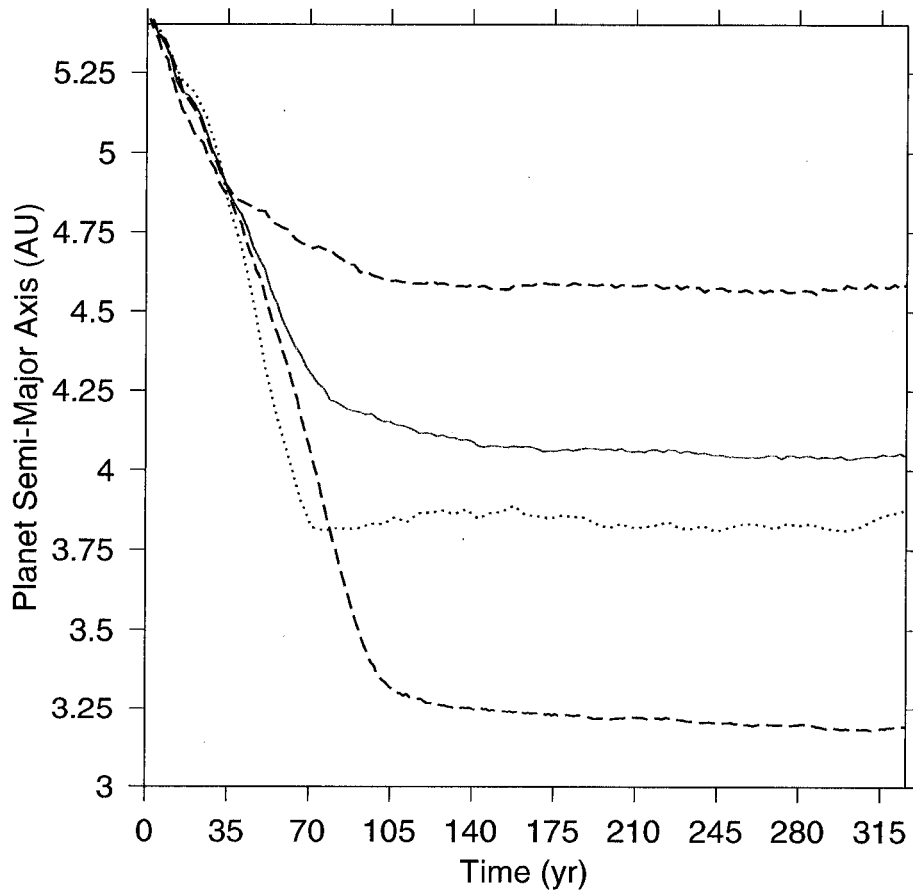


Figure 4.3: Gap formation scenario: The planet orbital radius as a function of time in a $0.1 M_{\odot}$ disc, for different starting masses. The solid line is for an initial planet mass of $1 M_J$. The top dashed line is $2 M_J$ and the bottom dashed line is $0.5 M_J$. The dotted line is for a $1 M_J$ planet in the 2D approximation.

4.5.3 Planet-triggered instability

If we reduce the stability of the disc, the spiral arms generated by an embedded protoplanet can trigger the gravitational instability. Such triggered clumps are always exterior to the seed planet that drives the instability, because Q decreases with distance from the star. The spiral arms of the planet must present a large enough density contrast to drive the local value of Q below 1. Since the unperturbed disc stability decreases with distance from the central star, for a fixed disc stability, a planet farther out from the central star is more likely to trigger the collapse. If we place a Jupiter-mass planet at 12.5 AU, a disc with $Q \gtrsim 1.6$ will fragment (see Fig. 4.4). Once the instability is triggered, the evolution of the system is very similar to the totally unstable case. The clumps form with non-negligible eccentricity, and strongly disturb the disc profile.

4.5.4 Unstable discs

If the disc is massive and/or cool enough, gravitational instabilities will cause it to collapse into bound objects, regardless of any embedded planets. Spiral waves propagate, and the density buildup in the arms causes the disc to fragment into gravitationally bound objects. Not one, but several of these bound objects are formed, and their interaction as effective point masses dominates the subsequent evolution. The previously smooth disc is ripped apart, as the clumps often have sizable eccentricities (see Fig. 4.5 for a progression of snapshots). We observe collisions, ejections, tidal stripping during close encounters, and violent disruption when plunging too close to the parent star. The eccentricities of these clumps can be high, and change as a result of dynamical interaction. As in Mayer et al. (2002), we find that the disc is unstable when Toomre's Q criterion is less than approximately 1.4. The clumps form when a spiral arm with sufficient amplitude reaches the outer regions of the disc.

For this regime we present a simulation that was unstable, a $0.2 M_{\odot}$ disc which

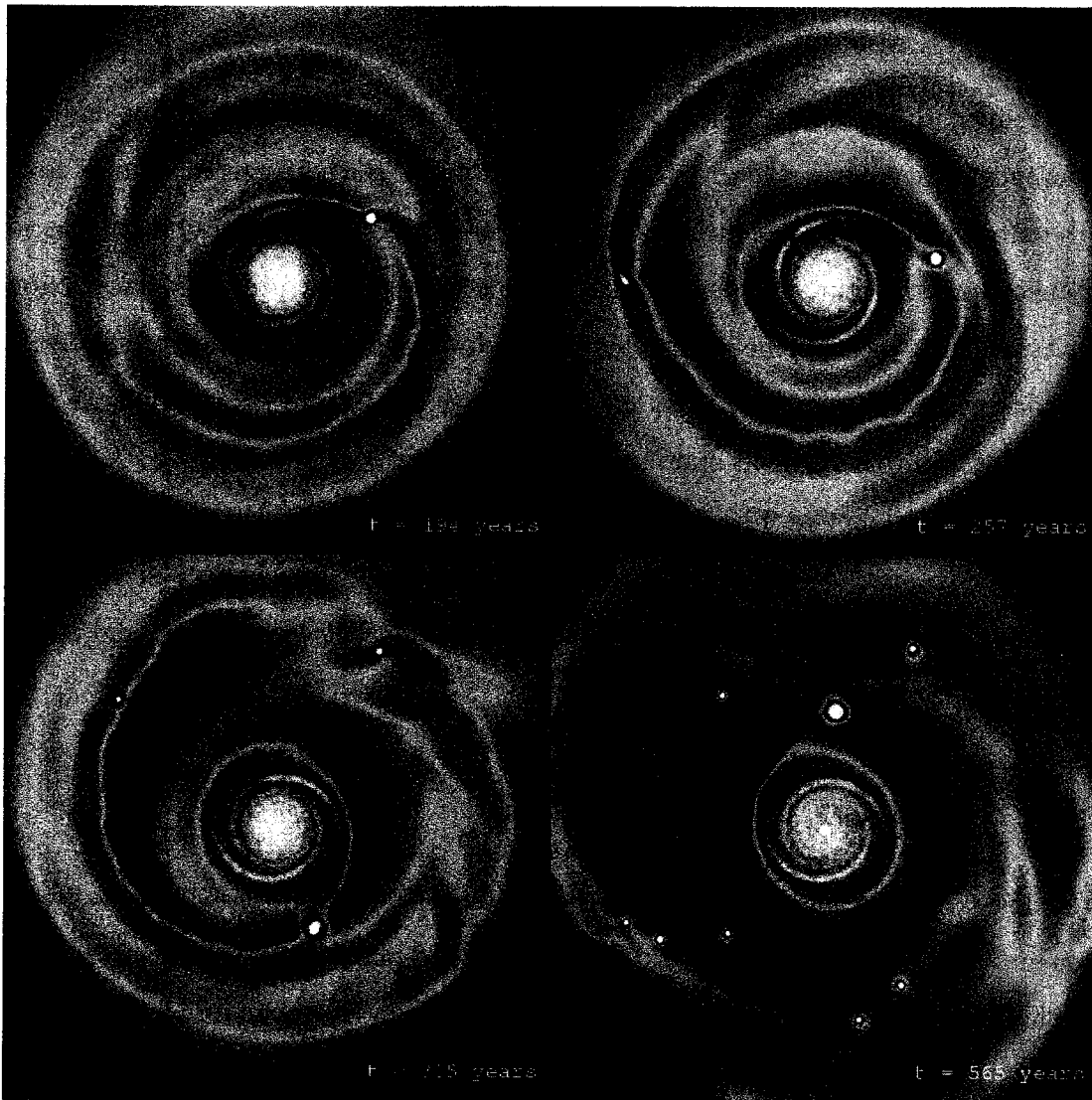


Figure 4.4: **Triggered Planet Formation:** A sequence of snapshots showing the gas density in a protoplanetary disc. At the location of the planet $Q = 2.2$, at the outer edge $Q = 1.6$. Early on, the planet drives spiral density waves in the outer regions of the disc. One of these waves increases the local density to the point where the region collapses. The planet continues to drive the spiral arms, leading to further clump formation. The process will continue until the disc material is sufficiently depleted. The width of each image represents 55 AU.



Figure 4.5: **Unstable Disc Planet Formation:** A sequence of snapshots showing the gas density in an unstable disc ($Q_{\min} = 0.8$). Early on, the spiral arms grow, after 150 years one of the spiral arms fragments into a few clumps. As time goes by, other arms fragment, in the outer disc, later, the leading arms of some clumps cause fragmentation of the inner disc. The width of each image represents 55 AU.

has $Q_{\min} = 0.8$. In this run, a spiral arm at approximately 20 AU fragments into four separate clumps after 153 years. Five more clumps form over the next 200 years. At this point, two clumps have developed strong leading arms, which fragment into approximately 10 more clumps over the next 30 years. Figs. 4.6 and 4.7 show the orbital and mass progression of some of the first clumps formed (the simulation forms many more clumps than detailed in the plots). We see large eccentricities and eccentricity changes, and mergers of several clumps. Once a significant fraction of the gas has been caught up in clumps, we expect that the furious production of new bound objects will cease, and the system will evolve as a set of point masses. After a long time (much longer than we have simulated) the system will reach dynamical stability, presumably with only a handful of objects remaining.

When a spiral arm fragments, it collapses to a rotating spheroid. All our planets formed initially with prograde rotation, however a later merger resulted in a counter-rotating clump. We are not modeling the cooling of the atmosphere of the planet accurately, so cannot comment on what the final spin of the planets will be. Because our simulations are three-dimensional, we can and do observe tilted planets, a result of interactions with other planets and vertical asymmetry in the spiral density waves.

Our work on wholly unstable discs extends the work of Mayer et al. (2002) to a larger region of parameter space, following the system for a longer period of time and spatially fixing the temperature profile. The critical value of Q that heralds collapse is quite sensitive to the equation of state used (Boss, 2002). A more detailed equation of state and more physical treatment of radiative transfer are necessary to determine how likely planet formation via gravitational instability is in a given disc. Note that, though we have evolved the system well past the initial collapse, we do not believe we have accurately modeled the detailed structure of the planets that form because we are using a simple equation of state. However, we have accurately followed the gravitational interaction of the multiple planets that form. We can therefore assert that, in planetary systems that formed via gravitational collapse, the disc torque

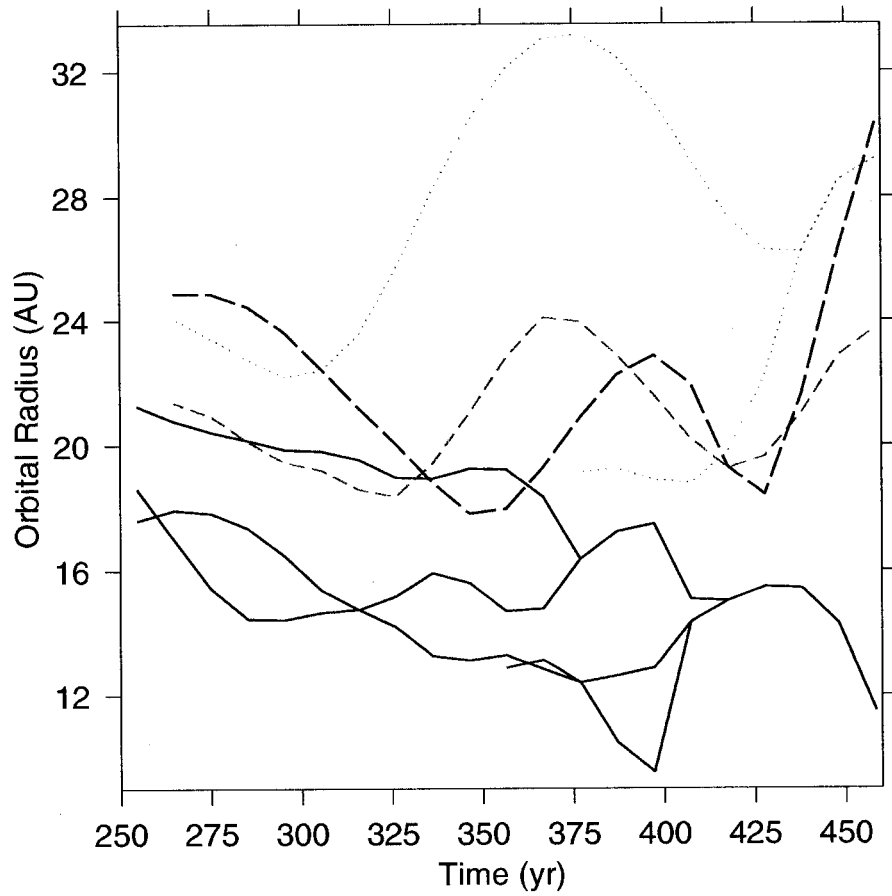


Figure 4.6: Formation in an unstable disc: The orbital radius of several clumps as a function of time. The lines begin when a clump forms. Clumps that will merge in the time shown have the same line style.

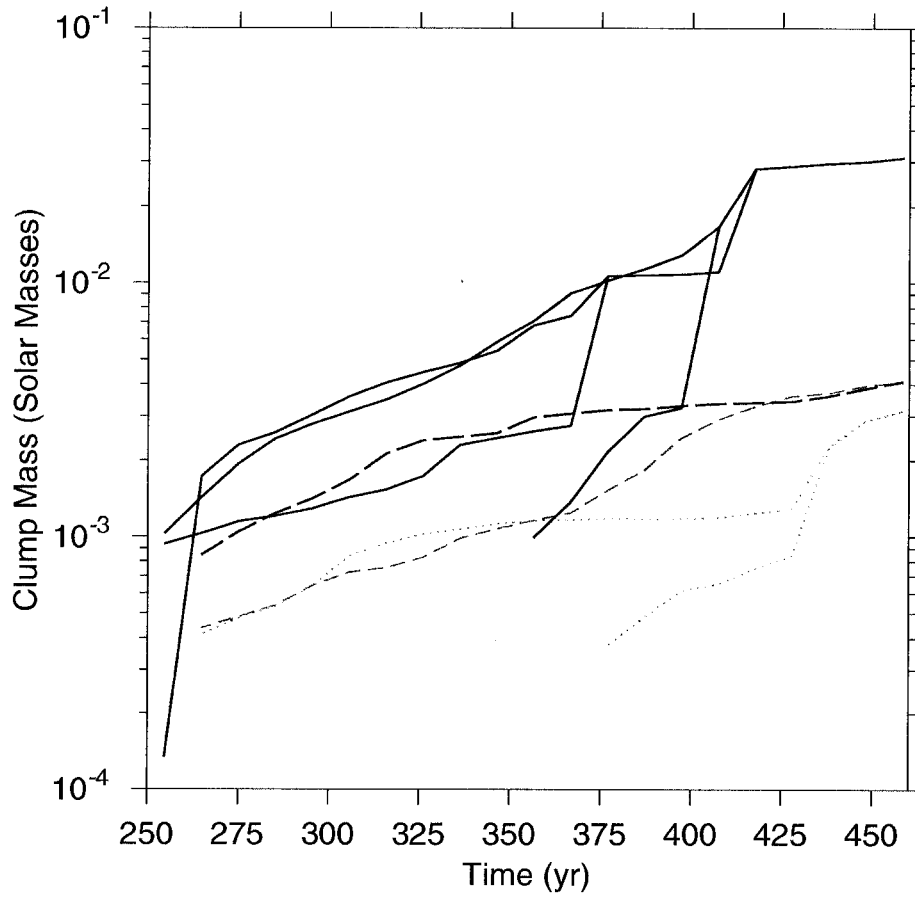


Figure 4.7: Formation in an unstable disc: The mass of several clumps as a function of time. The lines begin when a clump forms. Clumps that will merge in the time shown have the same line style.

theory of migration does not play a role, as the two-body interactions completely dominate the orbital evolution of the planets.

4.6 Discussion

Here we describe how we calculated the mass of the planet, some tests we performed, further discussion of our migration results, and how we define and use the word ‘gap’ in this work.

4.6.1 Mass of the planet

The gas particles that are captured by the planet are not removed from the simulation or added to the planet particle. They continue to orbit in the disc along with the planet. When we give results for accretion rates we have to calculate a mass of the whole planet, including the initial point mass and the captured gas. We use a simple criterion to determine whether or not a gas particle counts toward the mass of the planet: a particle must be within the Hill sphere of the planet and have density greater than the Hill density (the planet mass divided by the volume of the Hill sphere). Since the Hill sphere depends on the planet mass, this process is iterated until the planet no longer grows, starting from the initial planet particle.

4.6.2 Resolution issues

Our standard run for Type I migration is a $0.01 M_{\odot}$ disc with a Jupiter-mass planet starting on a circular orbit at 5.2 AU. We simulate the system for 326 years (approximately 28 orbits) and calculate accretion and migration rates as a function of time. Over this time period the migration and accretion rates are constant, and the planet migrates inward approximately 0.3 AU and grows in mass to approximately $1.8 M_{\text{J}}$. We ran this model at several resolutions to check for convergence. At resolutions of 20000 to 400000 particles the accretion rates matched to within 5 per cent and

the migration rates to better than 1 per cent. Given this agreement, we chose 10^5 particles as our standard resolution.

The results of two 10^5 particle runs can be seen in Fig. 4.8. Each simulation initially has $\Sigma(r) \propto r^{-3/2}$, aspect ratio $H/r = 0.05$, and an embedded Jupiter-mass planet initially on a circular orbit at 5.2 AU. The two density profiles shown are for disc masses of 0.1 and 0.01 M_{\odot} , after 326 years. The disc is three-dimensional, has free boundary conditions, and self-gravity is included. The density profiles can be compared to the results of previous simulations, for example fig. 3 of Nelson and Benz (2003a) and fig. 10 of Kley (1999). Those simulations are both two-dimensional, treat viscosity differently, and apply boundary conditions at the inner and outer edges of the disc.

4.6.3 Migration rate differences

The Type I migration rates we found were higher than most previous numerical and semi-analytical studies. However they agree fairly well with a recent simulation of Nelson and Benz (2003a), which does include the self-gravity of the disc.

We believe our treatment of the vertical dimension and the disc self-gravity is correct, and so the discrepancy should reveal invalid assumptions made in the linear theory of migration. Self-gravity always acts to increase the magnitude of density perturbations, so we would expect that the torques arising from these perturbations would be correspondingly increased, but we have not completed any simulations without self-gravity, so cannot comment further. To determine the effect of including the vertical dimension of the disc, we did several runs where all particles were constrained to the $z = 0$ plane. For light discs, the 2D case consistently gave accretion rates lower than the 3D case by at least 20 per cent. For more massive discs, the 2D case appears to give a slightly higher accretion rate during gap formation but again a lower rate after the gap has formed (see Fig. 4.2). The difference in migration rates between 2D and 3D simulations was not clear.

4.6.4 *Defining a gap*

Determining if and when a planet forms a gap in a disc is a non-trivial problem. By what percentage must the density decrease around a planet to be called a gap, and how far must this density depression reach? These criteria necessarily invoke an arbitrary number. Fig. 4.8 shows an azimuthally and vertically averaged surface density of two simulations with different disc masses. In both cases the gas density near the planet has been markedly reduced, and these depressions could be called gaps. The planet in the heavier disc has stopped migrating (see Fig. 4.3). In the lighter disc, however, the planet continues to migrate inward at a rate independent of the depth of the density depression. Therefore, we choose to use the word ‘gap’ only when its dynamical effects are apparent, i.e. when the planet has stopped migrating. This is how we chose between the ‘Type I’ and ‘Gap Formation’ regions when classifying simulations for Fig. 4.1.

4.7 *Conclusion*

This work presents the first results from our ongoing investigation of planet formation and migration. It is a pioneering application of global SPH simulations to a field previously examined primarily with Eulerian grid-based simulations. Using the new technique, we have measured migration and accretion time-scales, witnessing Type I migration and gap formation. Our results for this region partially qualitatively agree with the linear theory of interaction with spiral density waves. We have observed planet formation via disc fragmentation, including a cascade effect from a single starter planet. Using massive discs, we find that it is easy to form large (tens of Jupiter masses) planets on a short time-scale (hundreds of years). If planets form via gravitational instability, the theory of migration via disc torques is not applicable.

To obtain an overview of gaseous disc-embedded planet interactions, we performed a suite of simulations, varying the planet mass, the initial location of the planet, and

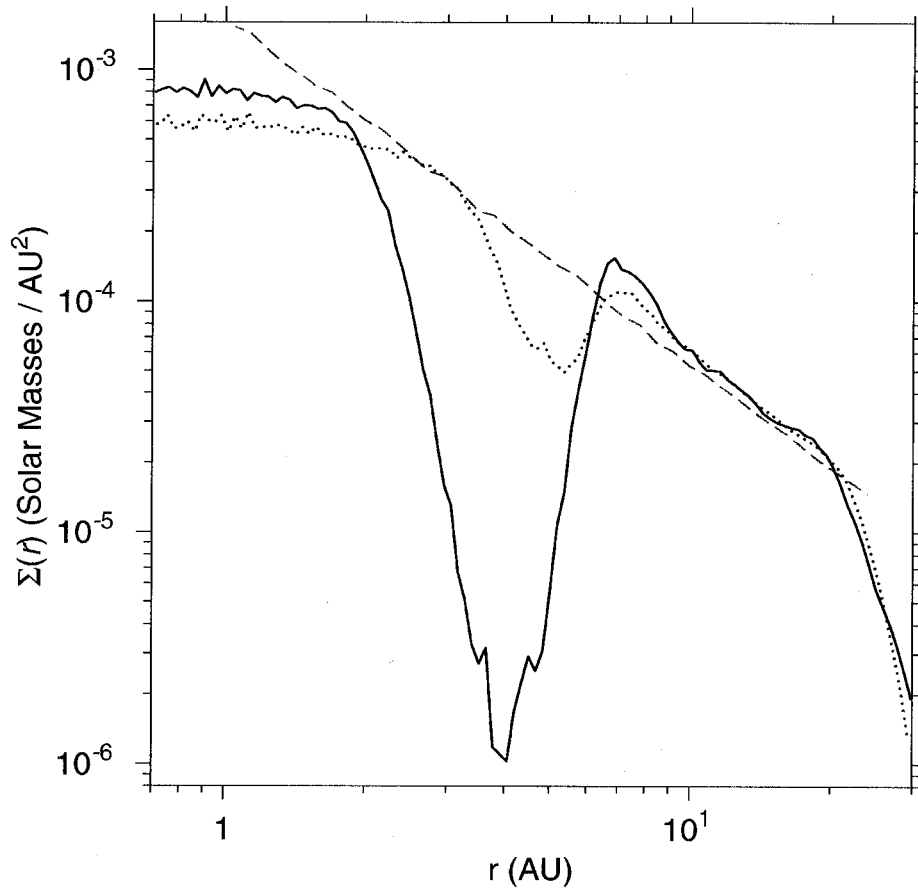


Figure 4.8: Azimuthally and vertically averaged surface density of two discs with embedded Jupiter-mass planets, after 326 years. The solid line is the density of a $0.1 M_{\odot}$ disc. A deep gap has formed within 100 years, and Type I migration has stopped. The dotted line is the density (multiplied by 10) of a $0.01 M_{\odot}$ disc. Note that a depression has formed about the planet, of less than half the initial density. This feature can be called a gap, but the planet is still exhibiting Type I migration. The dashed line shows the initial density profile.

the disc stability. We have shown the orientation in parameter space of four broad categories of interaction. These interactions are: Type I migration; gap formation and Type II migration; planet-triggered instability; and unstable discs. The stability of the disc is the most effective predictor of the type of interaction between a gaseous disc and an embedded planet.

Planet formation and migration is a non-linear process that requires the reasoned application of computational resources to model. Future investigations will explore the details of each interaction we have described. In addition, we will refine our knowledge of the boundaries between regions of parameter space. Future observations will give us a range for Q and a better understanding of the temperature profile in protoplanetary discs. Combined with the results presented here, we can say which migration and formation processes will be relevant.

Chapter 5

MORE TESTS OF MIGRATION

In this chapter we present the results of a suite of simulations of planetary migration. These simulations take a disk model with an embedded planet as described in Section 3.3.1 and evolve the system for several dynamical times. Given the simulation outputs we calculate quantities like the migration and accretion rates of the planet and explore how these vary with the parameters of the disk, planet and simulation.

Our standard case is a $1 M_{\odot}$ star with $0.01 M_{\odot}$ circumstellar disk initially extending from 1 to 25 AU. Embedded in the disk is a $1 M_{\text{Jup}}$ planet initially on a circular orbit at 5.2 AU (the current semi-major axis of Jupiter in our Solar System). The disk–planet system is evolved for 326 years. A suite of simulations was built by varying the physical parameters in the initial conditions. In addition, we investigated the effects due to some computational parameters. The following sections detail the performance, analysis and results of this suite.

5.1 *Performing and Analyzing*

Running the Simulations All the simulations described in this chapter were run using *Gasoline* in serial mode on computers in the Astronomy Department of the University of Washington. The jobs were distributed over a group of ~ 70 PCs running Linux by the Condor system (Thain et al., 2004). Jobs were run in Condor’s *vanilla* universe using *Gasoline*’s native checkpointing to perform restarts.

System of Units The system of units used was Astronomical Units for length, Solar Masses for mass and years divided by 2π for time. In this system, the largest

timestep was $\delta_0 = 16$, about 2.5 years. *Gasoline* uses a multi-stepping scheme to speed up the force calculations for particles with varying dynamical times. Smaller timesteps lie on “rungs”, binary subdivisions of the maximum timestep. The timestep for particles on the i th rung is $\delta_i = \delta_0/2^i$. For each particle, the timestep is chosen from the largest gravitational interaction it participates in (Richardson et al., 2000). In addition, the timestep is required to obey the Courant condition (Wadsley et al., 2004). In our simulations, the majority of the particles were within the first 4–5 rungs. The largest number of rungs used was usually 12, by the innermost particles.

Equation of State Except for Section 5.3.4, the equation of state used was isothermal with imposed radial temperature profile of $\eta = 0.05$ (see Section 3.1.2) and mean molecular weight of the gas $\mu = 2 m_{\text{H}}$. This set the temperature such that $T(r = 1 \text{ AU}) = 538 \text{ K}$ and $T(r = 5.2 \text{ AU}) = 103 \text{ K}$.

Initial Conditions Initial conditions for the disk were generated as described in Section 3.3.1. With those temperature and density profiles and standard disk mass $M_D = 0.01 M_{\odot}$, the minimum value of the Toomre stability criterion is at the outer edge of the disk, $Q = 16$. No boundary conditions were imposed, allowing the disk to expand and contract. Without an embedded planet, the disk exhibited little structure formation. During a brief (about 20 years) ring-down period, low-amplitude, many-armed spiral waves equilibrated the disk. A planet particle interacting via gravity only was placed on a circular orbit at 5.2 AU. The motion of the planet particle was not constrained by any external forces. Its motion was determined entirely by the gravitational forces due to the central star and the gas disk. The central star was always $1 M_{\odot}$.

Planet Formation In Chapter 4 we considered the formation of giant planets via the disk instability. In this chapter, we are assuming that a planet has already formed

on a circular orbit in an unperturbed disk. This is more consistent with the core accretion model of planet formation. Specifically, we are trying to start at the point where gas accretion becomes a runaway process. This is the time when the planet first starts to significantly perturb the gas disk.

5.1.1 Calculation of Accretion and Migration Rates

To extract migration and accretion rates from our simulations, we calculate the semi-major axis and mass of the planet for every simulation output. Using the two-body approximation, the semi-major axis of a planet with mass M_p , instantaneous velocity v_p and radial position r_p from a central star with mass M_* is

$$a_p = \left(\frac{2}{r_p} - \frac{v_p^2}{G(M_* + M_p)} \right)^{-1} \quad (5.1)$$

The calculation of the mass of the planet is detailed in Section 5.4.2.

The simulation outputs are regularly spaced in time, typically 2.55 yr apart. Whenever the semi-major axis and mass of the planet appear to vary linearly with time, the values are fit to a straight line using a least-squares fitting routine. The slopes of the best-fit lines are then quoted as the rates for migration and accretion for that simulation. Because we do not have uncertainties for each data point, the concept of goodness-of-fit does not apply. We examine each straight-line fit to ensure that the data does in fact appear to be linear.

5.2 Dependence on Planet and Disk Mass

The theory of Type I migration, discussed in Section 1.4.1, gives an expression for the migration rate of a planet embedded in a gas disk. This rate is linearly dependent on the mass of both the planet and disk. We performed a suite of 212 simulations to test the predicted dependence.

In this suite, the total mass of the disk and initial mass of the planet were varied from 0.0025–0.09 M_\odot and 0.25–2 M_{Jup} , respectively. The softening lengths were deter-

mined with the default parameters described in Section 5.3.2. The artificial viscosity parameters were fixed at their default values. The number of particles used ranged from 20000–800000.

5.2.1 Overall Results

For the standard case, $M_D = 0.01 M_\odot$ and $M_p = 1 M_{\text{Jup}}$, the planet migrates inward at a constant rate of 10^{-3} AU/yr. It also accretes gas from the surrounding disk at a constant rate of $2.5 \times 10^{-6} M_\odot/\text{yr}$. The quoted rates are the mean values from 103 different simulations with the specified disk and planet masses. The standard deviation from the mean of the migration rate is 1.2×10^{-4} , about 12 percent. The standard deviation from the mean of the accretion rate is 1.4×10^{-7} , about 6 percent. Reasons why simulations with identical parameters yield different results are discussed in Section 5.3.1.

The migration and accretion continue at these rates for several hundred years (tens of orbits). The results presented in this section are all derived from this initial period. Later, the migration slows as the planet creates a gap in the disk. Section 5.5 discusses the long-term behavior. For some of the simulations with more massive disks the timescale for gap formation is short. In those cases, the quoted migration and accretion rates were derived from only the first few orbits of the planet.

5.2.2 Dependence on Planet Mass

We found that migration rate was independent of planet mass. Figure 5.1 shows the migration rate as a function of the initial planet mass for 137 simulations with $M_D = 0.01 M_\odot$. No trend is evident. The rates shown are a superset of the standard case result, yet the mean and standard deviation of the larger set are nearly identical. To quantify the lack of trend, we need to estimate the errors of a linear fit to this data. Since we have no *a priori* knowledge of the magnitude of the errors, we use the Bootstrap method, assuming our data is independent and identically distributed

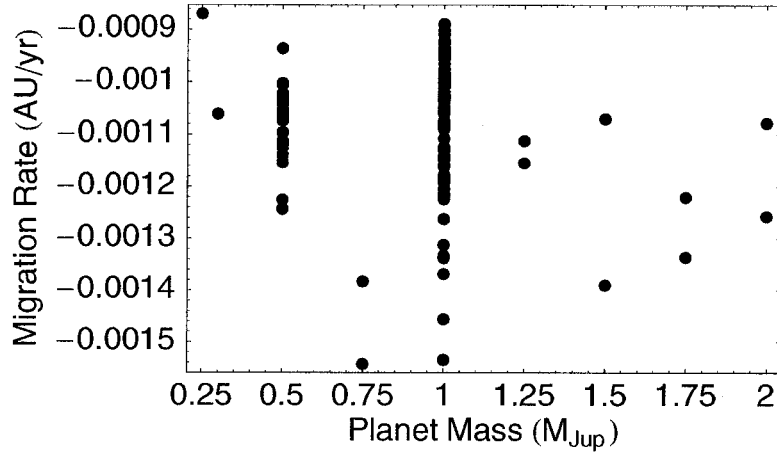


Figure 5.1: The migration rate as a function of the planet mass in a $0.01 M_{\odot}$ disk. Varying the initial mass of the planet does not affect the rate of migration.

(Press et al., 1992). For the data shown in Figure 5.1, the linear fit with errors is $\dot{a}_p = ((-1.02 \pm 0.03) - (6.3 \pm 3.7) \times 10^{-2} M_p/M_{\text{Jup}}) \times 10^{-3}$ AU/yr. The intercept is well constrained and definitely non-zero, while the slope is poorly known and much smaller. Furthermore, the slope is within two standard deviations of zero. This shows quantitatively the absence of a linear trend, as predicted by the linear theory. In our simulations, within the range $0.25 M_{\text{Jup}} < M_p < 2 M_{\text{Jup}}$, the rate of migration is unrelated to the initial mass of the planet.

Nelson and Benz (2003a) (hereafter, NB) performed similar simulations using a two-dimensional grid code. After performing a suite of simulations with $M_D = 0.05 M_{\odot}$ and planet mass ranging from 0.1 – $2 M_{\text{Jup}}$, they also concluded that migration rate was independent of planet mass. Figure 5.2 shows the results of similar set of simulations that we performed. We made bootstrap estimates of the errors of a linear fit to this data, as above. Again we find a definitely non-zero intercept and small slope, supporting our claim of independence. Our simulations show a smaller

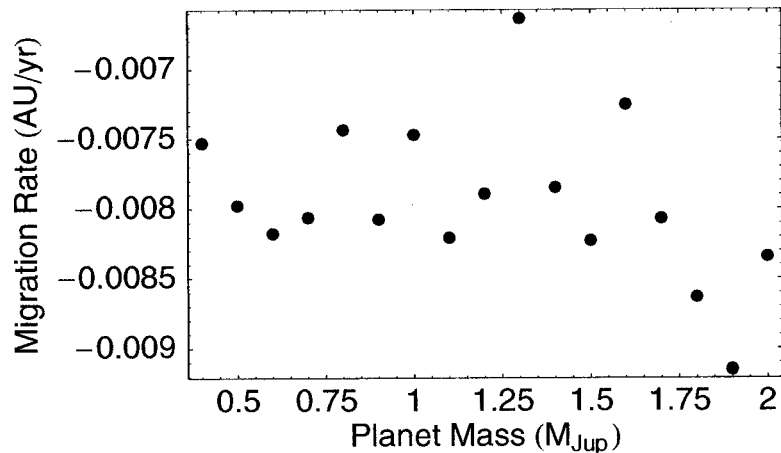


Figure 5.2: The migration rate as a function of the planet mass in a $0.05 M_{\odot}$ disk. Compare this to Figure 9 of NB. We agree on the lack of trend, but find a magnitude several times greater. These simulations used $N = 80000$ particles.

spread in migration rate than those of NB, but a magnitude several times larger. This difference is likely due to our differing numerical approaches. They used a two-dimensional Eulerian grid; we used a three-dimensional SPH simulation.

Why does the migration rate not depend on the mass of the planet? We believe this is because the disk does not respond linearly to the presence of the planet, as required by the theory of Type I migration. We make this claim based on three measurements of our simulations.

First, the magnitude of the perturbed density in the spiral waves formed by the planet is not small. The linear theory deals with the perturbed surface density of the disk, assumed to be small with respect to the unperturbed, average density (Goldreich and Tremaine, 1978a). This is not true in our simulations. We compressed the disk vertically to obtain a surface density. We then measured the maximum deviation in the surface density relative to the azimuthal average at each radius, $\delta\Sigma/\Sigma$. Close

to the planet, the relative deviation in surface density was typically 3 to 5. Further away, near the Lindblad resonances, the deviation was routinely above 1. These large density fluctuations clearly do not satisfy the small perturbation required by the theory.

Second, the maximum density just detailed did not depend on the perturbing planet mass. In the linear regime, we would expect the amplitude of the spiral waves to be dependent on mass of the planet exciting them.

Finally, the relative surface density was decomposed into azimuthal Fourier modes. According to theory, the magnitude of the torque exerted at the m th Lindblad resonances increases with m up to about $m = 10$ (Ward, 1997). Therefore, the high m modes are most responsible for migrating the planet. We measured the power in the m th mode at the m th Lindblad resonance. It was independent of planet mass. NB performed a similar calculation with the same result.

Based on this evidence, we conclude that, for planet masses of 0.25–2 M_{Jup} , the response of the disk is nonlinear in proportion to the perturbing potential of the planet. Therefore, we should not expect the linear theory to correctly predict the rate of migration. Beyond a critical planet mass, the response of the disk saturates. That is, the spiral waves cannot be made sharper or higher in amplitude. Therefore the torque they exert does not increase as the planet mass increases. Presumably, probing ever-lighter planets would reveal the the minimum planet mass that saturates the disk response. Simulations of smaller-mass planets require more resolution in the disk, so we have been unable to look for this transition.

Unlike migration, we found that the initial planet mass does affect the rate of accretion. Figure 5.3, the counterpart to Figure 5.1, shows the accretion rate as a function of the initial planet mass for 137 simulations with $M_D = 0.01 M_\odot$. Figure 5.4 shows the similar result for the suite similar to NB. The accretion rate is linearly dependent on the initial planet mass. This agrees with our explanation of accretion via gas capture within the Hill sphere (Section 5.3.2). Because the volume of the Hill

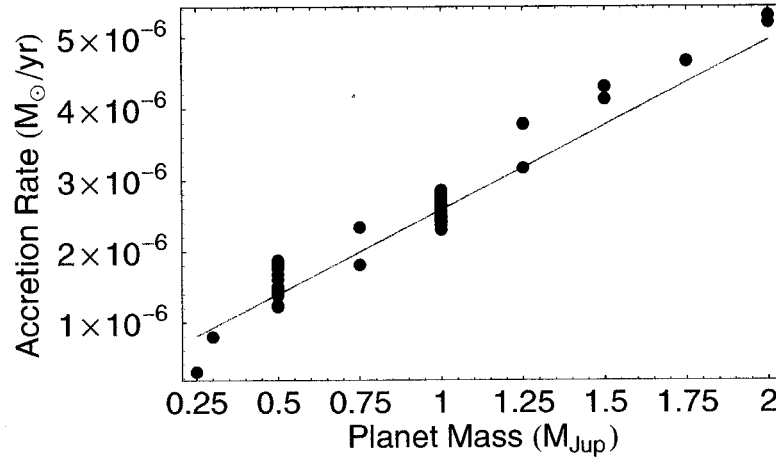


Figure 5.3: The accretion rate as a function of the planet mass in a $0.01 M_{\odot}$ disk. The data is well approximated by a linear function of the planet mass.

sphere is proportional to the planet mass, so is the gas available for accretion.

5.2.3 Dependence on Disk Mass

We found that migration rate was linearly dependent on the total disk mass (at fixed size and profile, equivalently the surface density). This agrees with the prediction of the theory of Type I migration. Figure 5.5 shows the results of 118 simulations with $M_p = 1 M_{\text{Jup}}$ and disk masses ranging from 0.01 – $0.09 M_{\odot}$.

NB also performed simulations varying the disk mass from 0.0025 – $0.05 M_{\odot}$, using a $0.3 M_{\text{Jup}}$ planet. We performed simulations for those conditions, using a disk of 80000 particles, obtaining the results shown in Figure 5.6. As in the simulations where the planet mass was varied, our rates are several times greater than NB. Notice that for disk masses below $0.04 M_{\odot}$ the migration rates are linearly dependent on the disk mass. This trend is slightly stronger than that found by NB. Our result agrees qualitatively with the results of the Type I migration theory (Section 1.4.1).

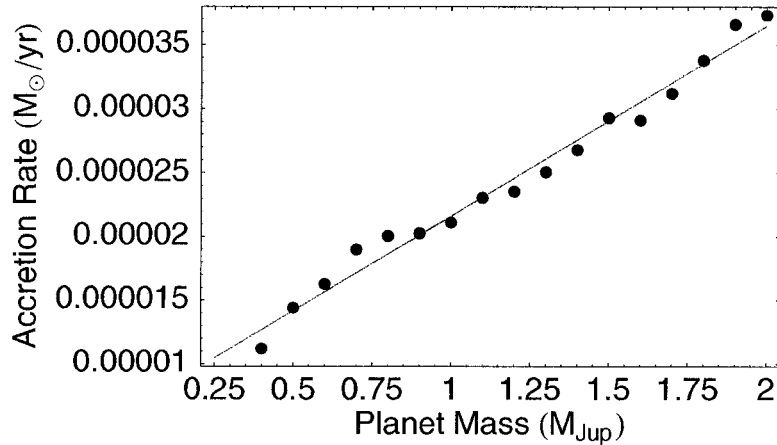


Figure 5.4: The accretion rate as a function of the planet mass in a $0.05 M_{\odot}$ disk. The data is well approximated by a linear function of the planet mass.

Quantitatively, we are within a factor of a few of Equation 1.2. However, since we do not see the linear dependence on planet mass, this is likely coincidence.

The linear fits shown in Figures 5.5 and 5.6 were made by minimizing the χ^2 assuming identical errors. By creating bootstrap datasets, we estimate the error in the constant term to be 11% and 20%, and the error in the slope to be 4% and 2%, for Figures 5.5 and 5.6, respectively. Within this error, the constant term is definitely non-zero. This implies that, for zero disk mass, the planet still migrates. This could be due to numerical effects inherent in the simulation. Alternatively, the interaction with the disk could deviate from linearity at disk masses lower than we simulated. Note that at the lowest disk masses, the disk is only a few times more massive than the planet.

Our quoted migration rates imply that giant planets should migrate rapidly and be accreted by their parent star within only a few thousand years. However, as discussed in Section 5.5, larger disk mass results in more rapid gap formation, halting

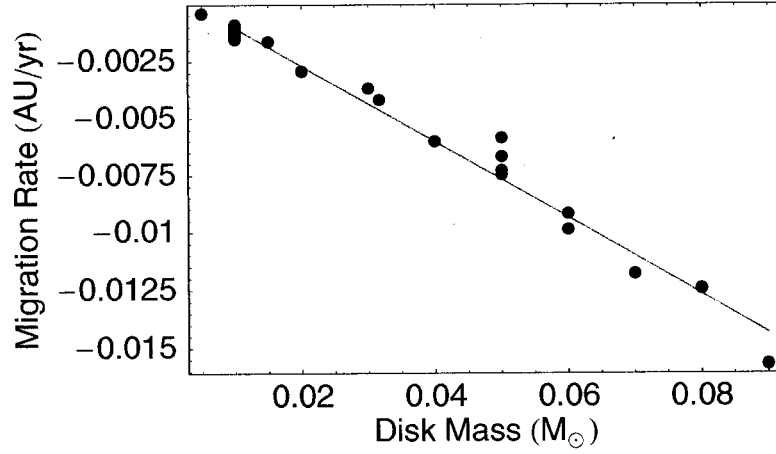


Figure 5.5: The migration rate of a $1 M_{\text{Jup}}$ planet as a function of the disk mass. The data is well approximated by a linear function of the disk mass: $\dot{a}_p = (0.0006 - 0.165 M_D/M_{\odot}) \text{ AU/yr}$.

migration sooner. Therefore, we believe that some planets can survive this period of rapid migration, provided they open a gap quickly.

For disk masses above $0.04 M_{\odot}$ the migration rate appears to plateau. The cause of this is unclear. The accretion history for these simulations is very different than for lower-mass disks. We can understand the behavior of the accretion by considering the effect of fixed gravitational softening as the simulation proceeds. Section 5.3.2 describes the mechanics of accretion in the simulation and its dependence of the gravitational softening length. To accrete, the softening length between planet and gas particles must be a fraction of the Hill radius (Equation 5.3). The softening length is fixed for the duration of the simulation. However, as the planet migrates inward, the Hill sphere gets smaller. As the planet accretes, the Hill sphere grows, but to a lesser degree. Thus, if the planet migrates too quickly, the Hill radius and softening lengths may become commensurate, halting accretion. Figure 5.7 shows this process

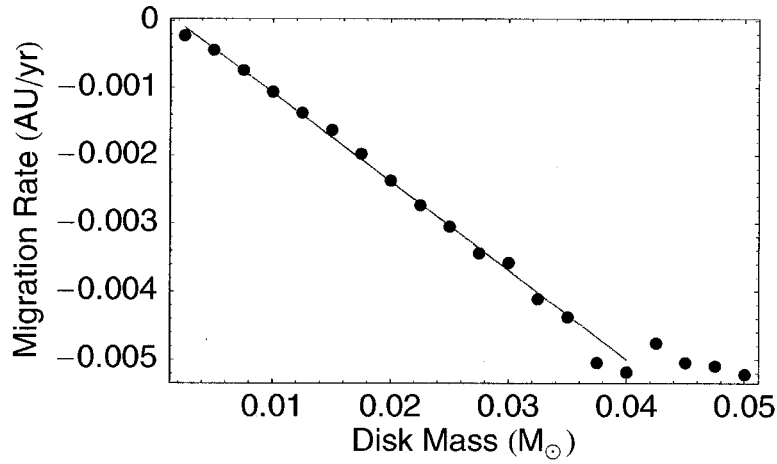


Figure 5.6: The migration rate of a $0.3 M_{\text{Jup}}$ planet as a function of the disk mass. Below $M_D = 0.04 M_{\odot}$, the data is well approximated by a linear function of the disk mass: $\dot{a}_p = (0.00023 - 0.130 M_D/M_{\odot}) \text{ AU/yr}$. Compare this to Figure 10 of NB.

occurring in a simulation with $M_D = 0.0475 M_{\odot}$. Given the unphysical accretion processes, we are wary of results at this resolution for disk masses above $0.04 M_{\odot}$ for $0.3 M_{\text{Jup}}$ planets. As Figure 5.5 shows, we performed higher-resolution simulations of $1 M_{\text{Jup}}$ planets in more massive disks and did not find a similar migration rate plateau. We therefore conclude that the data points above $M_D = 0.04 M_{\odot}$ in Figure 5.6 are numerical artifacts.

We expect the accretion rate to be linearly dependent on the disk mass. Figures 5.8 and 5.9 show the accretion rate of 1 and $0.3 M_{\text{Jup}}$ planets, respectively. As discussed above, the accretion rates for the $0.3 M_{\text{Jup}}$ planet in disks more massive than $0.04 M_{\odot}$ are the product of a numerical artifact.

5.3 Dependence on Other Parameters

Gasoline is a complex program that parametrizes many of the numerical issues present

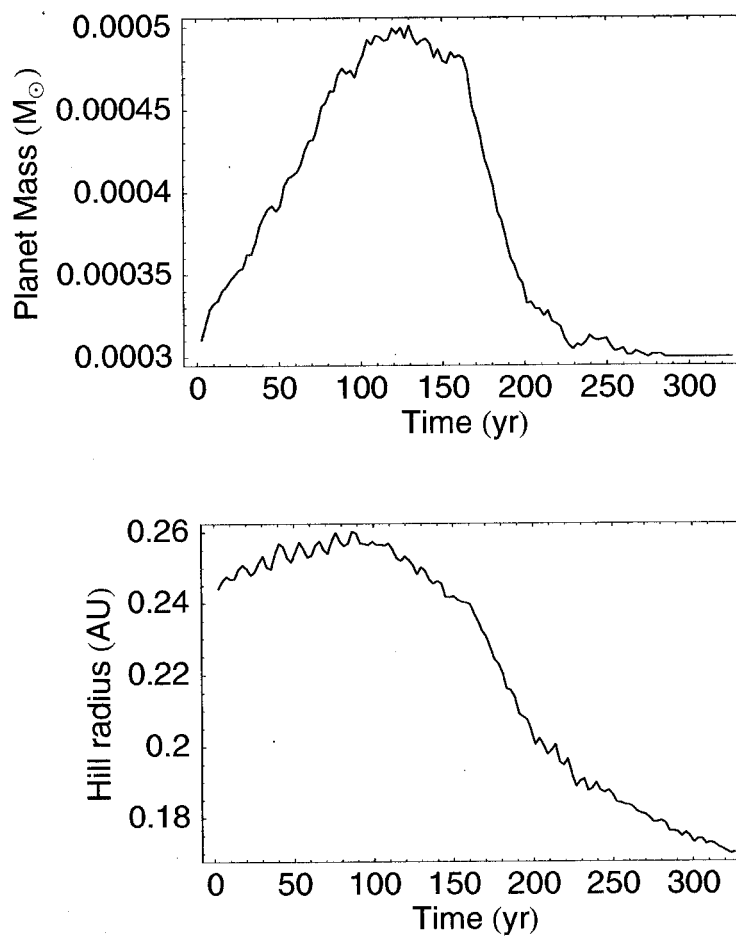


Figure 5.7: Mass and Hill radius of the planet as a function of time for a $1 M_{\text{Jup}}$ planet in a $0.0475 M_{\odot}$ disk. As the planet migrates inward, the Hill radius does not grow fast enough. Accretion halts and the planet's envelope of gas particles is lost, further shrinking the Hill radius.

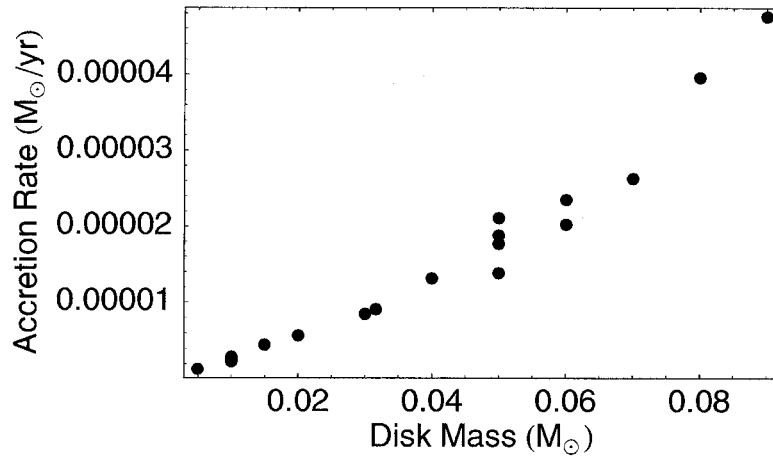


Figure 5.8: The accretion rate of a $1 M_{\text{Jup}}$ planet as a function of the disk mass.

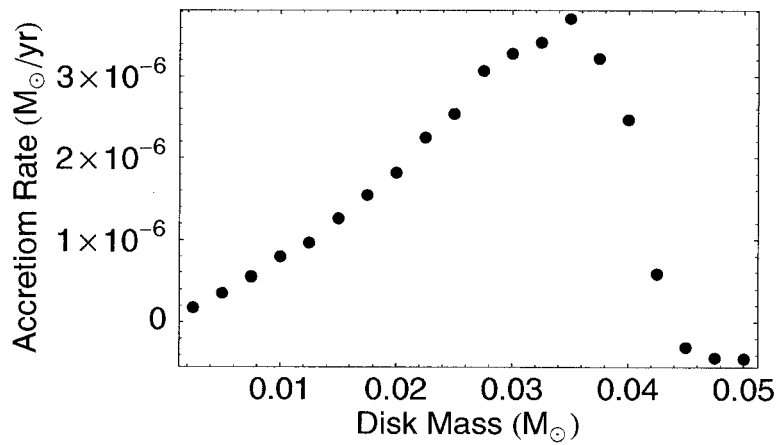


Figure 5.9: The accretion rate of a $0.3 M_{\text{Jup}}$ planet as a function of the disk mass.

in a simulation. Here we investigate the effects due to varying some computational parameters. We explain how simulations with identical parameters can produce different results.

5.3.1 *Dependence of Migration Rate on Simulation Resolution*

We hope that our simulations have accurately captured the relevant physics of the disk–planet system. We test this by varying the simulation resolution. To measure the convergence with resolution, we conducted simulations of the standard migration system with particle numbers ranging from 2×10^4 to 8×10^5 . At each resolution we run several simulations, varying the seed used by the random number generator in constructing the initial conditions. For a good random number generator, each choice for the seed is equally valid. The discretization of the continuous fluid introduces some small amount of Poisson noise onto the particle distribution. By varying the random seed, we quantify the effect this discretization noise has on the aggregate results we are interested in. Figures 5.10 and 5.11 show the dependence of the migration and accretion rates on the resolution for our standard disk and planet masses. In this instance the error bars are calculated from the standard deviation of the rates for each population of simulations at a particular resolution. By measuring the variance in this way, we have a baseline with which to judge the effects of other parameters. For example, when we say that the gravitational softening does not affect the migration rate, we mean that the migration rates measured in runs with different softening lengths were within the standard deviation for the resolution of the simulations.

The random seed effect is an example of how two simulations with identical physical parameters can have different numerical realizations. Can two numerically identical simulations yield differing results? In the case of *Gasoline*, there are two computational mechanisms that can lead to this. First, when a parallel version of *Gasoline* is used, a dynamic load-balancing algorithm is used to distribute work between processors. If conditions vary between runs, for example the number of processors or

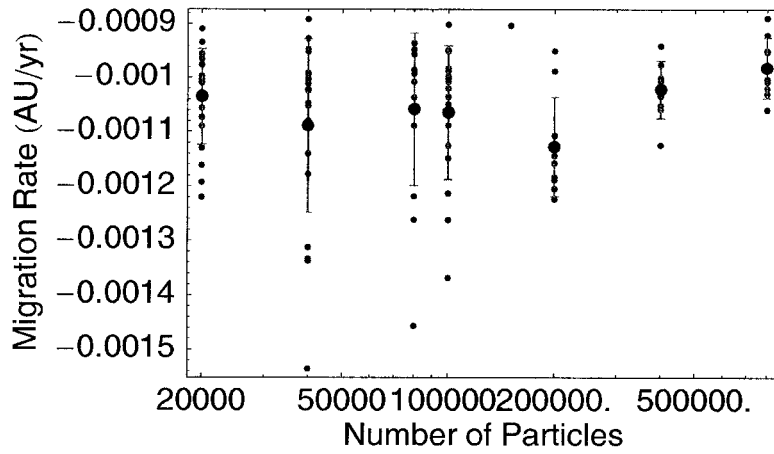


Figure 5.10: Migration rate of a $1 M_{\text{Jup}}$ planet in a $0.01 M_{\odot}$ disk as a function of the simulation resolution. Mean values for a particular number of particles are shown in blue, and the error bar represents one standard deviation of the population. Increasing resolution decreases the spread in migration rates, and the average value appears to be fixed. The independence of average migration rate indicates that we have sufficient resolution to capture the formation and dissipation of the spiral waves excited by the planet.

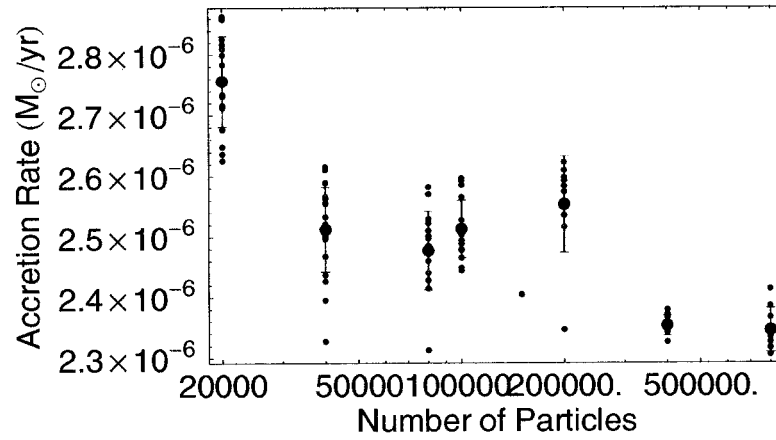


Figure 5.11: Accretion rate of a $1 M_{\text{Jup}}$ planet in a $0.01 M_{\odot}$ disk as a function of the simulation resolution. Mean values for a particular number of particles are shown in blue, and the error bar represents one standard deviation of the population. Excepting a hiccup at 200000 particles, the deviation from the mean decreases with increasing resolution. In addition, the mean value fluctuates. We suggest that this dependence on resolution is due to a finer sampling of the region within the Hill radius of the planet, where gas particles can be captured. In addition, the extent of dissipation via artificial viscosity decreases with resolution.

network latency, the load-balancer can choose a different distribution of work, leading to slightly different force calculations. This did not occur in the simulations described in this chapter, as they were all run in serial. Second, certain parameters can change when restarting a run from a checkpoint. A checkpoint is a picture of the simulation program's state that is periodically written to disk. When a job is interrupted, it resumes sometime later by restoring state using the checkpoint data. *Gasoline* has a different file format for simulation snapshots and checkpoints. Due to a computational difficulty (Wadsley et al., 2004, see Section 3.1.1 of), the change in smoothing length of each particle is limited between timesteps. When restarting from a checkpoint, the growth limiter is relaxed. Thus, the smoothing of length of a particle can change during a restart. Due to the nature of the *Condor* system used to perform the jobs, the number of restarts during a simulation run can vary enormously, from none to one restart every output. By performing multiple runs of numerically identical disks, we believe that the magnitude of this effect is comparable to that due to choosing the random seed.

5.3.2 Varying Gravitational Softening

Newton's Law of Gravity states that the gravitational force between two point masses is inversely proportional to the square of the distance between them. Thus, when two particles have a close approach, the gravitational force between the two can grow arbitrarily large. Real astrophysical objects are not point masses and thus avoid this difficulty. Although we usually think of the particles in the simulation as point masses, we must modify this idea to correctly handle close approaches. This is done by "softening" the gravitational force: decreasing the strength of gravity for short-range interactions.

A common softening prescription is cubic-spline softening. In this method the gravitational force is equal to the Newtonian value for interaction distances greater than twice the softening length ϵ . Inside the softening length the force is that due to a

spherically symmetric extended mass with mass distribution equal to the cubic-spline smoothing kernel (Equation 2.3). The softening length for a pairwise interaction is the average of the softening lengths of the two interacting particles. This is the method of softening used in all our simulations.

In our simulations all gas particles have the same softening lengths. The planet particle is more massive than the gas particles but, we imagine, has a more compact physical size, so is given a different softening length. In addition, the potential of the central star is softened on a third distinct length scale. To calculate the gravitational force between any pair of particles, the *mutual softening length* is used. The mutual softening length is the arithmetic average of the individual softening lengths of the particles.

Unlike the smoothing length used to calculate gas pressure forces, the softening length does not vary with time. How then do we choose appropriate values for the softening lengths? The purpose for which we introduced softening is to reduce two-body encounters and account for the extended physical size of the particles. Too small a softening clearly misses this goal and is more computationally expensive. Too large a softening is also incorrect, obscuring small-scale interactions that we have sufficient resolution to correctly resolve. In a study of Jeans collapse, Bate and Burkert (1997) found that softening and smoothing should be commensurate in SPH simulations. Dehnen (2001) suggests picking a softening length by minimizing the error in the gravitational force calculation. For unstable disk simulations, Mayer et al. (2003) empirically found that the softening should be smaller than the most unstable Toomre wavelength (Binney and Tremaine, 1987). Here we use an empirical study to choose softening lengths by looking for accretion onto the planet.

We want the procedure used to pick softening lengths to scale with the physical and computational parameters of the system. For the gas particles the procedure should scale with the total disk mass and the number of particles used in the simulation. For a disk of mass M_D composed of N equal-mass particles, we use a baseline density ρ_{gas}

to set the softening length:

$$\epsilon_{\text{gas}} = \left(\frac{M_D/N}{\frac{4}{3}\pi\rho_{\text{gas}}} \right)^{1/3} \quad (5.2)$$

For the planet particle, the natural length scale is the *Hill radius*, derived from Hill's equations concerning motion in the restricted three-body problem.

$$r_H = r_p \left(\frac{M_p}{3M_\star} \right)^{1/3} \quad (5.3)$$

where r_p is the distance from the central star to the planet. This is the radius of the *Hill sphere* of a planet. Inside the Hill sphere, the gravitational field of the planet dominates that of the central star. See Murray and Dermott (1999) for a derivation of Hill's equations.

The results of our simulations indicate that varying the gravitational softening length of either the gas particles or of the planet has no measurable affect on the migration rate of the planet. However, varying the softening strongly affects the accretion rate. Large softening prohibits the planet from capturing surrounding gas particles. Thus we can use the presence of accretion to choose an appropriate softening length. By examining the process of accretion (see Section 5.4.1 for a physical description), we see that the mutual softening lengths should be a fraction of the Hill radius of the planet. For the gas particles, we will find a density, and for the planet particle, a fraction of the Hill radius, such that the mutual softening between planet and gas particles satisfies this criterion. By varying the softening length of the gas particles, Figure 5.12, and planet particle, Figure 5.13, we see that too large a softening leads to a sharp cutoff in accretion. Smaller softening is more computationally expensive as it requires more force calculations per particle. The accretion rate does not vary much for softening lengths below the cutoff value. Therefore, we choose softening lengths for the gas and planet particles that are close to the cutoff. The softening length of the gas particles is set using Equation 5.2 with $\rho_{\text{gas}} = 3.73 \times 10^{-5} M_\odot \text{ AU}^{-3}$. The softening length of the planet particle is set to $r_H/5$. These two choices ensure

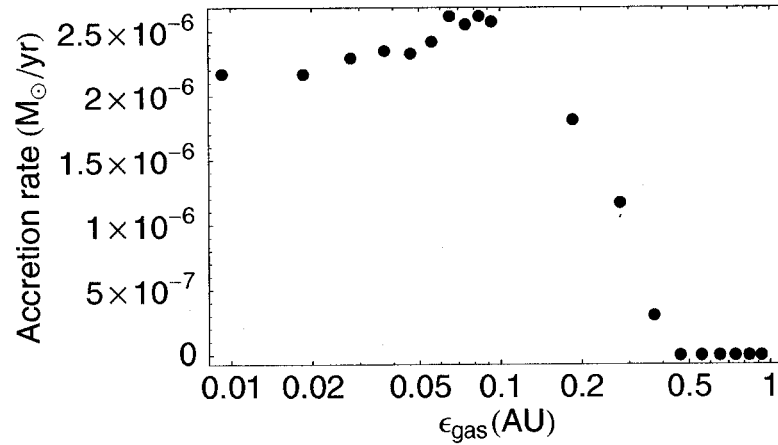


Figure 5.12: The accretion rate onto the planet as a function of the gravitational softening of the gas particles. These data are taken from simulations with $M_D = 0.01 M_{\odot}$, $N = 80000$ and $M_p = 1 M_{\text{Jup}}$. At this resolution the choice $\rho_{\text{gas}} = 3.73 \times 10^{-5} M_{\odot} \text{ AU}^{-3}$ corresponds to $\epsilon_{\text{gas}} = 0.093 \text{ AU}$, close to the transition value.

that, at sufficient resolution (number of gas particles), the mutual softening is small enough to allow for accretion onto the planet. That the migration rate of the planet is independent of the gravitational softening indicates that the internal torques between the planet particles, both gas and the gravity-only core, are not the source of the observed orbital migration.

The potential of the central star is softened with a length scale $\epsilon_{\odot} = 0.4 \text{ AU}$. This is within the internal edge of the disk in all our simulations. In addition, it is well within the inner Lindblad resonance of a planet at 5.2 AU , so should not affect the formation and dissipation of spiral density waves.

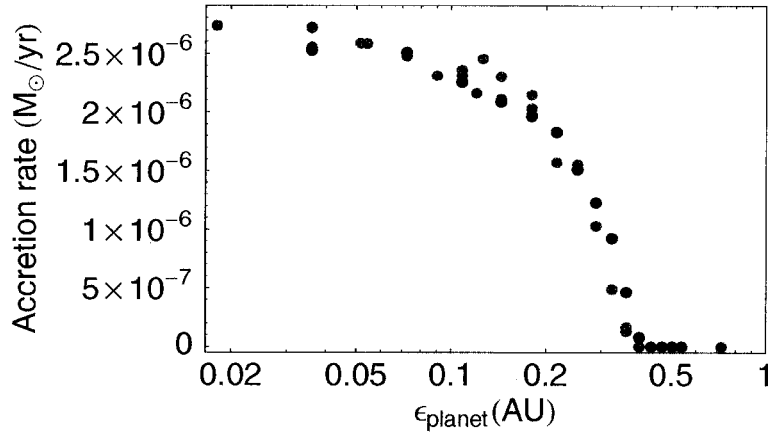


Figure 5.13: The accretion rate onto the planet as a function of the gravitational softening length of the planet. These data are taken from simulations with $M_D = 0.01 M_{\odot}$ and $M_p = 1 M_{\text{Jup}}$. Red datapoints are from simulations with $N = 40000$, blue with $N = 80000$. At this resolution the choice $r_H/5$ corresponds to $\epsilon_{\text{planet}} = 0.072$ AU.

5.3.3 *The Effect of Artificial Viscosity*

The artificial viscosity described in Section 2.3.1 is parametrized with two constants, α and β , designed to handle shocks in gas and reduce particle inter-penetration. Conventional wisdom in the SPH community suggests that $\alpha = 1$, $\beta = 2$ is appropriate for a broad class of simulations. Recently, Mayer et al. (2003) has found that SPH simulations of planet formation via gravitational instability are sensitive to the particular choices for these parameters. We found that varying the artificial viscosity parameters by a factor ten smaller or larger affected the magnitude of the migration rate by only a few percent. When both parameters are set to identically zero, no shocks occur and the planet does not capture surrounding gas particles (there is no accretion). Given this weak dependence, we assert that artificial viscosity is not a dominant force in our simulations. Accordingly, the default values $\alpha = 1$, $\beta = 2$ are used in all other simulations.

5.3.4 *Dependence of Migration Rate on Equation of State*

Simulations of unstable disks revealed that switching from an isothermal to adiabatic equation of state suppressed the formation of clumps (Boss, 2001, 2002; Mayer et al., 2002). Although the disks discussed in this chapter are stable to the gravitational instability, we are still interested in what effect, if any, the choice of equation of state has on the migration and accretion rates. To do this, we ran simulations with an adiabatic equation of state and compared them to our standard isothermal case. The isothermal and adiabatic approximations are extremes. Isothermal assumes that the timescale for radiation of non-equilibrium thermal energy is zero; adiabatic that it is infinite. The true equation of state is likely intermediate. The simulations described below started from the same initial conditions, with $T(r) = T_0(r/r_0)^{-1}$ with $T_0 = 534 K$ and $r_0 = 1 AU$.

Our default equation of state is isothermal with a fixed temperature profile de-

pending only on the cylindrical distance to the central star. Using this relation with a $1 M_{\text{Jup}}$ planet in a $0.01 M_{\odot}$ disk, the disk geometry is stable, and the planet migrates and accretes at a constant rate. Changing to an adiabatic equation of state markedly changed the nature of the simulation. In the adiabatic simulation, particles were allowed to heat via shocks and contraction, and cool during expansion. The region closest to the central star is the most dense, and is strongly shearing. This led to a large influx of heat, heating particles to several hundred-thousand Kelvin. Rapid heating was not limited to the central region, causing the entire disk to puff up, on its way to a spherical equilibrium shape. The planet still excited spiral density waves, but they were much weaker than in the isothermal case. Combined with enhanced gas pressure forces at higher temperature, this prevented gas particles from being captured by the planet. This drastically non-equilibrium behavior indicates that a purely adiabatic equation of state is not appropriate for the system we are trying to model. Especially in the central regions, where we are unsure of the true physical conditions, such rapid heating is clearly a numerical effect.

To try to limit this aspect of the adiabatic equation of state, we performed an adiabatic simulation where the temperature was capped at an arbitrary maximum of 1500 K. Like the fully adiabatic simulation, the disk heated rapidly. The interior region at the maximum temperature grew slowly outward, thickening the disk as it grew.

Migration did occur in both simulations with alternate equations of state, although its nature was different. Figure 5.14 shows the semi-major axis of the planet as a function of time for simulations with imposed isothermal temperature profile, adiabatic and capped adiabatic equations of state. The isothermal simulation yields the familiar constant rate of inward migration. The adiabatic simulation shows the migrate rate quickly decreasing as the disk heats up from the inside outward. The capped adiabatic simulation shows the same trend, with the changeover occurring more slowly. The imposed profile has no vertical structure, while the adiabatic sim-

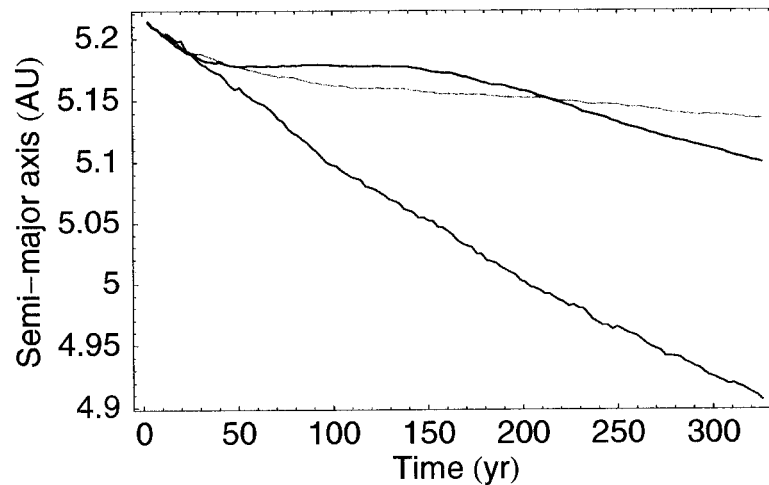


Figure 5.14: Semi-major axis of planets in disks with different equations of state. Black is imposed isothermal profile; red is fully adiabatic; blue is adiabatic capped at 1500 K. Changing the equation of state has a marked effect on the migration and the structure of the disk as a whole.

ulations allow for the temperature to decrease vertically out of the disk. This lets gas pressure forces quickly vertically dissipate the spiral density waves excited by the planet. Migration is thus severely limited, in comparison with the imposed isothermal case.

The result of varying the equation of state is mixed. Clearly it has a large effect on the dynamics of the system. However, it is not clear how to improve on the isothermal model without introducing unphysical numerical effects. Without an appropriate form of additional cooling, an adiabatic equation of state is not appropriate for our simulations of this system. In the future, a more sophisticated treatment of the equation of state and radiative transfer will be necessary to improve the robustness of results of disk–planet interaction.

5.4 Accretion Onto The Planet

A planet can grow by accreting material from the surrounding disk. Here we explain the mechanics of this accretion.

5.4.1 Capturing Gas Particles

In our simulations, the planet captures gas particles from the disk, growing in mass. These particles are gravitationally bound to the planet, forming a flattened sphere of gas rotating in the same sense as the orbital motion (Figure 5.15) A gas particle must come within the Hill sphere of the planet and lose some of its relative velocity to be captured by the planet. This is possible because, in addition to gravity, the gas particles are subject to the dissipative forces of SPH. Figure 5.16 shows a series of zero-velocity curves for the restricted three-body problem appropriate to the Sun-Jupiter combination. The shape of each zero-velocity curve depends on the Jacobi constant (equivalently, the energy in the rotating frame) of a test particle. As the energy decreases, the zero-velocity curve encloses the planet, trapping particles around it. Because SPH is collisional and dissipative, gas particles that lose energy while within the Hill sphere of the planet will become bound to the planet. This occurs when a particle on an orbit slightly external (internal) to the planet is caught by (catches) the trailing (leading) density wave of the planet. The particle collides with the density wave, accelerating (decelerating) and thus, in the rotating frame, losing energy. If the particle is within the Hill radius of the planet it is trapped, becoming part of the envelope. This scenario for the capture of gas particles requires that the gravitational softening between the planet and gas particles be appreciably smaller than the Hill radius, so that the three-body problem approximation is valid. Figure 5.17 highlights the particles that will soon become part of the planet.

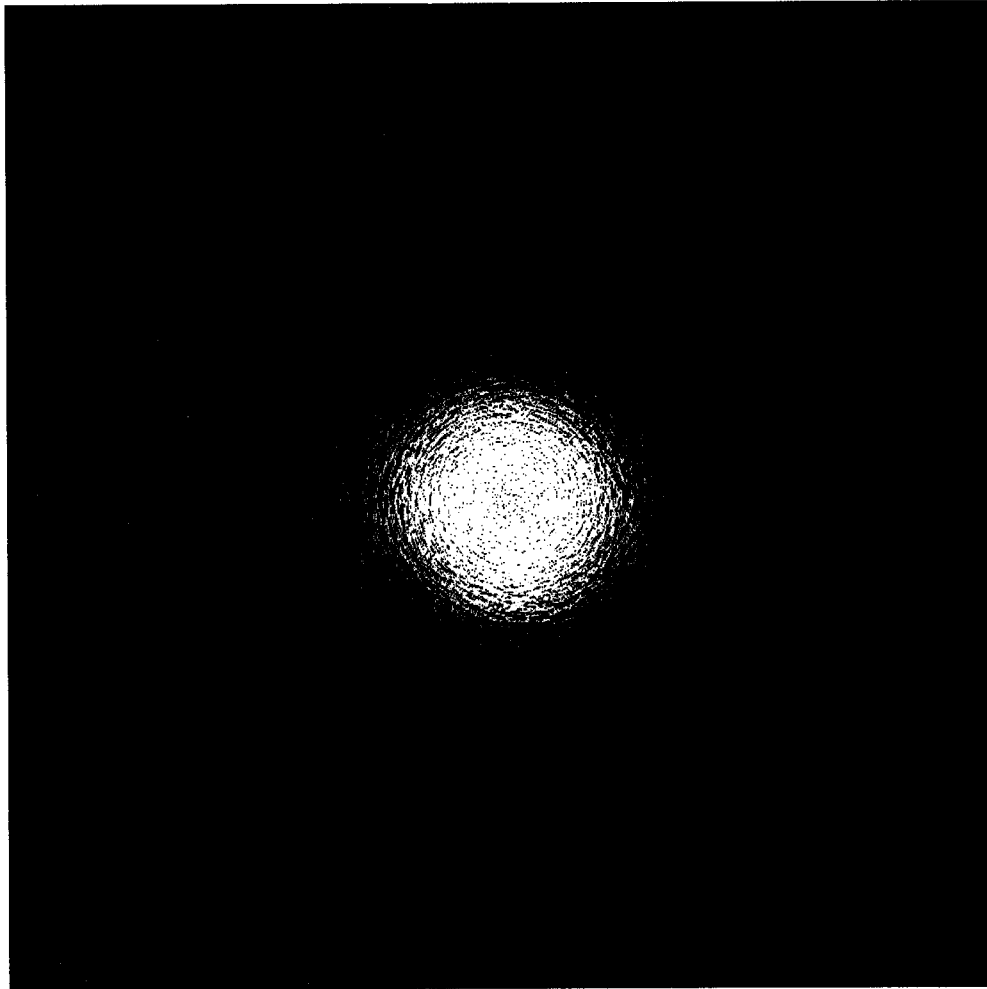
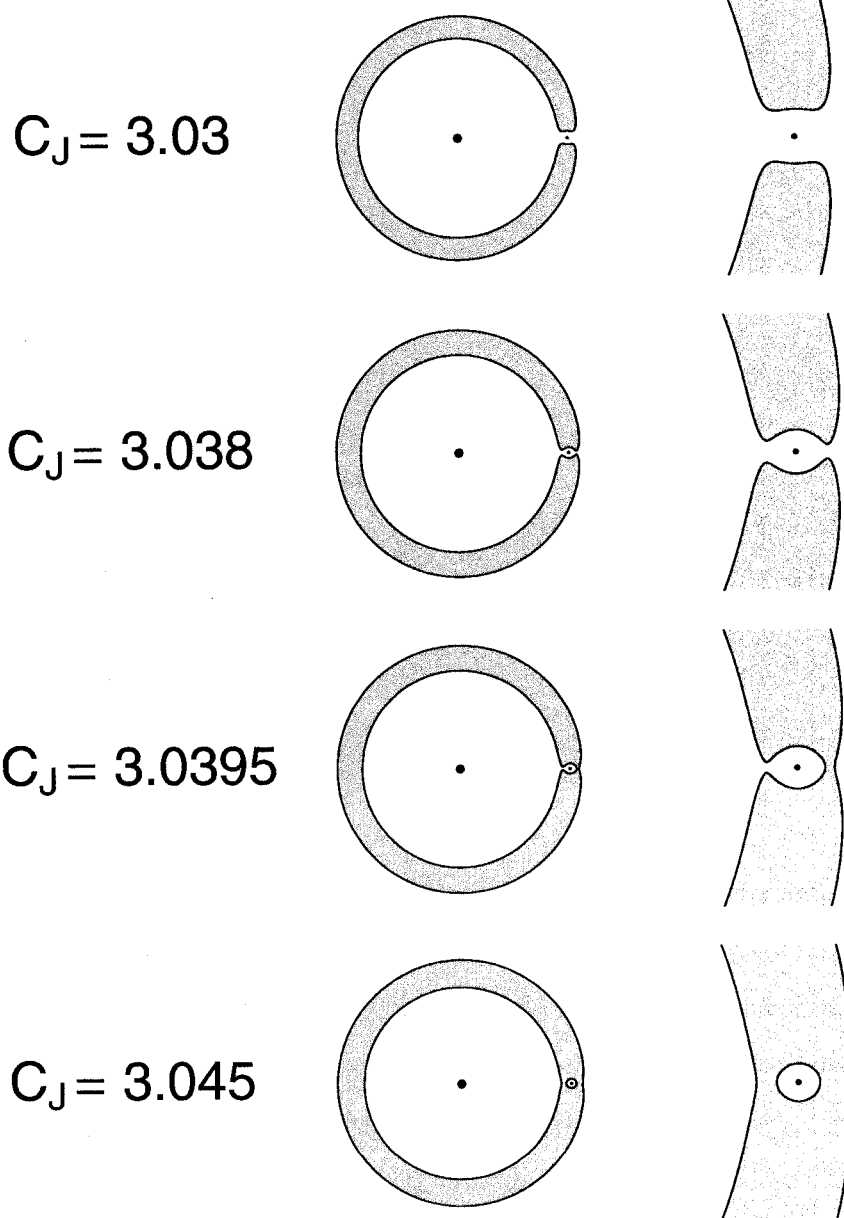


Figure 5.15: Gas particles making up the envelope of a planet in a $0.01 M_{\odot}$ disk. The central star is to the bottom of this image, and the orbital motion is to the left. The disk is composed of 10^6 gas particles. The initial planet particle is $1 M_{\text{Jup}}$. At the time of this snapshot, just a few orbits into the simulation, the planet has accreted $0.07 M_{\text{Jup}}$ of gas particles, as determined by the algorithm described in Section 5.4.2. Vectors on each particle indicate the direction of motion, minus the Keplerian component, around the center of the planet with the same sense as the orbital motion. The length of each vector represents the distance the particle would travel in the next 0.008 yr. The color scale represents the logarithm of the gas density.

Figure 5.16: Zero-velocity curves in the restricted three-body problem with mass ratio appropriate for the Sun–Jupiter system. The right-hand figures are closeups of the area around the planet. A particle with the specified value of the Jacobi constant C_J is prohibited from entering the shaded region. In this system of units $C_J = (x^2 + y^2) + 2 \left(\frac{1-\mu_2}{\sqrt{(x+\mu_2)^2+y^2}} + \frac{\mu_2}{\sqrt{(x-(1-\mu_2))^2+y^2}} \right) - (\dot{x}^2 + \dot{y}^2)$ where $\mu_2 = 0.001$ is the Sun–Jupiter mass ratio. As the Jacobi constant increases, the prohibited region encloses the planet. If dissipative processes decrease the energy (equivalently, increase the Jacobi constant) of a particle while it is near the planet, the zero-velocity boundary closes in, trapping the particle. It is then effectively a part of the planet.



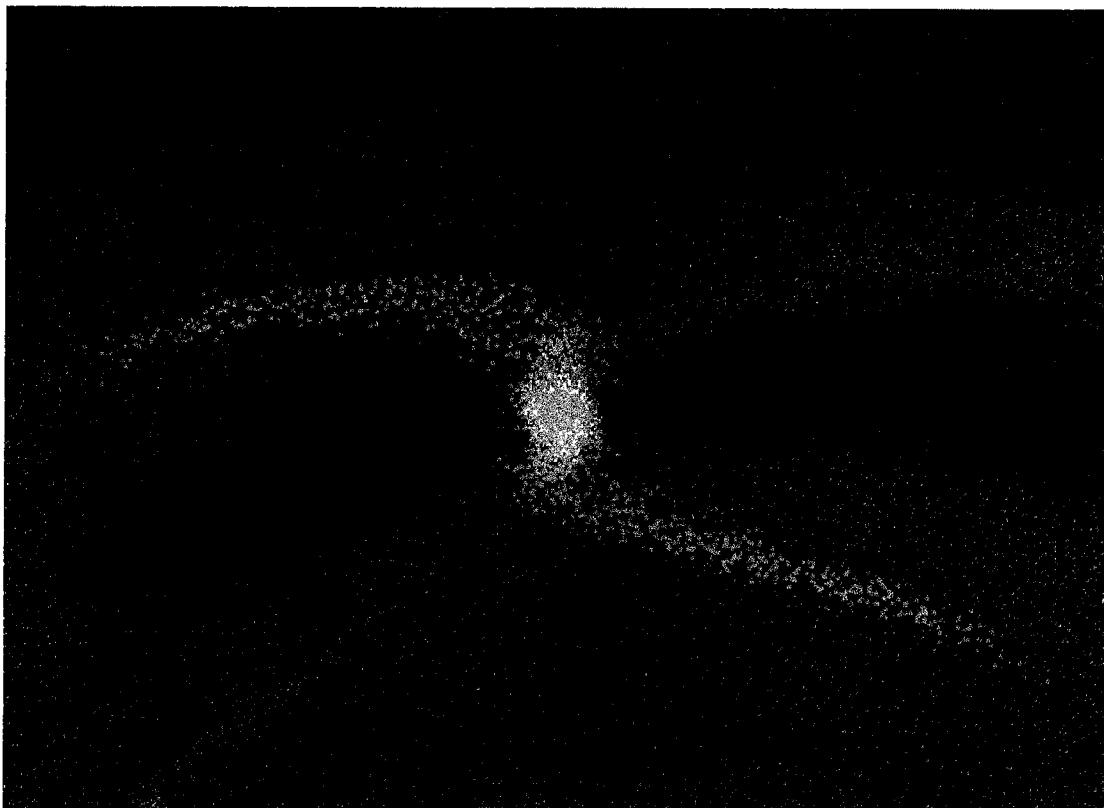


Figure 5.17: The same planet as in Figure 5.15, zoomed out to show the trailing and leading edge of the spiral density waves. Within two time steps, all the particles highlighted in green will be part of the planet. The exterior particles will be caught by the super-Keplerian trailing wave, and the interior particles will catch the sub-Keplerian leading wave. The shock will slow them, trapping them as part of the gas envelope of the planet. For non-planet particles, the color scale represents the logarithm of the gas density.

5.4.2 Description of Planet Mass Determination Algorithm

Initially, what we refer to as the “planet” is a single particle, interacting via the gravitational force only. As the system evolves, dissipation in the gas allows the planet particle to capture surrounding gas particles. The gas particles move along with the planet particle, contributing to the excitation of spiral density waves and migration. The “planet” is thus the original planet particle and some surrounding gas particles. How do we determine exactly which gas particles to include in this characterization? We use an iterative algorithm described below.

To start the algorithm, the mass and center of mass of the planet are those of the initial planet particle.

1. Using the mass and center of mass of the planet, determine the Hill radius (Equation 5.3) and Hill density, defined as

$$\rho_H = \frac{9M_\star}{4\pi r_p^3} \quad (5.4)$$

2. Find all gas particles that are within a Hill radius of the center of mass of the planet and have density greater than the Hill density.
3. Using the initial particle and all found gas particles, calculate the new mass and center of mass of the planet. If the new mass and center of mass are different from the old values, iterate again with Step 1. Else, we have determined the list of particles making up the planet.

5.4.3 Details of the Planet

The size of the planet is comparable to the gravitational softening length, meaning that its gravitational behavior is not being properly modeled. In addition, the assumptions justifying an isothermal equation of state are not valid for a planetary envelope. However, our simulations present the first opportunity to study a planet

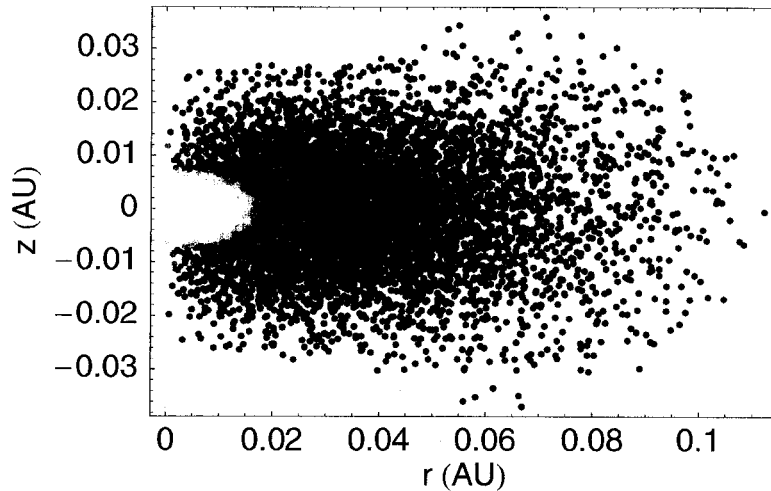


Figure 5.18: Projected density of particles making up a planet. The $0.01 M_{\odot}$ disk was composed of 400000 gas particles. The initial planet particle was $1 M_{\text{Jup}}$; the planet is now composed of an additional 7870 gas particles, a total of $1.19675 M_{\text{Jup}}$. The color represents the density. Angular momentum has flattened the planet into a disk with height less than a third of the radius. This planet has a rotation period of 0.53 yr.

that is more complicated than a point particle. We therefore discuss some observations about the structure of the planet, with the warning that these results should not be considered robust.

The planet, composed of the initial core particle and an envelope of gas particles, is a flattened disk rotating uniformly with the same sense as its orbital motion. Figure 5.18 shows the radial and vertical projection of the particles making up the planet. Note that the height of the planet is less than a third of the radius.

The planet is in almost completely uniform rotation about the vertical axis. As the planet accretes, its rotation speed increases nearly linearly. This increase slows as the planet carves a gap in the disk. The planet shown in Figure 5.18 has a rotation

period of 0.53 yr. Our simulation does not have the necessary resolution or physics to model the contraction of this large planetary envelope down to a fully-formed gas giant planet. Nonetheless, we know that angular momentum must be conserved. We can measure the spin angular momentum of our planet directly from the mass, position and velocity of the particles. The spin angular momentum of a sphere of mass M and radius R uniformly rotating with period T is $L_{\text{spin}} = \frac{2}{5}MR^2 2\pi/T$. This enables us to estimate the rotation period of the planet if we shrunk it to a sphere with the same density as Jupiter:

$$T_p = \frac{2}{5}M_p \left(\frac{M_p}{\frac{4}{3}\pi\rho_{\text{Jup}}} \right)^{2/3} \frac{2\pi}{L_{\text{spin}}} \quad (5.5)$$

For the planet shown in Figure 5.18 we have $M_p = 1.19675 M_{\text{Jup}}$ and $L_{\text{spin}} = 3.18 \times 10^{-6} M_{\odot} \text{ AU}^2/\text{yr}$. The current density of Jupiter is $\rho_{\text{Jup}} = 2.25 \times 10^6 M_{\odot}/\text{AU}^3$. This yields a rotation period of just over two hours for the shrunken planet, about five times shorter than Jupiter's. This is just slightly smaller than the escape velocity of the shrunken planet. We do not yet have observational evidence of the rotation speed of extrasolar planets. Perhaps we will find that they are rotating much faster than the giant planets in our Solar System. Alternatively, perhaps the contraction phase of giant planet formation involves the shedding of a significant fraction of the spin angular momentum.

5.5 Long Term Behavior

The results quoted above for migration and accretion rates are all derived from the first few hundred years of the evolution of the system. What happens if we continue the simulation, letting the planet move farther inward? The planet forms a gap in the disk. This changes the dynamics of the system, halting migration and changing the accretion rate. Here we discuss these changes and attempt to quantify the process of gap formation as seen in our simulations.

5.5.1 *The Density Profile and Gap Formation*

A consequence of accretion onto the planet is depletion of the gas making up the disk. The tidal force of the planet pushes material away from corotation, as seen in planetary ring systems. These actions combine to lower the gas density in a ring along the orbit of the planet. Such a depletion is called a gap in the disk. A gap physically disconnects the planet and its envelope from the inner and outer portions of the disk. This disconnect results in slower accretion and halts the migration of the planet. Figure 5.19 shows the semi-major axis and mass of a planet forming a gap in a $0.05 M_{\odot}$ disk. The vertically and azimuthally averaged surface density in the disk is shown for this simulation in Figure 5.20. As the planet accretes and exerts torques on the disk, it depletes a ring of gas around its orbit. The depth of the gap grows, resulting in a change in the migration of the planet. The disconnect from the disk is not complete, as shown in Figure 5.21. Gas from the disk can still accrete onto the planet through the spiral waves that reach through the gap.

We found the speed of gap formation to be sensitive primarily to the disk mass. Figures 5.19, 5.20 and 5.21 show a gap forming within about 250 years in a $0.05 M_{\odot}$ disk. In contrast, Figure 4.3 shows a gap forming in just 100 years in a $0.1 M_{\odot}$ disk. Finally, Figure 5.22 shows the result of a long simulation of a $0.01 M_{\odot}$ disk, taking closer to 1500 years to fully develop a gap.

5.5.2 *Halting Migration*

The current catalog of extrasolar planets exhibits a strong lower bound on the semi-major axis of giant planets. Are planets prevented from migrating closer than 0.04 AU to their parent star, or are all planets within that distance accreted onto the central star? Unfortunately, our simulations cannot shed much light on this mystery. We do not accurately resolve the region close to the central star, nor do we include forces such as magnetic fields and dissipation due to tidal forces between planet and star.

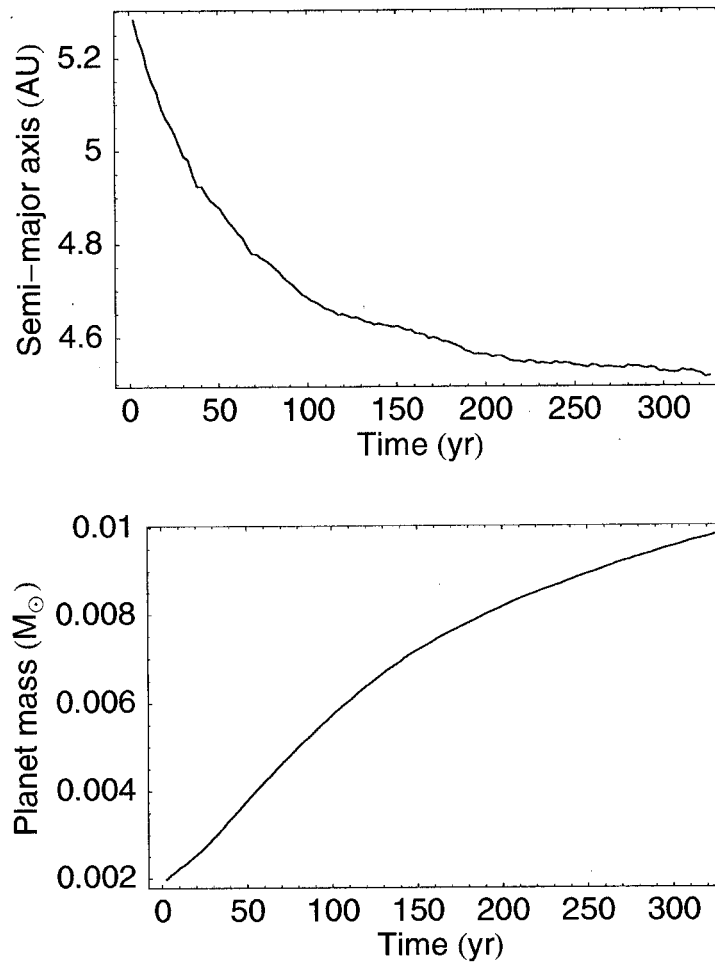


Figure 5.19: Semi-major axis and mass of a planet forming a gap in a $0.05 M_{\odot}$ disk. Notice that migration and accretion slow between 100 and 200 years after the start of the simulation. The initial mass of the planet was $1.9 M_{\text{Jup}}$ and the disk was composed of 80000 particles. Compare with the density profiles of this disk shown in Figure 5.20.

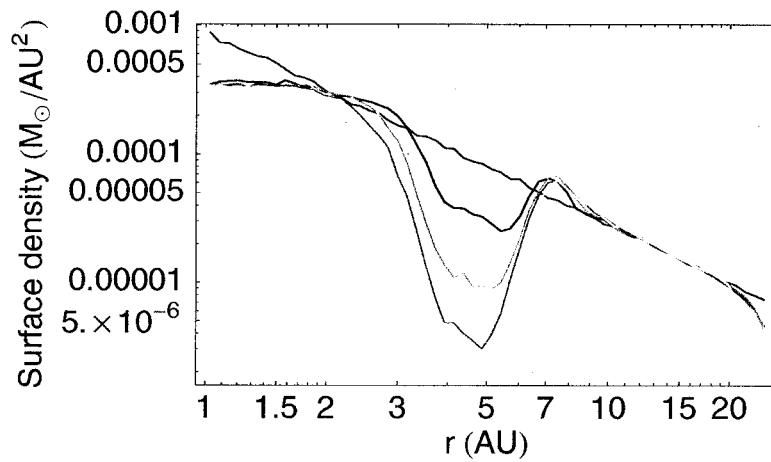


Figure 5.20: Surface density profiles of a planet forming a gap in a $0.05 M_{\odot}$ disk. Black is the initial condition, $\Sigma(r) \propto r^{-3/2}$. Blue is at 81 years, magenta at 163 years, red at 244 years, and yellow at 326. As the simulation proceeds, the density depression around the orbit of the planet deepens. Relating to the semi-major axis and mass shown in Figure 5.19, we see the gap move inward along with the planet, deepening as the planet grows in mass. When the simulation stops, the density in the gap is almost 100 times less than the initial conditions.

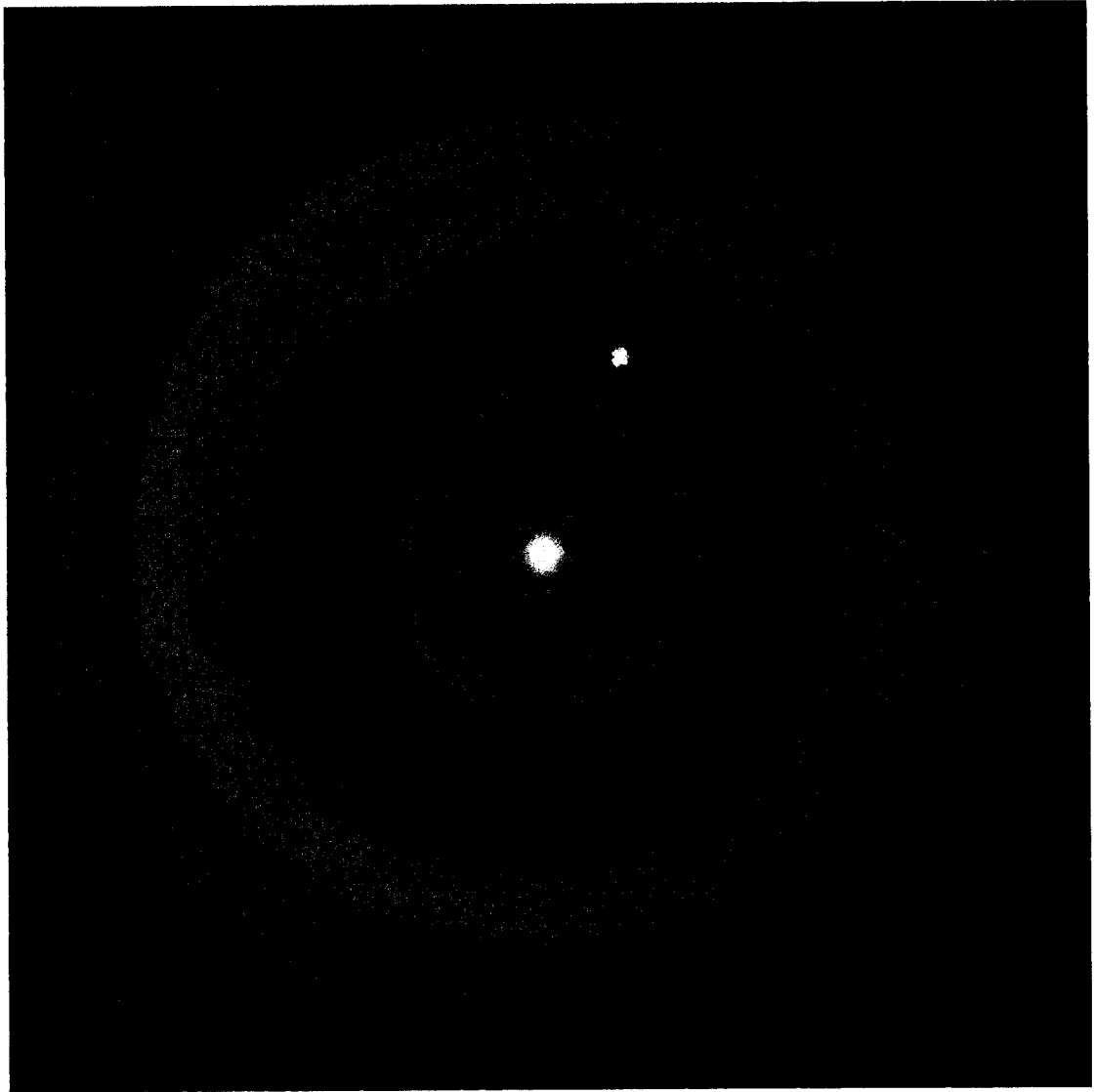


Figure 5.21: A snapshot of a simulation where the planet has formed a gap in the disk. The region along the orbit of the planet has been almost entirely depleted of material. However, the planet still excites spiral density waves, which reach in to touch the planet, allowing for continued accretion across the gap. The color scale represents the logarithm of the gas density.

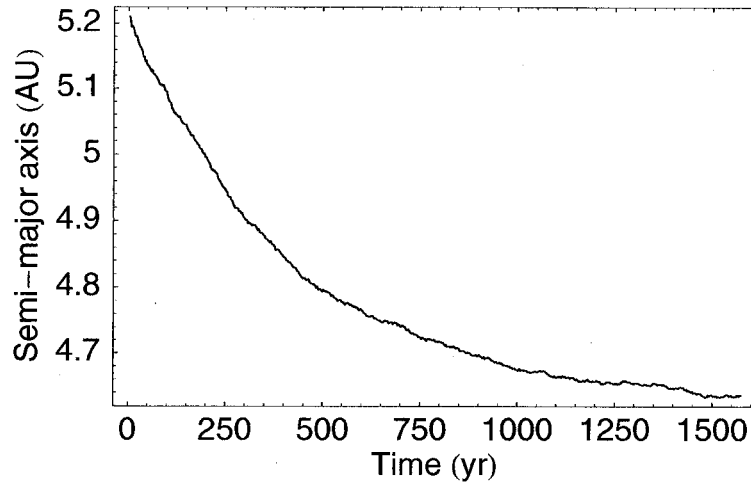


Figure 5.22: The semi-major axis of a $1 M_{\text{Jup}}$ planet in a $0.01 M_{\odot}$ disk, taking a long time to fully form a gap. At the endpoint of this simulation, the planet has grown to $3.7 M_{\text{Jup}}$ and is still accreting.

While we found that gap formation appeared to halt migration, our treatment of viscosity in the disk is too crude to suggest that Type II migration does not take place.

One possible solution neatly sidesteps the problem of halting migration, the “last of the Mohicans” scenario. In this case, a whole series of planets formed, migrated inward, and were accreted by their parent star over the lifetime of the protoplanetary disk. The planets we observe are simply the last members of this series; those left exposed when the disk dissipates. Our results are consistent with this theory but do not provide positive evidence for it.

5.6 Conclusions

Our simulations add to the body of knowledge that makes up modern cosmogony. Placing our results in context with the current framework of planet formation and

migration, we summarize and conclude. Note that we mention the results of Chapter 4 as well as this chapter.

We have simulated the migration of giant planets in gaseous circumstellar disks using the smoothed particle hydrodynamics technique. These are the first fully three-dimensional simulations of this problem that treat the self-gravity of the disk, allow for the planet to dynamically migrate and accrete, and have free boundary conditions. We used a simple isothermal equation of state with imposed radial temperature profile of $T(r) \propto r^{-1}$. The initial surface density of the disk was $\Sigma(r) \propto r^{-3/2}$, as suggested by the minimum mass solar nebula model. The initial vertical distribution was determined by the equilibrium pressure support of the tide from the central star. We used disks of mass 0.01–0.2 M_{\odot} around 1 M_{\odot} stars. For migration and triggered formation runs, we inserted planets of mass 0.25–2 M_{Jup} into the disk on initially circular orbits at 5.2 and 12.5 AU.

With this choice of equation of state, massive disks are unstable to local gravitational collapse, forming gas giant planets on a timescale of a few hundred years. For a small, but interesting, region of parameter space, the instability can be triggered in otherwise stable disks by an already formed planet. Such disks will typically form several planets, often on significantly non-circular orbits. The planets will disrupt the disk and the evolution of the system will be governed by the dynamical gravitational interaction of the planets with each other, as opposed to the disk. Given the chaotic nature of those interactions, we cannot at this time make any predictions as to the final distribution of orbital semi-major axis and eccentricity in such systems. However, the nature of many-body interactions suggests that large eccentricities, as observed in extrasolar planetary systems, may be quite common.

Lower-mass disks are gravitationally stable. If the solid core of a giant planet forms in such a disk, it will experience significant orbital migration during its lifetime. The migration is a result of secular interaction with the gas disk. The planet excites spiral density waves by exchanging angular momentum with material at the Lindblad

and corotation resonances. These non-axisymmetric perturbations torque back on the planet. The net effect is inward migration of the planet. Theoretical treatments of this problem suggest that migration rate should be proportional to both the planet and disk mass. Our simulations partially agree with this result, finding linear dependence on the disk mass, but independence of the planet mass. We believe that this is because the response of the disk is not linearly proportional to the planet mass, as assumed by the theory. A giant planet of $1 M_{\text{Jup}}$ at 5.2 AU in a $0.01 M_{\odot}$ disk will migrate inward at 10^{-3} AU/yr for several hundred years. During this time period it will accrete gas from the surrounding disk.

The tidal torques exerted by the planet will push disk material on nearby orbits away from corotation. Combined with accretion, this process will form a gap in the disk, where gas density is several orders of magnitude below the initial value. The gap halts the migration of the planet. A giant planet of $1 M_{\text{Jup}}$ at 5.2 AU in a $0.01 M_{\odot}$ disk will form a gap in about 1500 years, with a final orbit of 4.6 AU. At this point, viscosity in the disk may lead to further, Type II, migration.

How do these results fit into the story of modern cosmogony, and what questions still need to be answered?

The planet formation results provide intriguing evidence for an alternate theory of planet formation. However, other research indicates that our equation of state is overly optimistic for the conditions. Further work investigating the thermal evolution of circumstellar disks is needed.

Prior to the situation our migration simulations start from is the growth of solid bodies from dust to rocks to planetesimals to several-Earth-mass cores. This problem will likely remain out of the reach of direct simulation for some time. Approximate methods, like the particle-in-a-box and shearing patch, must be judiciously applied to tell us the spatial and size distributions of solid material in the disk. The coupling of solids to the gas, usually assumed to simply stop abruptly for objects larger than a few meters, is likely much more complicated.

The distribution of gas in the disk and its temperature need to be explained. Simulations of star formation are a likely candidate for providing this data. By following the collapse of a slowly rotating cloud, the parameters of newly formed circumstellar disks can be found. The density of the star-forming region is probably an important factor.

The planet migration results confirm a puzzling situation in the process of planetary evolution. Rapid migration suggests that planets would quickly be swallowed by their parent star after forming. Yet observational evidence shows that planet formation is robust. Areas for further research include more sophisticated treatment of radiative transfer, the gravitational interaction of material close to the planet, the process of accretion onto the planet and the behavior of multiple-planet systems. In addition, new ideas for halting migration should be pursued.

Of particular interest to us here on Earth is the effect of giant planet on the formation and fate of terrestrial-size planets. Direct simulations of the long-term stability of orbits in extrasolar planetary systems may affect our assumptions about the commonality of habitable zones.

Finally, how and when is the gas disk dispersed? If due to stellar winds, a better theory of young stars is needed to explain such a powerful force. If due to accretion, we require a better understanding of viscous processes in circumstellar disks.

As seen by the number of questions above, cosmogony is still an incomplete theory. Hopefully the contributions of our work will form a basis for a better explanation of the formation and evolution of planetary systems.

Chapter 6

SIMULATION VISUALIZATION TOOLS

A computer program used to run simulations is useless without accompanying tools to analyze and visualize the results. When developing and testing a simulation tool, an analysis and visualization package allows the researcher to identify errors in the simulation, investigate their source and obtain the information needed to fix the problem. A mature simulation tool can be used to produce prodigious amounts of simulated data which must be processed. Flexible tools enable the discovery of qualitative and quantitative relationships that were not conceived of during the writing of the original program.

This chapter describes part of the development of SALSA, a flexible tool for parallel analysis and visualization of particle-based data.

6.1 The Need for Parallel Analysis Tools

The size of simulations advances with the available computer processing power. The growth of computational clusters, in addition to individual processor speeds following Moore's Law, has allowed researchers to run enormous simulations, producing more data than they know how to analyze. One solution is to perform the analysis using the same technique that enabled the simulation: parallel processing.

Writing a simulation tool that works efficiently in parallel is a difficult task. A problem is first broken into several pieces which are distributed across the parallel machine. Any non-trivial problem requires a complex pattern of communication between the problem domains. However, once a successful strategy for decomposing the

work has been found, the simulation proceeds as a predetermined series of well-defined operations. When analyzing a simulation, the “series of well-defined operations” is not predetermined, rather it is subject to the whims of the user. A parallel analysis tool must therefore provide many operations, each of which should take advantage of the parallel machine, and allow the user to string together an arbitrary sequence of those operations. While previous analysis tools have provided a limited level of user control, they do not work in parallel, and thus are ineffective when presented with today’s large simulations. SALSA provides the parallel primitives necessary to process enormous quantities of data. In addition, it incorporates a full-fledged scripting language, allowing the user unprecedented flexibility.

6.2 SALSA’s *First Task: Simple Visualization*

Here we describe the layout of the SALSA program and describe its first major feature.

SALSA is a computer program used to visualize and analyze particle-based data in parallel. It has a client-server architecture. The client is written in Java and runs on the user’s local machine. The server is written in C++ using the Charm++ framework and runs on a parallel machine (Parallel Programming Lab). By utilizing a parallel library backend, we avoid writing difficult and error-prone code dealing with network and inter-process communication. In addition, no changes to our source code are necessary when we wish to utilize a new machine architecture.

6.2.1 Particle Data

Our data is composed of particles, each of which has various attributes. An *attribute* is a named scalar or vector value of specific type. Examples of attributes include mass, position, velocity and energy. A *particle* is a collection of any number of attributes. A set of particles that all have the same kinds of attributes is called a *family*. Examples of families might be dark matter particles and gas particles. Finally, a *simulation* is

a set of named families.

The details of how attributes and particles are stored in memory or on disk are unimportant. We require only an interface that allows access to each attribute of each particle of each family. In addition, we require a way of ordering the particles to facilitate domain decomposition.

6.2.2 Domain Decomposition

Because analysis and visualization suggest no natural division of work, domain decomposition in SALSA will be somewhat arbitrary. It is hoped that this will avoid worst-case performance in the majority of common tasks. The current method of domain decompositions splits the particles evenly along an ordering. The nature of the ordering, position along a space-filling curve, makes this splitting equivalent to making cuts through a binary spatial tree. While the visualization operation does not currently use the tree for an algorithmic speedup, this is a future goal.

6.2.3 Visualization

The most straightforward way to visualize a set of particle data is to project the positions of the particles onto a viewing plane. Particles can be colored by some function of their attributes. This technique has been implemented in several programs, notably SALSA's direct inspiration TIPSY (Neal Katz and Thomas Quinn). SALSA reproduces this functionality, adding a novel heuristic that allows intuitive rotations. In addition to simple visualization, the core functionality of SALSA includes the ability to define particle colors based on a range of attribute values. Groups can also be specified by attribute ranges, and are used to selectively display a portion of the entire simulation.

6.2.4 *Projection onto the Viewing Plane*

The simulation exists in a three-dimensional space spanned by the Cartesian coordinates (x, y, z) . The viewing screen is two-dimensional, so we must project the simulation onto a plane, known as the viewing plane or the visual. In this discussion we do not address perspective, instead we assume all views are orthonormal.

The visual is composed of an array of $w \times h$ pixels. Valid pixel locations are pairs (i, j) with $i \in \{0, 1, \dots, w - 1\}$, $j \in \{0, 1, \dots, h - 1\}$; pixel coordinates start in the upper-left corner.

The viewing panel array of pixels is mapped onto the simulation space by defining the point at the center of the view, the orientation of the view with respect to that point, and the width and height of the view. In addition, we require that the aspect ratio of pixels be fixed at unity. This defines a parallelepiped through the simulation volume, shown in Figure 6.1. In the visual, the x -axis increases to the right and the y -axis increases up. Each pixel is square with side-length δ in simulation coordinates. All the particles in the parallelepiped are then “squashed” down onto the viewing plane. This is done by taking the dot product of the position of the particles with the x - and y -axes of the viewing plane. Figure 6.2 shows the view looking down the aligned viewing parallelepiped. This area has a width and height in floating-point simulation coordinates that are mapped to the integer-valued pixel coordinates. When rendering “pointlike” images, the projected position on the viewing plane is rounded to the nearest integer, yielding a single pixel coordinate for each particle. This pixel is assigned a value based on the properties of the particle, the value of each particle having been determined earlier by the user. When multiple particles map onto the same pixel, we choose the particle with the highest value. Figure 6.3 shows a pointlike visual produced by SALSA. When rendering “splatter” visuals, a single particle can map to several pixels, and pixel values are assigned additively, as described in the next section.

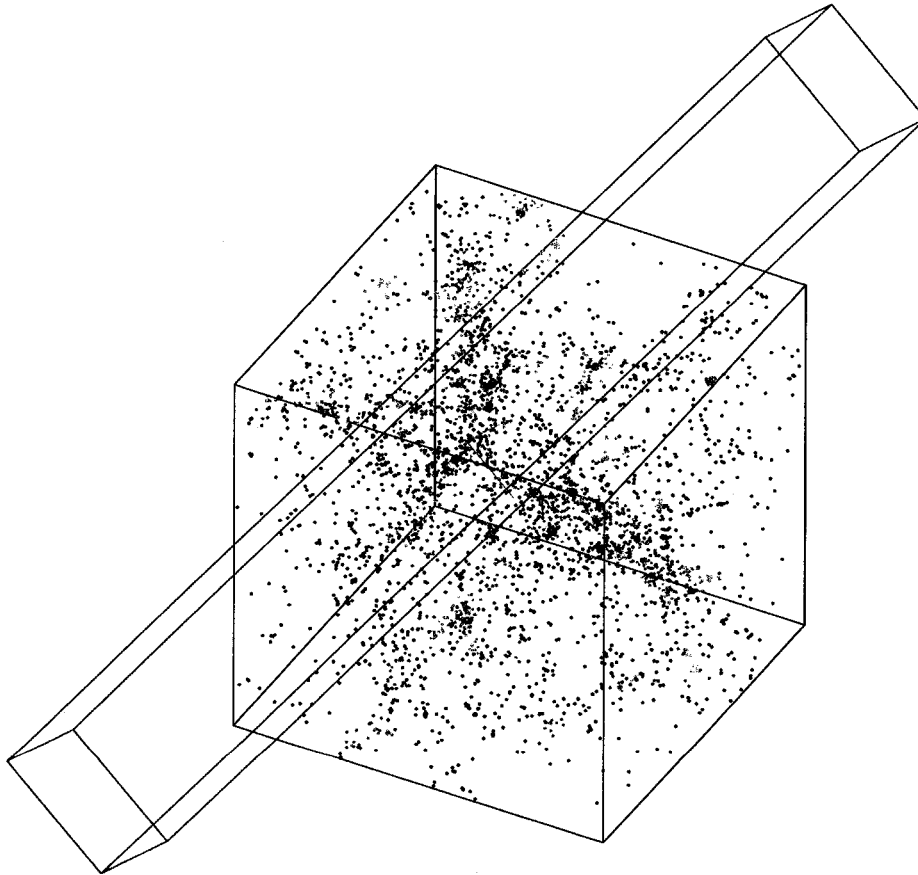


Figure 6.1: A view of a three-dimensional simulation is defined by an infinite parallelepiped through the simulation volume. Here the particles are contained in a cube. Specifying the center, the orientation, and the width and height of the view defines the parallelepiped. Figure 6.2 shows the view down the parallelepiped for this configuration.

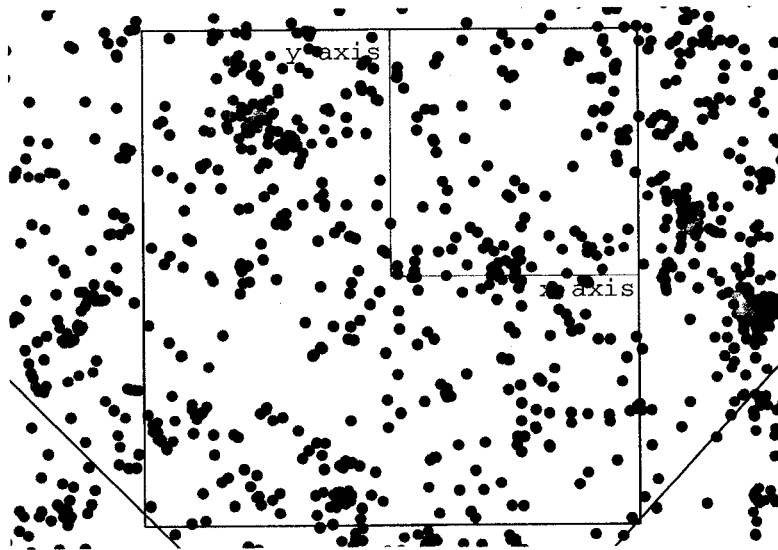


Figure 6.2: The axes of a view through a simulation. The origin is in the center of the view. Particles in this cross-section will be placed into the pixel array, depending on their position and color. Figure 6.3 shows a pointlike view rendered by SALSA. Figure 6.5 shows the same view, but with splatter rendering.

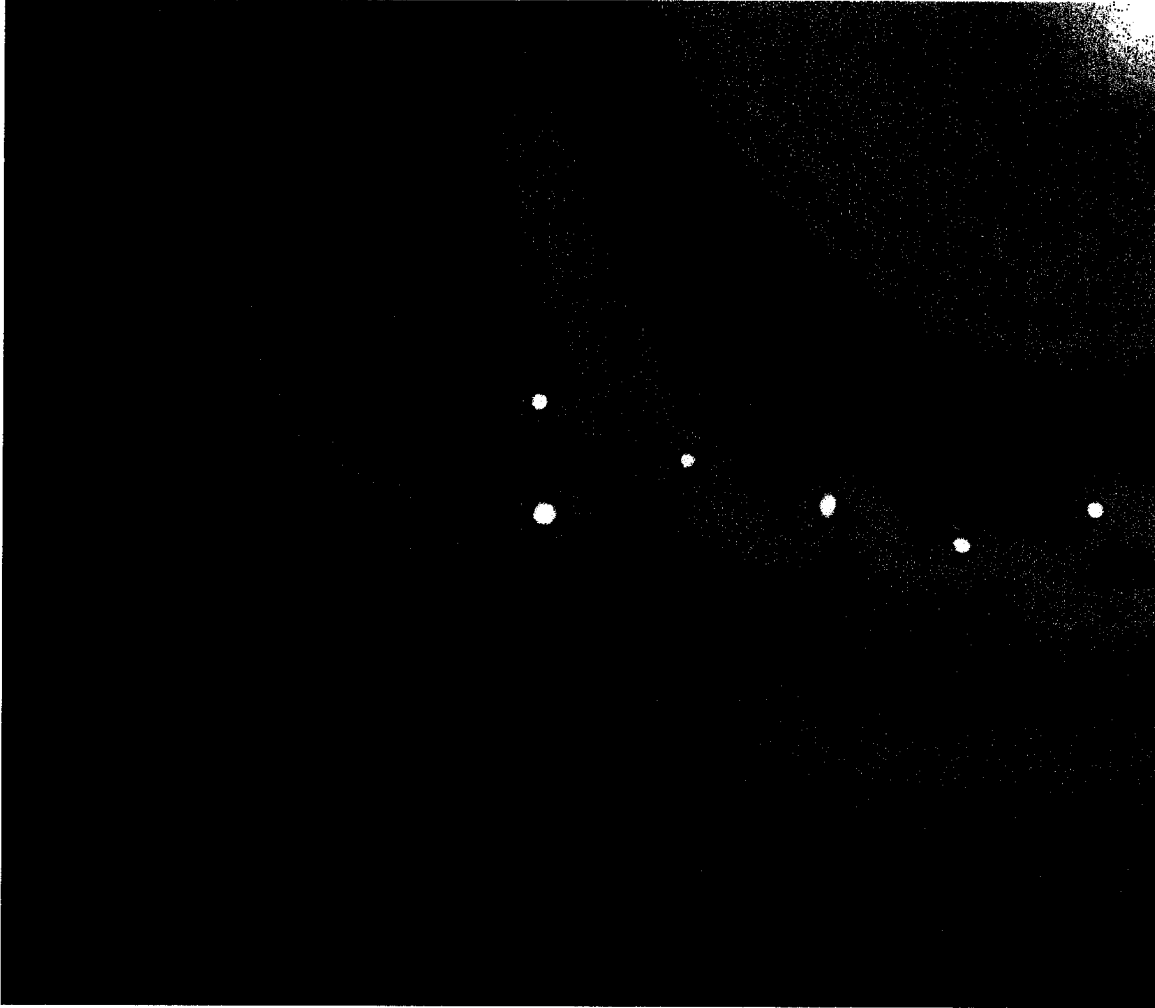


Figure 6.3: A planet formation simulation rendered pointlike by SALSA. Each particle maps to the single pixel nearest its projected center. The value of that pixel is determined by an attribute of the particle, in this case the logarithm of the density, mapped to an 8-bit integer. If more than one particle lands in the same pixel, the value of the pixel is taken to be the maximum of the individual values. The pixel value is turned into a color using the WRBB color palette.

6.3 SPH Splatter Visuals

An SPH particle represents a “blob” of gas with a specific size and spatial distribution determined by the smoothing length and kernel, respectively. When viewing a simulation including SPH particles, a single pixel is usually a misleading representation of how the particle behaves in the simulation. To present a visualization that more accurately reflects the non-pointlike nature of SPH particles, we use a technique affectionately known as “splatter”-ing the particles across the visual. In this technique each SPH particle contributes luminance to several pixels surrounding its projected position, the amount depending on the weight of the kernel in the pixel, using the smoothing length of the particle, as shown in Figure 6.4. After all particles have completed this process a palette can be applied to the luminance information to create a false color image.

This process is analogous to using a charge-coupled device to take a digital photograph. With a CCD, the number of photons hitting a pixel determine its brightness. A single pixel can accept photons from any number of sources. When the array is read off, a false-color palette can be applied to create a color image. In a splatter visual, the quantity being counted in each pixel is not the amount of light received, but a weighted mass density. In addition, there is nothing analogous to the color filters used with a CCD.

6.3.1 Pixel Deposition

Given a particle with mass m , smoothing length h and visual-projected position (x, y) , which pixels should this particle contribute to and in what amounts? To determine this, we use the physical size of the particle and its mass distribution, which is defined by the smoothing kernel. The particle will contribute to all the pixels within a radius of $2h$ of the projected center of the particle (x, y) . To determine what contribution each pixel in the circle should receive, we project the three-dimensional kernel onto

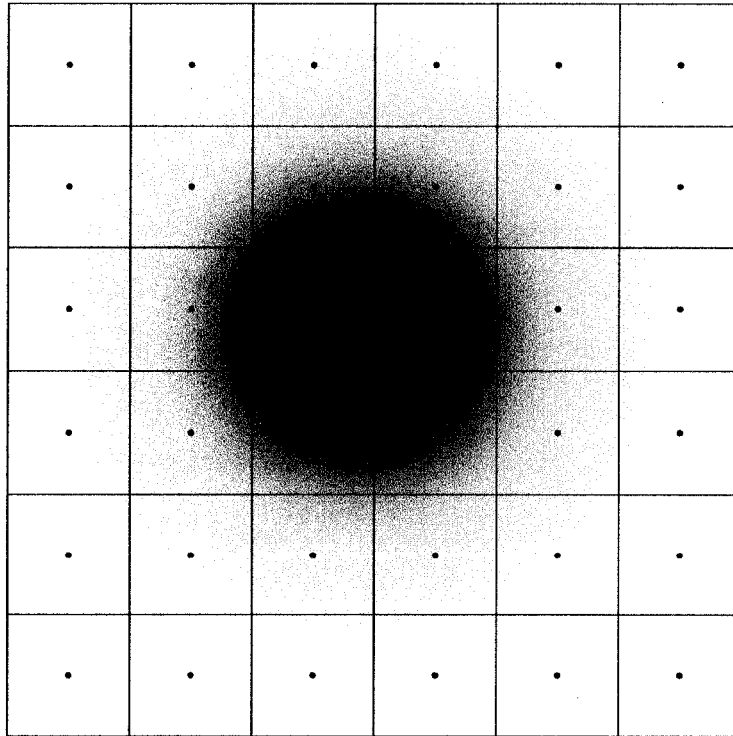


Figure 6.4: In a splatter visual, a single SPH particle can contribute to several pixels. The contribution to a particular pixel is taken as the value of the projected kernel at the center of the pixel multiplied by the area of the pixel.

the viewing plane, obtaining the surface density. For the spherically symmetric cubic-spline kernel (Equation 2.3) the projected kernel can be expressed analytically for a particle of mass m and smoothing length h :

$$\Sigma(r) = \begin{cases} \frac{m}{\pi h^2} \left(4f\left(\frac{1}{2}\frac{r}{h}\right) - f\left(\frac{r}{h}\right) \right) & \text{for } r < h \\ \frac{m}{\pi h^2} 4f\left(\frac{1}{2}\frac{r}{h}\right) & \text{for } h \leq r < 2h \\ 0 & \text{for } r \geq 2h \end{cases} \quad (6.1)$$

$$f(x) = \left(\frac{1}{2} + \frac{13}{4}x^2 \right) \sqrt{1-x^2} - \left(3 + \frac{3}{4}x^2 \right) x^2 \log\left(\frac{1 + \sqrt{1-x^2}}{x} \right) \quad (6.1a)$$

This expression for the surface density is used in Figure 6.4.

A fully correct algorithm for the deposition into a pixel would be: for each pixel that is contained in part or entirely by the circle of radius $2h$ about the point (x, y) , add the amount $\int \Sigma(r') dx' dy'$, the integral of the surface density over the square pixel area, where r' is the distance from the point (x', y') to the center of the particle (x, y) . This integral cannot be done analytically and would be prohibitively expensive to perform numerically. We therefore use an approximate method: for each pixel whose center is within the circle of radius $2h$ about the point (x, y) , add the amount $m\Sigma(r')\delta^2$ where r' is the distance from (x, y) to the center of the pixel and δ is the width and height of the pixel. As the full expression for the surface density (Equation 6.1) is expensive to calculate, it is tabulated before any visualization is done, and the values used are interpolated from the table using a cubic-spline, scaled by the appropriate value of h . Additionally, if the circle is completely contained by one pixel, that pixel receives the full contribution m . There is an additional scaling factor to convert the floating point values to numbers in the range 0–255, as the pixel array is made up of 8-bit integer values. Figure 6.5 shows the same simulation as Figure 6.3 with a splatter rendering as described above.



Figure 6.5: A planet formation simulation rendered splatter by SALSA. Each particle can map to multiple pixels, determined by its smoothing length. The value of each pixel is determined by the value of the smoothing kernel at that distance from the center of the particle. Contributions to the same pixel from different particles are combined additively. The pixel value is turned into a color using the WRBB color palette. Compared with Figure 6.3, this picture more closely agrees with how the physical forces are calculated by the simulation tool. It shows the gas to be more like a continuous fluid than the pointlike representation suggests.

6.3.2 Color

When all relevant particles have been rendered onto the visual, we have an array of pixel values. Each pixel is an 8-bit value. This array is then passed to a client program over a network connection. The client program then determines the RGB color of each pixel by applying a 256-entry color palette, and displays the visual. Without re-rendering the scene, the color palette can be manipulated to visually highlight different areas of the simulation.

The WRBB Color Palette

One of the most popular color palettes is known as “WRBB”, or “white-red-blue-black”. This palette provides the human eye with excellent awareness of color changes. It is usually applied so that black and blue represent smaller values, while red, yellow and white show higher values. Its name omits two of the colors in the gradient; the full progression is black, blue, purple, red, yellow, white. For a red-green-blue (RGB) color display, this can be formulated as five linear ramps of a single color component. An RGB triplet is three numbers between zero and one giving the strength of the red, green, and blue channels, respectively. The WRBB color palette proceeds from black $(0, 0, 0)$ to blue $(0, 0, 1)$, linearly increasing the blue component for one fifth of the total length of the palette. It then ramps the red component up to get purple $(1, 0, 1)$; blue is ramped down to get red $(1, 0, 0)$; green is ramped up to get yellow $(1, 1, 0)$; finally blue is ramped up to get white $(1, 1, 1)$. This algorithm can be applied to any length color palette, breaking it into five nearly equal chunks. The program TIPSY uses a slightly different formulation of the WRBB palette. All the images of simulations in this work have used the WRBB color palette just described, usually representing density or logarithmic density.

6.4 The Future of SALSA

As of this writing, SALSA is in active development. The goal is to create a full-featured tool used by researchers worldwide. To that end, we have several near- and long-term goals.

SALSA currently embeds the scripting language Python to provide high-level control of the server program to the user (Python Programming Language). The framework for this integration is still being developed. When it has stabilized, we will add functionality to the scripting interface, exposing more functions to the control of the user. For example, we will allow the user to write scripts to render sequences of images, to form a movie.

We plan to add a low-level scripting interface as well. In this case, a user could provide a function that modifies an individual particle, and apply it to a group of particles. This would, for example, allow the creation of new attributes for a family of particles.

A longer-term goal is the ability to manipulate a time-series of simulation data. We would like to provide the user the ability to move the simulation forward and backward in time as easily as we currently move in space.

Eventually, we plan to merge the force calculations done by the simulation code into the analysis tool. By doing so, we allow the user to visualize how forces are calculated. Adding a time-stepping scheme, this would erase the difference between simulation tool and analysis tool. A combined code-base would increase the flexibility of both tools.

The time-scale for implementing these features ranges from months to years. Visit the NChilada project web site for up-to-date information on SALSA (NChilada Project).

BIBLIOGRAPHY

- P. J. Armitage and B. M. S. Hansen. Early planet formation as a trigger for further planet formation. *Nature*, 402:633–635, December 1999.
- P. Artymowicz. On the Wave Excitation and a Generalized Torque Formula for Lindblad Resonances Excited by External Potential. *ApJ*, 419:155+, December 1993.
- D. S. Balsara. von Neumann stability analysis of smooth particle hydrodynamics—suggestions for optimal algorithms. *Journal of Computational Physics*, 121:357–372, 1995.
- R. Barnes and S. N. Raymond. Predicting Planets in Known Extra-Solar Planetary Systems I: Test Particle Simulations. *ArXiv Astrophysics e-prints*, February 2004.
- M. R. Bate, I. A. Bonnell, and V. Bromm. The formation of a star cluster: predicting the properties of stars and brown dwarfs. *MNRAS*, 339:577–599, March 2003a.
- M. R. Bate and A. Burkert. Resolution requirements for smoothed particle hydrodynamics calculations with self-gravity. *MNRAS*, 288:1060–1072, July 1997.
- M. R. Bate, S. H. Lubow, G. I. Ogilvie, and K. A. Miller. Three-dimensional calculations of high- and low-mass planets embedded in protoplanetary discs. *MNRAS*, 341:213–229, May 2003b.
- E. Battaner. *Astrophysical Fluid Dynamics*. Astrophysical Fluid Dynamics, Cambridge, New York: Cambridge University Press, ISBN 0521431662, 1996.

- S. V. W. Beckwith and A. I. Sargent. The occurrence and properties of disks around young stars. In *Protostars and Planets III*, pages 521–541, 1993.
- S. V. W. Beckwith, A. I. Sargent, R. S. Chini, and R. Guesten. A survey for circumstellar disks around young stellar objects. *AJ*, 99:924–945, March 1990.
- J. Binney and S. Tremaine. *Galactic Dynamics*. Princeton, NJ, Princeton University Press, 747 p., 1987.
- Boost Developers. Boost.org C++ Libraries. <http://www.boost.org>, 2004.
- A. P. Boss. Giant planet formation by gravitational instability. *Science*, 276:1836–1839, 1997.
- A. P. Boss. Temperatures in Protoplanetary Disks. *Annual Review of Earth and Planetary Sciences*, 26:53–80, 1998.
- A. P. Boss. Possible Rapid Gas Giant Planet Formation in the Solar Nebula and Other Protoplanetary Disks. *ApJ*, 536:L101–L104, June 2000.
- A. P. Boss. Gas Giant Protoplanet Formation: Disk Instability Models with Thermodynamics and Radiative Transfer. *ApJ*, 563:367–373, December 2001.
- A. P. Boss. Evolution of the Solar Nebula. V. Disk Instabilities with Varied Thermodynamics. *ApJ*, 576:462–472, September 2002.
- W. V. Boynton. Meteoritic evidence concerning conditions in the solar nebula. In *Protostars and Planets II*, pages 772–787, 1985.
- G. Bryden, X. Chen, D. N. C. Lin, R. P. Nelson, and J. C. B. Papaloizou. Tidally Induced Gap Formation in Protostellar Disks: Gap Clearing and Suppression of Protoplanetary Growth. *ApJ*, 514:344–367, March 1999.

- R. G. Cionco and A. Brunini. Orbital migrations in planetesimal discs: N-body simulations and the resonant dynamical friction. *MNRAS*, 334:77–86, July 2002.
- G. D’Angelo, T. Henning, and W. Kley. Nested-grid calculations of disk-planet interaction. *A&A*, 385:647–670, April 2002.
- G. D’Angelo, W. Kley, and T. Henning. Orbital Migration and Mass Accretion of Protoplanets in Three-dimensional Global Computations with Nested Grids. *ApJ*, 586:540–561, March 2003.
- Charles Darwin. *On the Origin of Species*. 1859.
- R. Dawkins. *The Selfish Gene*. Oxford University Press, 2nd Ed., 1989.
- W. Dehnen. Towards optimal softening in three-dimensional N-body codes - I. Minimizing the force error. *MNRAS*, 324:273–291, June 2001.
- A. Del Popolo, M. Gambera, and N. Ercan. Migration of giant planets in planetesimal discs. *MNRAS*, 325:1402–1410, August 2001.
- M. J. Duncan and T. Quinn. The long-term dynamical evolution of the solar system. *ARA&A*, 31:265–295, 1993.
- C. F. Gammie. Nonlinear Outcome of Gravitational Instability in Cooling, Gaseous Disks. *ApJ*, 553:174–183, May 2001.
- P. Goldreich and S. Tremaine. The excitation and evolution of density waves. *ApJ*, 222:850–858, June 1978a.
- P. Goldreich and S. Tremaine. The formation of the Cassini division in Saturn’s rings. *Icarus*, 34:240–253, May 1978b.
- P. Goldreich and S. Tremaine. The excitation of density waves at the Lindblad and corotation resonances by an external potential. *ApJ*, 233:857–871, November 1979.

- P. Goldreich and S. Tremaine. Disk-satellite interactions. *ApJ*, 241:425–441, October 1980.
- J. M. Hahn and R. Malhotra. Orbital Evolution of Planets Embedded in a Planetesimal Disk. *AJ*, 117:3041–3053, June 1999.
- C. Hayashi, K. Nakazawa, and Y. Nakagawa. Formation of the solar system. In *Protostars and Planets II*, pages 1100–1153, 1985.
- L. Hernquist and N. Katz. TREESPH - A unification of SPH with the hierarchical tree method. *ApJS*, 70:419–446, June 1989.
- J. J. Hester, P. A. Scowen, R. Sankrit, T. R. Lauer, E. A. Ajhar, W. A. Baum, A. Code, D. G. Currie, G. E. Danielson, S. P. Ewald, S. M. Faber, C. J. Grillmair, E. J. Groth, J. A. Holtzman, D. A. Hunter, J. Kristian, R. M. Light, C. R. Lynds, D. G. Monet, E. J. O’Neil, E. J. Shaya, K. P. Seidemann, and J. A. Westphal. Hubble Space Telescope WFPC2 Imaging of M16: Photoevaporation and Emerging Young Stellar Objects. *AJ*, 111:2349–+, June 1996.
- D. J. Hollenbach, H. W. Yorke, and D. Johnstone. Disk Dispersal around Young Stars. In *Protostars and Planets IV*, pages 401–+, May 2000.
- J. D. Jackson. *Classical Electrodynamics*. New York: Wiley, 3rd ed., 1999.
- N. Katz, D. H. Weinberg, and L. Hernquist. Cosmological Simulations with TreeSPH. *ApJS*, 105:19–+, July 1996.
- W. Kley. Mass flow and accretion through gaps in accretion discs. *MNRAS*, 303: 696–710, March 1999.
- W. Kley, G. D’Angelo, and T. Henning. Three-dimensional Simulations of a Planet Embedded in a Protoplanetary Disk. *ApJ*, 547:457–464, January 2001.

- D. E. Knuth. *The Art of Computer Programming Vol. II: Seminumerical Algorithms*. Addison-Wesley, Reading, MA, 2nd edition, 1981.
- D. N. C. Lin and J. C. B. Papaloizou. On the tidal interaction between protostellar disks and companions. In *Protostars and Planets III*, pages 749–835, 1993.
- D. N. C. Lin, J. C. B. Papaloizou, C. Terquem, G. Bryden, and S. Ida. Orbital Evolution and Planet-Star Tidal Interaction. In *Protostars and Planets IV*, pages 1111–+, May 2000.
- J. J. Lissauer and G. R. Stewart. Growth of planets from planetesimals. In *Protostars and Planets III*, pages 1061–1088, 1993.
- S. H. Lubow, M. Seibert, and P. Artymowicz. Disk Accretion onto High-Mass Planets. *ApJ*, 526:1001–1012, December 1999.
- G. Lufkin, T. Quinn, J. Wadsley, J. Stadel, and F. Governato. Simulations of gaseous disc-embedded planet interaction. *MNRAS*, 347:421–429, January 2004.
- R. Malhotra. Migrating planets. *Scientific American*, 281:56–63, 1999.
- G. W. Marcy and R. P. Butler. Planets Orbiting Other Suns. *PASP*, 112:137–140, February 2000.
- M. Matsumoto and T. Nishimura. Mersenne Twister: A 623-dimensionally equidistributed uniform pseudorandom number generator. *ACM Trans. on Modeling and Computer Simulation*, 8:3–30, January 1998.
- L. Mayer, T. Quinn, J. Wadsley, and J. Stadel. Formation of Giant Planets by Fragmentation of Protoplanetary Disks. *Science*, 298:1756–1759, November 2002.
- L. Mayer, T. Quinn, J. Wadsley, and J. Stadel. The evolution of gravitationally unstable protoplanetary disks: fragmentation and possible giant planet formation. *ArXiv Astrophysics e-prints*, October 2003.

- M. Mayor and D. Queloz. A Jupiter-Mass Companion to a Solar-Type Star. *Nature*, 378:355–+, November 1995.
- M. J. McCaughrean, K. R. Stapelfeldt, and L. M. Close. High-Resolution Optical and Near-Infrared Imaging of Young Circumstellar Disks. In *Protostars and Planets IV*, pages 485–+, May 2000.
- E. E. Mendoza V. Infrared Photometry of T Tauri Stars and Related Objects. *ApJ*, 143:1010–+, March 1966.
- E. E. Mendoza V. Infrared Excesses in T Tauri Stars and Related Objects. *ApJ*, 151: 977–+, March 1968.
- J. J. Monaghan. Smoothed particle hydrodynamics. *ARA&A*, 30:543–574, 1992.
- C. D. Murray and S. F. Dermott. *Solar system dynamics*. Cambridge University Press, 1999.
- N. Murray, B. Hansen, M. Holman, and S. Tremaine. Migrating Planets. *Science*, 279:69–+, January 1998.
- J. Muzerolle, S. T. Megeath, R. A. Gutermuth, L. E. Allen, J. L. Pipher, L. Hartmann, K. D. Gordon, D. L. Padgett, A. Noriega-Crespo, P. C. Myers, G. G. Fazio, G. H. Rieke, E. T. Young, J. E. Morrison, D. C. Hines, K. Y. L. Su, C. W. Engelbracht, and K. A. Misselt. The 24-Micron View of Embedded Star Formation in NGC 7129. *ArXiv Astrophysics e-prints*, June 2004.
- NChilada Project. <http://nchilada.astro.washington.edu/nchilada>.
- Neal Katz and Thomas Quinn. <http://hpcc.astro.washington.edu/tools/tipsy/tipsy.html>.

- A. F. Nelson and W. Benz. On the Early Evolution of Forming Jovian Planets. I. Initial Conditions, Systematics, and Qualitative Comparisons to Theory. *ApJ*, 589: 556–577, May 2003a.
- A. F. Nelson and W. Benz. On the Early Evolution of Forming Jovian Planets. II. Analysis of Accretion and Gravitational Torques. *ApJ*, 589:578–604, May 2003b.
- A. F. Nelson, W. Benz, F. C. Adams, and D. Arnett. Dynamics of Circumstellar Disks. *ApJ*, 502:342–+, July 1998.
- A. F. Nelson, W. Benz, and T. V. Ruzmaikina. Dynamics of Circumstellar Disks. II. Heating and Cooling. *ApJ*, 529:357–390, January 2000a.
- R. P. Nelson and J. C. B. Papaloizou. The interaction of a giant planet with a disc with MHD turbulence - II. The interaction of the planet with the disc. *MNRAS*, 339:993–1005, March 2003.
- R. P. Nelson and J. C. B. Papaloizou. The interaction of giant planets with a disc with MHD turbulence - IV. Migration rates of embedded protoplanets. *MNRAS*, 350:849–864, May 2004.
- R. P. Nelson, J. C. B. Papaloizou, F. Masset, and W. Kley. The migration and growth of protoplanets in protostellar discs. *MNRAS*, 318:18–36, October 2000b.
- J. C. B. Papaloizou and R. P. Nelson. The interaction of a giant planet with a disc with MHD turbulence - I. The initial turbulent disc models. *MNRAS*, 339:983–992, March 2003.
- J. C. B. Papaloizou, R. P. Nelson, and M. D. Snellgrove. The interaction of giant planets with a disc with MHD turbulence - III. Flow morphology and conditions for gap formation in local and global simulations. *MNRAS*, 350:829–848, May 2004.

- M. Podolak, W. B. Hubbard, and J. B. Pollack. Gaseous accretion and the formation of giant planets. In *Protostars and Planets III*, pages 1109–1147, 1993.
- J. B. Pollack, O. Hubickyj, P. Bodenheimer, J. J. Lissauer, M. Podolak, and Y. Greenzweig. Formation of the Giant Planets by Concurrent Accretion of Solids and Gas. *Icarus*, 124:62–85, November 1996.
- W. H. Press, S. A. Teukolsky, W. T. Vetterling, and B. P. Flannery. *Numerical recipes in C. The art of scientific computing*. Cambridge: University Press, 2nd ed., 1992.
- Python Programming Language. <http://www.python.org>.
- R. R. Rafikov. Planet Migration and Gap Formation by Tidally Induced Shocks. *ApJ*, 572:566–579, June 2002.
- S. N. Raymond, T. Quinn, and J. I. Lunine. Making other earths: dynamical simulations of terrestrial planet formation and water delivery. *Icarus*, 168:1–17, March 2004.
- W. K. M. Rice, P. J. Armitage, M. R. Bate, and I. A. Bonnell. The effect of cooling on the global stability of self-gravitating protoplanetary discs. *MNRAS*, 339:1025–1030, March 2003.
- D. C. Richardson, T. Quinn, J. Stadel, and G. Lake. Direct Large-Scale N-Body Simulations of Planetesimal Dynamics. *Icarus*, 143:45–59, January 2000.
- S. M. Rucinski. IRAS observations of T Tauri and post-T Tauri stars. *AJ*, 90:2321–2330, November 1985.
- C. Schäfer, R. Speith, M. Hipp, and W. Kley. Simulations of planet-disc interactions using Smoothed Particle Hydrodynamics. *A&A*, 418:325–335, April 2004.
- N. I. Shakura and R. A. Sunyaev. Black holes in binary systems. Observational appearance. *A&A*, 24:337–355, 1973.

- F. Shu. *Physics of Astrophysics, Vol. II: Gas Dynamics*. Published by University Science Books, 648 Broadway, Suite 902, New York, NY 10012, 1991.
- J. G. Stadel. *Cosmological N-body simulations and their analysis*. PhD thesis, University of Washington, 2001.
- S. E. Strom, S. Edwards, and M. F. Skrutskie. Evolutionary time scales for circumstellar disks associated with intermediate- and solar-type stars. In *Protostars and Planets III*, pages 837–866, 1993.
- T. Takeuchi, S. M. Miyama, and D. N. C. Lin. Gap Formation in Protoplanetary Disks. *ApJ*, 460:832–+, April 1996.
- H. Tanaka, T. Takeuchi, and W. R. Ward. Three-Dimensional Interaction between a Planet and an Isothermal Gaseous Disk. I. Corotation and Lindblad Torques and Planet Migration. *ApJ*, 565:1257–1274, February 2002.
- Douglas Thain, Todd Tannenbaum, and Miron Livny. Distributed computing in practice: The condor experience. *Concurrency and Computation: Practice and Experience*, 2004. URL <http://cs.wisc.edu/condor/>.
- E. W. Thommes and J. J. Lissauer. Planet Migration. In *Proceedings of STSci Astrophysics of Life Symposium*, September 2002.
- R. I. Thompson, B. A. Smith, and J. J. Hester. Embedded Star Formation in the Eagle Nebula. *ApJ*, 570:749–757, May 2002.
- exoplanets.org. California & Carnegie Planet Search.
- J. Wadsley, J. Stadel, and T. Quinn. Gasoline: a flexible, parallel implementation of TreeSPH. *New Astronomy*, 9:137–158, February 2004.
- W. R. Ward. Density waves in the solar nebula - Differential Lindblad torque. *Icarus*, 67:164–180, July 1986.

- W. R. Ward. Protoplanet Migration by Nebula Tides. *Icarus*, 126:261–281, April 1997.
- S. J. Weidenschilling and J. N. Cuzzi. Formation of planetesimals in the solar nebula. In *Protostars and Planets III*, pages 1031–1060, 1993.
- D. J. Wilner and O. P. Lay. Subarcsecond Millimeter and Submillimeter Observations of Circumstellar Disks. In *Protostars and Planets IV*, pages 509+, May 2000.
- G. Wuchterl, T. Guillot, and J. J. Lissauer. Giant Planet Formation. In *Protostars and Planets IV*, pages 1081–+, May 2000.
- D. Zwilliger. *CRC Standard Mathematical Tables and Formulae*. CRC Press, Boca Raton, Fl., 30th Edition, 1996.

VITA

Graeme Lufkin was born in Massachusetts in 1977. He grew up in New Jersey, expressing the frustration with school that is typical of people who like science. As an undergraduate at Case Western Reserve University in Cleveland, Ohio he had a rollicking-good time earning bachelor of science degrees in Physics and Mathematics. In 1999 he moved to Seattle, Washington to start graduate school in the Physics Department at the University of Washington. After the soul-crushing first two years, he found an adopted home in the Astronomy Department. After three more years he somehow convinced the faculty to grant him a Ph.D., and he's really quite happy about it.